Insights into Nucleic Acid Secondary Structures and Biomimetic Synthetic Ion Channels by Molecular Probes

Thesis submiTTed for The degree of

Doctor of PhilosoPhy (Science)

Jadavpur university

September 2022

By

RAJ PAUL

School of chemical ScienceS

Indian AssociAtion for the cultivAtion of Science

KolKata, Indla

Dedicated to My Parents & Family

‘Behind every success there is a succession of failures’

CERTIFICATE FROM THE SUPERVISOR

This is to certify that the thesis entitled "***Insights into Nucleic Acid Secondary Structures and Biomimetic Synthetic Ion Channels by Molecular Probes***" Submitted by Sri Raj Paul who got his name registered (Index 161/18/Life Sc./26) on 10th September, 2018 For the award of Ph. D. (Science) degree of Jadavpur University, is absolutely based upon his own work under the supervision of Prof. Jyotirmayee Dash and that neither this thesis nor any part of it has been submitted for either any degree / diploma or any other academic award anywhere before.

.....
....

Dash 21/09/2022
.....
.....

(Signature of the Supervisor(s) date with official seal)

Prof. Jyotirmayee Dash
Senior Professor
School of Chemical Sciences
IACS, Jadavpur
Kolkata - 700032

ACKNOWLEDGEMENTS

This thesis cannot be described as a solitary endeavor; the long list that follows indeed proves the same. First and foremost, I am sincerely grateful to my supervisor ***Professor Jyotirmayee Dash*** *for giving me the opportunity to work into her group: without her patience, continuous support and guidance; this thesis would not have been accomplished. During this tenure, she has contributed to a gratifying experience by giving me scholarly freedom in my work, engaging me in new concepts & ideas, and demanding quality work in all my endeavors. I am also thankful to* ***Prof. Mark Wallace*** *for giving me the opportunity to work with his group for a short-term research internship. This short-term project would have not been possible without his continuous support and thorough guidance amidst COVID-19 pandemic. I thank all the faculty members, administrative and technical staffs of* ***Indian Association for the Cultivation of Science*** *(IACS) who helped me in many ways to reach this milestone. I would also like to thank the faculty members of Department of Life Science and Biotechnlogy, Jadavpur University for their useful suggestions and staffs for administrative help and support during this rollercoaster voyage.*

I am indebted to the ***Department of Science & Technology****, India for the* ***INSPIRE fellowship*** *and funding, which removed the financial concerns from my decision to board on this journey. I am also thankful to the* ***British Council*** *for the* ***Newton-Bhabha research grant*** *under India-United Kingdom research collaboration and providing me the opportunity for a short-term research work in King's College London, United Kingdom.*

I am thankful to Central Service Scheme (CSS) of IACS for providing me enough necessary facilities to perform research work throughout my stay. This PhD journey would have been incomplete without continuous motivation and support of my beloved labmates. I cannot express their contribution in words on the road of this thesis bring to an end. My heartfelt thanks to all the current lab members: Manish Da, Rakesh Da, Tania Di, Ritapa, Khushnood, Semantee Di, Jayashree Di, Joydeb Da, Shilpi, Ananta, Soumya, Nabin, Binayak, Charles, Sandip, Pratap and previous lab members: Puja Di, Dipayan Da, Debasish Da, Deepanjan Da, Tirtha Da, Gargi Di, Tanima Di, Tridev Da, Subhro Da, Snehasish Da, Pavan Da, Sudarshan Da, Arunabha, Arkoprovo for their motivation, continuous support and enthusiasm. The juniors and new comers in the lab: Tathagato, Debasmita, Sudeshna, Somenath, Swomi, Palash have always made the lab environment full of elation with their energetic nature and eager to learn new things. As a senior lab member, it always feels great to guide juniors by making scientific discussions, new ideas, helping them to perform experiments and other lab works which could be useful to carry forward their research. I am also thankful to my labmates from Wallace lab: Jason, Jo, Eve, Daisy, Christopher, Steven, Yujie, Guanzhong, Kherina, Lucian, Zhongdao for all the help and support during my short-term stay in King's College London. I am sincerely grateful to the teacher's from my school, college and university who have always motivated me with their blessings to accomplish my goal. I thank all my friends from school, college, university and IACS who have always cheered my success and inspired me to move forward during tough times.

Last, but not the least, I would like to dedicate this thesis to my adored family; my parents, my sister Riya, grandparents (Dida Dadu), Uncles (Baramama, Mejhomama, Chhotomama) and Aunties (Masi) for their love, patience, sacrifice and support throughout my student life and PhD tenure.

Contents

Acronyms

Å	Angstrom 10^{-10} m
°C	Degree centigrade
μM	micromolar
μm	micrometer
Ca	Calcium
CD	Circular dichroism
CF	Carboxyfluorescein
CLSM	Confocal laser scanning microscopy
cm	Centimeter
CoV-2	Coronavirus-2
DNA	Deoxyribonucleic acid
DPhPC	1,2-diphytanoyl-sn-phosphatidylcholine
DMSO	Dimethylsulfoxide
EYPC	egg yolk L-α-Phosphatydylcholine
equiv./eq	equivalent
FAM	6- carboxyfluorescein
FACS	Fluorescence-activated cell sorting
FID	Fluorescence intercalator displacement

FRET	Förster resonance energy transfer
FBS	Fetal bovine serum
FITC	Fluorescein isothiocyanate
G	Guanosine
G4	G-quadruplex
g	grams
GUVs	Giant unilamellar vesicles
h	hour
H_2O	Water
H-bonding	Hydrogen bonding
HPTS	8-hydroxypyrene-1,3,6-trisulfonic acid trisodium salt
K	Potassium
Kcaco	Potassium cacodylate
LUVs	Large unilamellar vesicles
mut	Mutant
M	Molar
mM	millimolar
mg	milligrams
min	minutes
ms	milliseconds

MQ water	MilliQ water
μM	micromolar
μL	microliter
Na	Sodium
NHE	Nuclease hypersensitive element
NMR	Nuclear magnetic resonance
nM	Nanomolar
nm	Nanometer
nA	Nanoampere
nS	Nanosiemens
oSCR	Optical single channel recording
pA	Picoampere
PBS	Phosphate-buffered saline
pS	Picosiemens
qRT-PCR	Quantitative real-time polymerase chain reaction
rt/RT	Room temperature
RNA	Ribonucleic acid
RT-PCR	Real-time polymerase chain reaction
SARS	Severe acute respiratory syndrome
TAMRA	6-carboxytetramethylrhodamine

TIRF	Total internal reflection fluorescence microscopy
TO	Thiazole orange
UV	Ultraviolet
Vis	Visible
XTT	2,3-Bis-(2-Methoxy-4-Nitro-5-Sulfophenyl)-2H-Tetrazolium-5-Carboxanilide

List of Figures

Figure 1A.1. Schematic representation of native *c-KIT* constructs containing wild type promoter region. *WKIT1* and *WKIT2* represent the wild type *c-KIT1* and *c-KIT2*, respectively.

Figure 1A.2. (a) Thermal stabilization values (ΔT_M) of the G4s (*c-KIT1*, *c-KIT2*, *c-MYC*, *BCL-2*, *KRAS*, *VEGF*, *h-TELO*) and *ds26* DNA in presence of **TPW**, **TPE**, **TPA**, **TBE** and **TBA** at 1 µM concentration in 60 mM potassium cacodylate (K-Caco) buffer (pH 7.4). (b) FRET competition assay of **TPW** (1.0 μM) bound *c-KIT1* G4 (0.2 µM) [Control] in the presence of competitor *ds26* and *ct* (*calf thymus*) DNA (up to 50 equivalent con.) in 60 mM potassium cacodylate buffer (pH 7.4).

Figure 1A.3. (a) Fluorometric titration of **TPW** with *c-KIT1* G4 in the presence of 60 mM K-Caco buffer (pH 7.4). (b) Uv visible spectrum of **TPW**.

Figure 1A.4. Fluorometric titration of (A) **TPW** (10 µM) (B) **TPE** (10 µM), (C) **TPA** (10 µM), and (D) **TBA** (10 µM) in the presence of G4s (*c-KIT1*, *c-KIT*2, *c-MYC*, *KRAS*, *BCL-2*, *h-TELO*) and *ds26* DNA. (E) 3D Bar diagram showing fluorescence intensity fold change of **TPW**, **TPE**, **TPA**, **TBE** and **TBA** after addition of DNA up to 5 µM. (F) Thiazole orange displacement in terms of Relative Fluorescence Units (RFU) change (%) after titration of **TPW** with *c-KIT1* quadruplex.

Figure 1A.5. Representative binding isotherms for the binding of **TPW** with the *c-KIT1* G4 monitored through ITC in the presence of 60 mM potassium cacodylate buffer (pH 7.4) at 25 °C. (A) Heat burst curves and (B) the equilibrium K_d obtained through fitting the raw data.

Figure 1A.6. (A) Confocal images of HeLa cell nuclei (fixed) stained with **TPW (blue)**, **TPE (blue)** and **BG4 (red)**. (B) Quantification of BG4 foci per nucleus. For the analysis, >50 cells were counted and the standard error of the mean was calculated from three replicates. *P <0.05 (Student's 't' test).

Figure 1A.7. qRT-PCR analysis for transcriptional regulation of *c-KIT*, *c-MYC* and *BCL-2* after treatment with **TPW** or **TPE** in leukemia cells (K562) for 24 h. Quantification was done in terms of fold change by double delta C_T method using 18s rRNA or GAPDH as housekeeping or reference gene. Fold change of ligand treated relative gene expression is normalized with control or untreated value of 0. Three biological replicates were employed for the quantifications. Error bars represent mean ±SD.*P<0.05 (Student's t test), versus control or untreated leukemia cells. Relative luciferase expression of *c-KIT*, *c-MYC* and *BCL-2* promoters normalized with the Renilla plasmid pRL-TK after treatment with **TPW** or **TPE** at two different doses for 48 h. Fold change of ligand treated relative luciferase expression is normalized with control or untreated value of 0. Error bars

correspond to mean ±SD. *P<0.05 (Student's t test), versus untreated leukemia cells.

Figure 1A.8. Western blot analysis for monitoring relative protein expression of *c-KIT*, *c-MYC* and *BCL-2* by densitometric analysis of immunoreactive bands after treatment with **TPW** or **TPE** in K562 cells for 24 h. Fold change of ligand treated relative protein expression is normalized with control or untreated value of 0. Error bars correspond to mean ±SD. *P<0.05 (Student's t test), versus leukemia cells.

Figure 1A.9. Molecular docking of **TPW** with *c-KIT1* (A, B) (energy = -9.317 kcal.mol^{-1}) and **TPE** with *c-KIT1* (C, D) (energy = -4.49 kcal.mol^{-1}) obtained from Autodock 4.0. Ligands (shown in stick and ball mode) stacked on a terminal G-quartet, represented as hydrophobic surface. **TPW** and **TPE** were represented in dim gray and magenta color respectively.

Figure 1B.1. (A) 3D plot of thermal stabilization profile (ΔT_M) of the G4s (*c-MYC*, *BCL-2*, *c-KIT1*, *KRAS*, *h-TELO*) and *ds26* DNA in the presence of peptidomimetic ligands at 2 μM concentration in 60 mM potassium cacodylate (K-Caco) buffer (pH 7.4). (B) FRET titration of **TBT1** with the G4s (*c-MYC*, *BCL-2*, *c-KIT1*, *KRAS*, *h-TELO*) and *ds26* DNA in 60 mM potassium cacodylate (K-Caco) buffer (pH 7.4).

Figure 1B.2. (A) Determining the K_d value of **TBT1** with G4s and *ds26* DNA, **&** (B) Fluorometric titration of **TBT1** with *c-MYC22* in the presence of 60 mM K-Caco buffer (pH 7.4).

Figure 1B.3. Cell viability determination of **TBT1** in HeLa cells.

Figure 1B.4. Cellular localization of **TBT1** in HeLa cells.

Figure 1B.5. (A) qRT-PCR analysis for transcriptional regulation of *c-MYC* after treatment with **TBT1** in MCF-7 cells for 24 h. Quantification was done in terms of fold change by double delta C_T method using 18s rRNA as housekeeping or reference gene. Fold change of ligand treated relative gene expression is normalized with control. (B) Western blot analysis for translational regulation of *c-MYC* after treatment with **TBT1** in MCF-7 cells for 24 h. Three biological replicates were employed for the quantifications. Error bars represent mean ±SD. *P<0.05, **P<0.05 and ***P<0.001 (Student's t test), versus control MCF-7 cells.

Figure 2.1. CD profiles of SARS-CoV-2 *RG-1*, *RG-2*, *RG-3*, *RG-1 (Mut)* and *RG-2 (Mut)* at the 5 µM concentrations in the presence of 100 mM Tris-KCl buffer (pH 7.4).

Figure 2.2. Determining the stabilization potential of **RD5** for *RG-1*, *RG-2*, *RG-3* SARS-CoV-2 quadruplex and *dsDNA* in the presence of 100 mM Tris-KCl buffer (pH 7.4).

Figure 2.3. (A) Fluorometric titration of **RD5** with *RG-2* quadruplex in the presence of 100 mM Tris-KCl buffer. (B) Isothermal calorimetric titration experiment of **RD5** with *RG-2* in the presence of 100 mM Tris-KCl buffer (pH 7.4).

Figure 3A.1. Design of thiazolyl peptidomimetics **TBP1** and **TBP2**

Figure 3A.2. HPTS assay & determination of EC_{50} values for measuring the ion transport activity of **TBP2** in the presence of Na^+ and K^+. Buffer composition: Internal – 10 mM HEPES 100 mM KCl (pH 6.4); External –10 mM HEPES 100 mM KCl (pH 7.4). (C) EC_{50} value determination of **TBP2** in presence of external buffer – 10 mM HEPES 100 mM NaCl or KCl (pH 7.4), internal buffer – 10 mM HEPES 100 mM KCl (pH 6.4).

Figure 3A.3. CF release assay. Determination of CF release percentage in presence of **TBP1** and **TBP2** (External: 10 mM HEPES 100 mM NaCl, pH 7.4, Internal: 10 mM HEPES 100 mM NaCl, pH 7.4) after 8 minutes.

Figure 3A.4. Current measurement of **TBP2** in the presence of 1 M NaCl at (A, B) -80 mV, (C) +80 mV or 1 M KCl at (D) -80 mV and (E) +80 mV, respectively. (F) Bar diagram for frequency vs current of **TBP2** in the presence of 1 M NaCl (G) or 1 M KCl (at -80 mV). (H) I-V curve plot of **TBP2** in the presence of 1 M NaCl or 1 M KCl.

Figure 3A.5. Membrane colocalization of **TBP2** in GUVs by confocal microscopy.

Figure 3A.6. TEM images of **TBP2** in both NaCl and KCl buffer (pH 7.4).

Figure 3A.7. (A) FRET based melting experiments to determine stabilization potential (ΔT_M) of **TBP1** and **TBP2** for G4s and *ds26* DNA. (B) FRET titration of **TBP2** with G4s and *ds26* DNA **TBP2** in 60 mM potassium cacodylate buffer (pH 7.4). Fluorescence titration of (C) **TBP2** and (D) **TBP1** in 60 mM potassium cacodylate buffer (pH 7.4).

Figure 3A.8. Cell viability assay for **TBP2** in different cancer (HeLa, K562, A549) and normal kidney epithelial (NKE) cell lines.

Figure 3A.9. Confocal images of HeLa cell (fixed) stained with **TBP2** (blue) and NucRed (red). Co-localization experiment of **TBP2** with NucRed in cancer cells. Scale bar represents 5 μm.

Figure 3A.10. qRT-PCR analysis (A, B) for transcriptional regulation of *c-MYC* after treatment with **TBP2** in HeLa cells for 24 h. Quantification was done in terms of fold change by double delta C_T method using 18s rRNA as housekeeping or reference gene. Fold change of ligand treated relative gene expression is normalized with control. Three biological replicates were employed for the quantifications. Error bars represent mean ±SD. *P<0.05 and **P<0.001 (Student's t test), versus control HeLa cells. (C) Relative luciferase expression of *c-MYC*

promoter normalized with the Renilla plasmid pRL-TK after treatment with **TBP2** at two different doses for 48 h. Percentage change of ligand treated relative luciferase expression is normalized with control. Error bars stand for mean ±SD. *P<0.05 (Student's t test), versus untreated HeLa cells.

Figure 3B.1. Proposed model of ion transport via folic acid derived synthetic transmembrane nanopore.

Figure 3B.2. Structure of folic acid derivatives.

Figure 3B.3. pH-sensitive HPTS assay and determination of EC_{50} value for measuring the ion transport activity of **F1**-**F7** (80 μM) in presence of Na^+ and K^+ ions. a) Buffer composition: External – 10 mM HEPES 100 mM NaCl (pH 7.4), Internal – 10 mM HEPES 100 mM NaCl (pH 6.4), b) Buffer composition: External – 10 mM HEPES 100 mM KCl (pH 7.4), Internal – 10 mM HEPES 100 mM NaCl (pH 6.4).

Figure 3B.4. CF leakage assay. Determination of CF release percentage in the presence of **F7** and **F4** (External: 10 mM HEPES 100 mM NaCl or KCl, pH 7.4, Internal: 10 mM HEPES 100 mM NaCl, pH 7.4) after 8 minutes.

Figure 3B.5. Fluorescence titration of **F7** and **F4** with increasing amount of LUVs in a) External and internal 10 mM HEPES 100 mM NaCl buffer, pH 7.4 or b) External 10 mM HEPES 100 mM KCl buffer, Internal 10 mM HEPES 100 mM NaCl buffer, pH 7.4.

Figure 3B.6. Ion conductance measurement of A) **F7** and B) **F4** in the presence of 1 M NaCl or 1 M KCl at -100 mV, respectively. I-V curve plot of (C) **F7** and (D) **F4** in the presence of 1 M NaCl or 1 M KCl.

Figure 3B.7. Dye influx assay with **F7** and **F4** using EYPC GUVs exposed to fluorophore ATTO 633. **F7** and **F4** cause dye influx inside the GUVs in a time dependent manner and likely span the membrane. Scale bar represents 1 µm.

Figure 3B.8. AFM and TEM images of **F7** and **F4**.

List of publications

1. **Raj Paul**, Debasish Dutta, Diana Müller, Harald Schwalbe, Jyotirmayee Dash*. 'Artificial ion channel with DNA selective small molecule.' (*Communicated*)
2. Y Pavan Kumar, Manish Debnath, Tania Das, **Raj Paul** and Jyotirmayee Dash*. Guanosine Derivatives based Artificial Membrane Porins for Drug Transport. (*Communicated*)
3. **Raj Paul**, Debasish Dutta, Tania Das, Manish Debnath, Jyotirmayee Dash* (2021). 'G4 Sensing Pyridyl-thiazole Polyamide Represses *c-KIT* Expression in Leukemia Cells.' ***Chemistry–A European Journal,*** 27(33), Pages 8590-8599. ***doi.org/10.1002/chem.202100907***
4. Puja Saha, Deepanjan Panda, **Raj Paul**, Jyotirmayee Dash* (2021). 'A DNA nanosensor for monitoring ligand-induced i-motif formation.' ***Organic & Biomolecular Chemistry,*** 19(9), pp.1965-1969. ***doi.org/10.1039/D1OB00248A***
5. Rakesh Paul, Debasish Dutta, **Raj Paul** and Jyotirmayee Dash* (2020). 'Target Directed Azide-Alkyne Cycloaddition for Assembling HIV-1 TAR RNA Binding Ligands'. ***Angew. Chem. Int. Ed. 10.1002/anie.202003461***

6. Swarup Krishna Bhattacharyya, Madhab Dule, **Raj Paul**, Jyotirmayee Dash, Md Anas, Tarun Kumar Mandal, Poushali Das, Narayan Chandra Das, Susanta Banerjee* (2020). 'Carbon dot cross-linked gelatin nanocomposite hydrogel for pH-sensing and pH-responsive drug delivery.' ***ACS Biomaterials Science & Engineering,*** 6(10), pp.5662-5674. ***10.1021/acsbiomaterials.0c00982***

7. Debasish Dutta, **Raj Paul**, Jyotirmayee Dash*. 'G4 selective antineoplastic peptidomimetic curbs *MYC* expression in Breast Cancer cells.' (Manuscript under preparation)

8. **Raj Paul**, Durjoy Majumder* (2017) Development of Algorithm for Lorenz Equation using different Open Source Softwares. ***Journal of Computer Science & Systems Biology*** 10: 087-092. doi:10.4172/jcsb.1000255

Abstract

Nucleic acid secondary structures have evolved as important therapeutic targets in cancer and infectious diseases. The G-rich sequences of human genome hold the potential to form DNA or RNA secondary structures known as G-quadruplexes (G4s). Stabilization of G4 structures by small molecules could lead to the development of anticancer as well as antiviral therapeutics and diagnostics. The proto-oncogenes like *c-MYC*, *c-KIT*, *BCL-2* promoters and human telomeres contain guanine-loaded sequences to form G4 structures. *c-KIT* and *c-MYC* proto-oncogenes play critical role in cell proliferation and differentiation, cellular growth and apoptosis. Mutation in *c-KIT* or *c-MYC* proto-oncogene could lead to the development of leukemia and breast cancer like critical diseases. The thesis consists of introduction, three chapters, conclusion and an experimental section. The first chapter describes targeting oncogenic G4s by molecular probes, and is subdivided into two sections. In the first section (Chapter 1A), a thiazole based G4 sensing polyamide has been developed, which recognizes G4 structures and represses *c-KIT* proto-oncogene expression in leukemia cells. Owing to excellent fluorescence enhancement property inside cells, the polyamide has been used as molecular probe to image the cellular system. In the next section (Chapter 1B), , a series of thiazole based peptide ligands have been studied, which show highest

stabiliztion potential as well as high binding affinity for the *c-MYC* G4. One of the ligands represses *c-MYC* oncogene expression in breast cancer cells. The peptidomimetic ligand exhibits potent toxicity towards the cancer cells while it does not show toxicity for the normal cells. The nuclear localization and intracellular fluorescence property make it a unique molecular scaffold to probe biological systems.

The ongoing SARS-CoV-2 (COVID-19) pandemic has inspired us to work on small molecule based antiviral therapeutics due to its deadly combination of high infection and mutation rate. In Chapter 2, the G-rich sequences present in CoV-2 genome have been first characterized to identify the putative G-quadruplex structures. The RNA G-quadruplex structures *RG-1*, *RG-2* and *RG-3* present in the CoV-2 genome could be a potent therapeutic target for the development of small molecule drugs. A coumarin based peptidomimetic has been developed that preferentially binds to the *RG-2* motif of SARS-CoV-2 over duplex DNA. This peptidomimetic ligand may lead to further development of small molecule based therapeutics for COVID-19.

The Chapter 3 describes the development of bioinspired ion channels from synthetic molecules. This chapter is divided into two subsections. The first section (Chapter 3A) describes ion channel formation using a G-quadruplex binding peptidomimetic ligand. The fabrication of artificial ionophores with G4 selective

chemotherapeutic small molecules has not been explored so far. An artificial ion channel has been constructed with a G4 specific thiazole based peptidomimetic that forms nanovesicular and nanofibrillar structures allowing transportation of Na^+ and K^+ via model lipid bilayer membrane with high ionic conductance. Besides, the peptidomimetic ligand preferentially binds to *c-MYC22* G4 with high affinity and inhibits *c-MYC* oncogene expression at m-RNA level following cancer cell death. This study would provide critical structural and functional aspects of artificial ion channels and open up a new paradigm for developing novel synthetic ion transporters with improved therapeutic potential.

Inspired from naturally occuring guanosine, the next study describes the formation of highly conductive transmembrane nanopore from folate guanosine derivatives (Chapter 3B). The folate guanosine derivatives span the lipid membrane and transport Na^+ and K^+ with very high conductance indicating the formation of large pore via cell membrane mimicking artificial lipid bilayer. In addition, the ligands allow the influx of small molecular cationic dye through GUV membrane, which again demonstrates the folate mediated construction of stable nanoporous structure. This work would shed light on designing membrane nanopores by naturally derived or bioinspired molecules as ion transporters that would find applications in drug delivery systems, and biosensing.

INTRODUCTION

Nucleic acid secondary structures

Nucleic acids are often referred as a 'blueprint of life'; as their primary role is to store and process the genetic information in living organisms.[1] Since the discovery of DNA (Deoxyribonucleic Acid) structure by Watson and Crick (1953),[2] past few decades have seen substantial research and development in the knowledge and understanding of nucleic acid structures and functions within biological systems.[3] However, many aspects of nucleic acids are not fully understood, and so elucidation of the biological significance of DNA and RNA (Ribonucleic Acid) structures remains as interesting field to the chemical biology.[4] Because of the polymorphic nature of nucleic acids,[5] DNA might possess various structural variations[6] in the form of right handed B-DNA or duplex DNA, triple stranded DNA, four stranded guanine-rich self-assembled structures etc.[7] Likewise, apart from the basic structure, RNA can also hold secondary hairpin structures, stem-loop like structures, guanine-rich four stranded structures under physiological conditions.[8,9]

Understanding the functional importance of single-stranded nucleic acids is of great relevance because of its major role in many biological processes including replication, transcription, and translation, and transposition machinery in the human genome.[10] The single stranded DNA can form various secondary structures by Watson–Crick base-pairing and other non-canonical interactions.[11]The guanine

rich single stranded DNA or RNA can fold into four stranded structures in the presence of monovalent cations like Na^+ or K^+ under physiological microenvironment, known as G-quadruplexes (G4s).[12, 13]

Primary G-quartet structure

The basic structural motif of the G-quadruplex relies on the G-quartet, also called G-tetrad.[13] The supra-molecular co-planar arrangement of four guanine bases is governed by Hoogsteen hydrogen-bonding[14] to construct the G-quartet structure. Stacks of G-quartets are stabilized by cations (e.g., K^+, Na^+, Li^+) centrally coordinated to O6 of the guanines.[15]

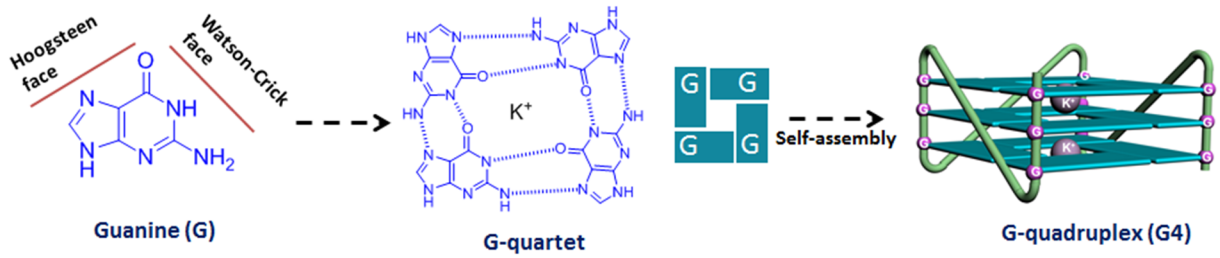

Figure 1. Schematic diagram of G-quadruplex formation.

Topology of G-quadruplexes

More than two guanine repeat sequences of DNA can form the G4 structure by stacking of more than two planar G-quartets.[15] The topologies or the specific folding patterns of G4 depend on the directions of these contiguous guanine repeats.[16] G4 structures are categorized into parallel, hybrid and anti-parallel type depending upon the orientation of the G-tract (Figure 2). In the parallel

conformation, all four G main chains are parallel while one and two G-tracts are anti-parallel in case of hybrid and anti-parallel topologies, respectively.[16,17] The G-tract connecting sequences are called loops,[18] and based on the shape of the loops they are classified as: propeller, lateral, and diagonal type. The propeller type joins the adjacent parallel G- chains, and the lateral loop connects the adjacent anti-parallel Guanine backbones.[18,19] On the contrary, the diagonal loops connect the G-main chain on the diagonal of the G-quartet. Thus, the parallel G4s possess three propeller loops, while the hybrid one holds two lateral loops and one propeller loop, and the anti-parallel conformation has two lateral loops and one diagonal loops, or three lateral loops.[20] Moreover, the hybrid topology possess two distinct forms, form-1 and form-2, in telomeric G4, and these differ in the order of the G-main chains and loops. Based on the loop types, the anti-parallel G4 can hold chair and basket conformation.[18-21]

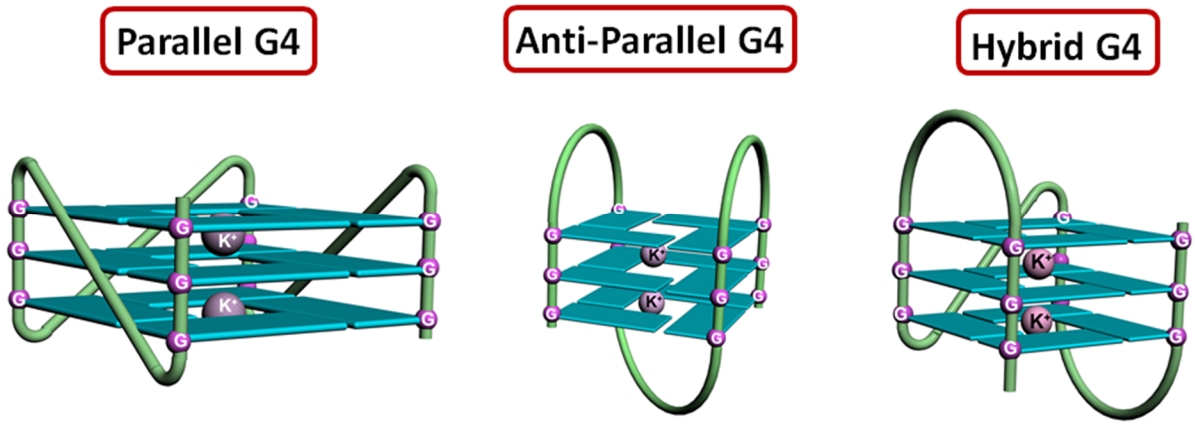

Figure 2. Structural conformation of G-quadruplexes (G4s).

Oncogenic G-quadruplexes (G4s)

Eddy and Maizels[22] revealed a significant prevalence of G-quadruplexes in oncogenes. The promoter region of proto-oncogenes like *c-MYC*, *c-KIT*, *BCL-2* retain guanine-rich sequences having the propensity to form four stranded G-quadruplex structures.[23] Aberration in structures and functions of those proto-oncogenes could lead to altered gene regulation and cancer like critical pathogenesis.[24,25]

c-MYC

c-MYC is one of the most abundant proto-oncogenes overexpressed up to 80% of all human cancers including colorectal, breast, cervix, lung, leukemia, osteosarcomas and glioblastomas.[25-28] The *MYC* acts as a master transcription factor,[29] binds to particular E-boxes in the target promoter and regulates the gene expression, which is crucial to many physiological processes such as cellular growth, apoptosis, angiogenesis and metastasis.[28,29] *MYC* acts like a transcriptional accelerator in cancer cells and repressing the *MYC* oncogene can cause inhibition of tumor growth and induction of tumor regression permanently.[28-30] The two important cis-elements lie upstream of the P1 and P2 promoters, designated as the far upstream sequence element (FUSE) and the NHE III_1, the FUSE is a cruise control element functioning as a physical sensor of ongoing *MYC* gene

transcription, whereas the NHE III_1 element is involved in both activating and silencing its transcription.[29-31] The *c-MYC* G4 possesses parallel topology.

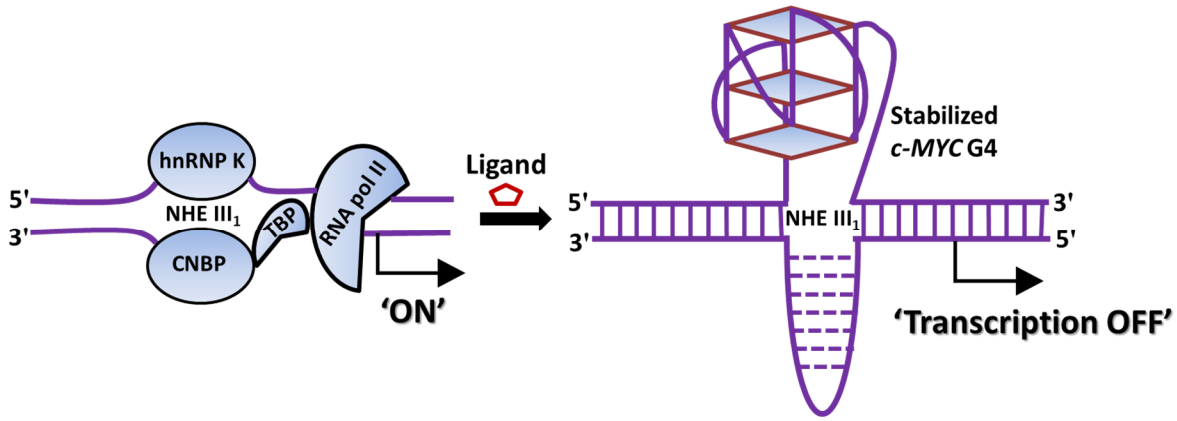

Scheme 1. Schematic model for ligand mediated repression of *c-MYC* gene transcription (gene 'OFF') via stabilization of *c-MYC* promoter G-quadruplex. hnRNP K and CNBP are single-stranded DNA binding proteins to act as transcriptional activator.

The NHE III_1 contains a 27-bp purine-rich sequence (Pu27) located -142 to -115 bp upstream of the P1 promoter.[29-32] Notably, the Pu27 consists of five consecutive G-tracts; three of these tracts are composed of four guanines and two tracts are composed of three guanines, indicating its high potential to form G4 structures. As the *MYC* G4 structure functions as a silencer element of transcription, ligand mediated stabilization of G4 can potentially be used as therapeutics to reduce *MYC* expression in cancer cells (Scheme 1).[30-33]

c-KIT

c-KIT codifies a type-III RTK (receptor tyrosine kinase) for stem cell factor (SCF), which is a key to cell proliferation, migration, maturation and survival in different

cancer types.[34] The overexpression of *c-KIT* is observed in various malignant cancers like myeloid leukemia (due to kinase mutation causing c-*KIT* protein auto phosphorylation), pancreatic cancers, Gastric Intestinal Stromal Tumors (GIST), colorectal cancers etc.[35-37] The *c-KIT* promoter comprises three neighboring regions capable of folding into parallel G4 structures: *c-KIT1*, *c-KIT** (a G-rich Sp1 binding site) and *c-KIT2* which are positioned between −109 and −182 nucleotides upstream of the ATG start site.[38-39] Experimental evidence and theoretical studies indicate that *c-KIT1* G4 forming sequence exists as a parallel G4 topology wherein one non-G-tract guanine takes part in the center of stacked G-quartets. Most importantly, *c-KIT1* G4 plays significant role in *c-KIT* transcription in cancer cells.[38-48]

BCL-2

BCL-2, an anti-apoptotic protein[49] has been found to be dysregulated in a variety of pathological conditions e.g., B-cell and T-cell lymphomas and breast, prostate, cervical, colorectal, and non-small cell lung carcinomas etc.[50] Moreover, *BCL-2* overexpression is linked with poor prognosis and interfere with conventional cancer therapeutics.[51] The P1 promoter of human *BCL-2* gene, located at 1386–1423 bp upstream of the translation start site, possesses GC-rich multiple transcriptional start sites and positioned within a nuclease hypersensitive site.[52] This mixed parallel/antiparallel-stranded G-quadruplex structure contains three G-

tetrads of mixed G-arrangements, which are connected with two lateral loops and one side loop, and four grooves of different widths.[52,53] The distinct major *BCL2* promoter G-quadruplex structure suggests that it can be specifically involved in gene modulation and can be an attractive target for pathway-specific drug design.

Telomeric G-quadruplexes (G4s)

h-TELO

Human telomere present in the chromosomal end play pivotal role in cellular ageing and cancer like deadly diseases.[54] Telomerase overexpression is observed in ~ 90% of cancer cells and maintains telomere length homeostasis (acting as a tumor promoter).[54,55] The telomeric DNA contain numbers of the G-rich GGGTTA tandem repeats with 100–200 flanking nucleotides at 3′-end.[56] The G-rich single stranded sequences of telomeric DNA or RNA could build four stranded G-quadruplex structure based G-quartets stack, leading to telomerase inhbition.[57] Hence, small molecules can bind and stabilize telomeric DNA quadruplex and regulate telomere length and cellular functions.[58]

RNA G-quadruplexes (G4s) in virus

G-quadruplex forming G-rich sequences are found in the viral genome or viral RNAs that could act as regulator of major viral proteins, responsible for evading the host immune response.[59] Recent studies suggest that despite the high recombination rate, the putative G-quadruplex forming sequences present in the

viral genome are highly conserved, indicating the importance of G4s in viral replication and evolution.[60] Such properties direct that the viral G-quadruplexes could act as potential targets for antiviral therapy.[61]

The positive stranded (+) severe acute respiratory syndrome coronavirus (SARS-CoV) was known after 2003 outbreak, leading to the death of ~ 10% of the infected people.[62] SARS-CoV can be categorized as one of the most contagious and pathogenic virus belonging to the Coronaviridae family.[62,63] SARS-CoV specific antiviral drug is not available for the treatment of coronavirus infected people till date.[63] However, a novel coronavirus was discovered on late December, 2019 (COVID-19) in Wuhan, China; named as severe acute respiratory syndrome coronavirus 2 (SARS-CoV-2), has rapidly spread worldwide and provoked global health leading to socio-economic disturbance.[62-64] The SARS-CoV-2 led to severe atypical pneumonia among the children that entails

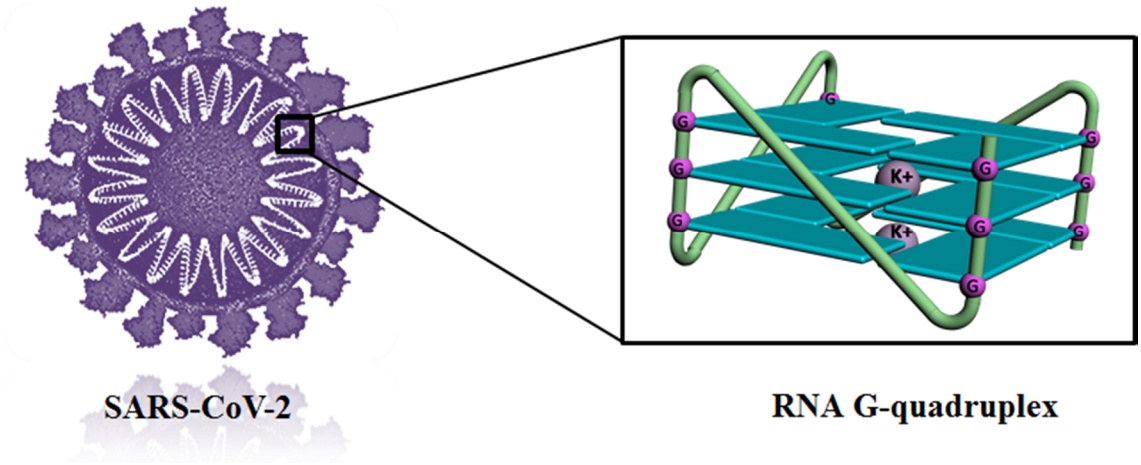

Figure 3. Schematic representation of RNA G4 harboring SARS-CoV-2 structure.

urgent hospitalization with high mortality among the old aged and immunocompromized people.[64] SARS-CoV-2 holds a single-stranded positive-sense RNA genome of 29.6 kb length that encrypts 16 non-structural proteins (e.g., Nsp1 - Nsp16), several accessory proteins, and four essential structural proteins, including small envelope (E) protein, nucleocapsid (N) protein, spike (S) glycoprotein, and matrix (M) protein.[64,65] Latest studies indicate that the nucleocapsid (N), Nsp10 and spike (S) protein harbor the G-quadruplex forming sequences that can fold into four stranded G-quadruplex structures, identified as *RG-1*, *RG-2*, *RG-3* and *RG-4*, respectively.[66-70] Specific targeting and stabilization of these RNA G4 structures present in the viral genome could be a potent strategy towards the development of novel anitiviral therapeutics against the COVID-19.[70-72]

Examples of G4 binding small molecules

The stabilization of G-quadruplex structure by small molecules has been considered as an important therapeutic strategy for cancer and microbial diseases.[74] G4-targeted therapy has been prompted by the functional relationship between G4 and gene regulation (especially oncogene regulation), DNA replication, DNA repair, genome instability, and telomere length.[75,76] Telomestatin derivatives could target the human telomeric G4s and shortens the telomere leading to cancer cell death.[77,78] A tri-substituted molecule, BRACO-19 could stabilize G4s and inhibit

the telomerase enzyme activity by significantly reducing the h-TERT expression in cancer cells.[79] Pyridostatin derivatives (PDS) target major oncogenic G4s and repress gene expression in cancer cells.[74,80] The cationic porphyrin molecule TmPyP4 suppresses the expression of *c-MYC* oncogene via the stabilization of G4s thereby limiting the proliferation of cancer cells.[81] The G4 specific naphthalene diimide ligand CM03 has been reported to show potent chemotherapeutic activity towards cancer cells and in a pancreatic ductal adenocarcinoma mouse model via targeting G4 rich oncogenes, which play pivotal role in cancer-cell survival, metastasis, and drug resistance mechanism.[82] Another G4 ligand CX-5461 has arrived in the clinical trials to cure BRCA1 and BRCA2 deficient cancer.[83]

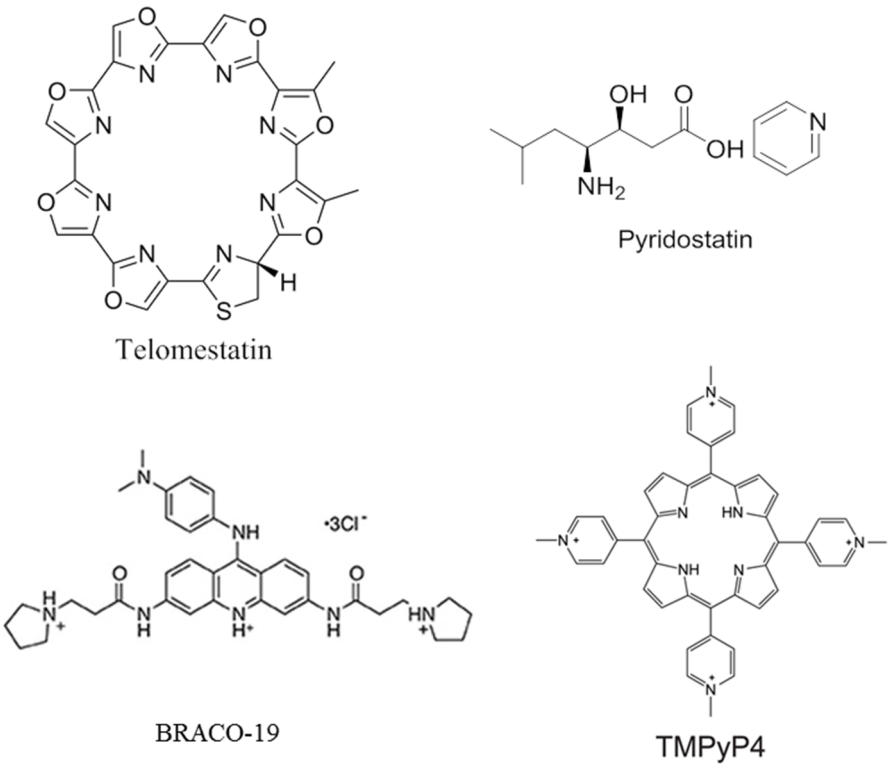

Figure 4. Chemical structure of G4 binding ligands.

Small molecule based artificial ion channel via model lipid bilayers

Biological Ion Channels

Cell membrane or plasma membrane acts as an essential unit of life by splitting the internal intracellular space from the external extracellular environment.[84] The semipermeable phospholipid cell membranes control the ionic or molecular metabolites exchange in cellular microenvironment.[85] Owing to the structural incompatibility of the hydrophobic cell membranes and the hydrophilic metabolites, molecules or ions cannot pass through the membrane and their translocation may be triggered by ion channels or carriers in response to external

microenvironment like pH, ionic strength, temperatures etc.[85,86] Natural ion channels are complex membrane proteins that assist the transport of ions across the cell membranes. The ion channels play critical role in maintaining the cellular homeostasis to endure life processes including cellular proliferation and differentiation, signal transduction, cellular growth and apoptosis.[86,87] Thus, the dysfunction of the channel protein may lead to several channel related diseases or channelopathies of neuromuscular system (e.g., epilepsy, migraine, paralysis), endocrine system (e.g., diabetes), respiratory system (e.g., cystic fibrosis), cardiovascular system (e.g., hypertension), immune system (e.g., anti-NMDA receptor encephalitis, Isaac syndrome) and renal system (e.g., BartterQs syndrome), cancer.[88,89]

Artificial Ion Channels

Owing to the importance of natural ion channels, immense research efforts are made towards the development of artificial ion channels using synthetic molecules.[91] The key methods are related with the designing of self-assembled supra-molecular structures by aggregation of small molecular components to generate active membrane spanning nanostructures. The nanostructures are built by employing non-reversible covalent bonds like hydrogen-bonding, electrostatic interactions, metal-coordination etc.[91,92] In addition to therapeutics for channelopathies, synthetic ion channels can be used to understand the biological

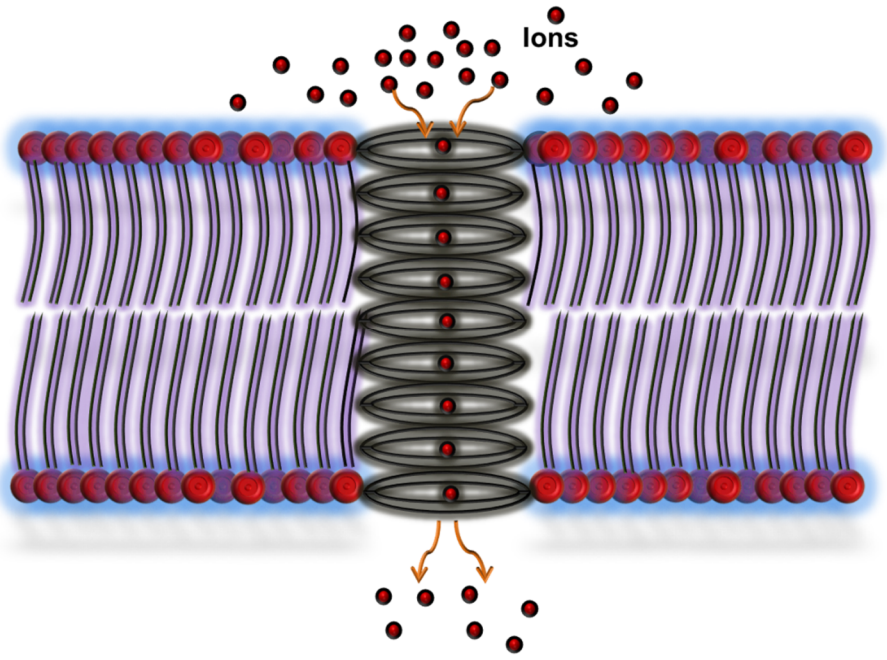

Figure 5. Schematic illustration of artificial ion channels.

channel functions, thereby opening the avenues for various applications in drug delivery systems, biosensing, nanotechnologies or nanodevices.[93] Current research also lies on developing artificial channels with chemotherapeutic properties leading to new therapeutic dimension in the treatment of cancer.[94,95] Supramolecular synthetic ion channels can mimic the self-assembly process of natural membrane proteins in relation to both structure and functions; and might possess significant advantages, like controllable transport, flexibility and diversity due to their in-built adaptive characteristics.[95,96] These properties of synthetic channels empower the understanding of the detailed transport mechanism and structure activity

relationship. To date, there are excellent examples of synthetic ion transporters e.g., β-cyclodextrin derivatives,[97] peptide based foldamers,[98] valinomycin[99] etc.[91-99]

Lipid Bilayer

Biological membranes are composed of lipid bilayers as their primary structural unit.[100] The membrane lipid bilayers are the clusters of amphiphilic lipid molecules linked together by hydrophobic interactions between acyl chains.[100,101] The membrane bilayers of cells separate the intracellular compartment from extracellular environment. When phospholipids are exposed to the hydrophilic region, the self-assembly take place into a two-layered sheet, where the hydrophobic tail part headed towards the center of the sheet.[102] Thus, two "leaflets" form single molecular layer each. The center part of the bilayer is extremely hydrophobic and eliminates water soluble molecules like sugar and salts. The self-assembly process is the result of interactions between hydrophobic molecules known as hydrophobic effect.[103] The increased hydrophobicity permits interaction of water molecules more easily with each other that increases the overall entropy of the complex system. This complex process is governed by non-covalent bonds like van der Waals interactions, electrostatic interactions and strong hydrogen bonds.[100-103]

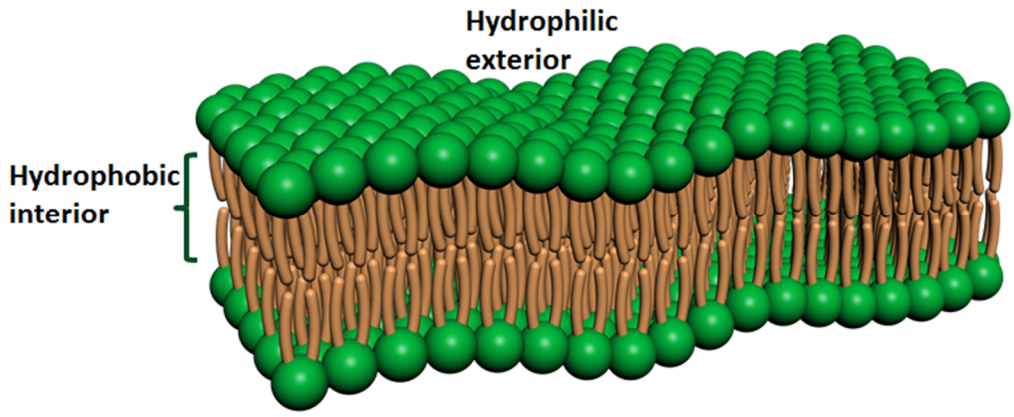

Figure 6. Basic structure of lipid bilayers.

The lipid bilayer structure was first discovered as the architectural unit of cell membrane in 1925 and the in-detail investigation of lipid structure of cell membranes started four decades ago.[104] In 1972, Singer and Nicholson first proposed a fluid mosaic model to explain the membrane structure.[105] This model hypothesized that lipids and proteins diffuse freely within the plane of the cell membrane. Since then, the discovery of large membrane domains (e.g., basal regions of glandular, endothelial and epithelial cells) and lateral microdomain structures (e.g., lipid rafts, caveolae, and coated pits) revealed the complex nature of the cell membrane structure.[106]

Model bilayers

On the basis of chemical structure, membrane lipids are grouped into: glycerol-based phospholipids, cholesterol and ceramide-based sphingolipids.[107] Phospholipids are classified into different groups primarily based on the

hydrophilic head: phosphatidylcholine (PC), phosphatidylethanolamine (PE), and phosphatidylserine act as predominant lipids in the cell membrane, while a low percentage of phosphatidylinositol and cardiolipin are found in the membrane.[107,108] Owing to this complex membrane structure with the extremely dynamic lipid-lipid and lipid-protein interfaces, exploring the biophysical and biomolecular interactions with small molecules, drugs and drug delivery systems became very challenging task.[109] Hence, simplified artificial membrane bilayer systems, that mimic the natural cell membrane lipid bilayer, have been established.[110]

Liposomes or vesicles

About five decades ago, Bangham and co-workers discovered the liposomes, identified as spherical vesicles, which form after the phospholipids come in contact with the aqueous environment.[111,112] Liposomes are described as microscopic vesicles comprising of phospholipid or any analogous amphipathic lipid bilayers.[113] They are largely used for encapsulation and effective delivery of both lipophilic and polar or hydrophilic materials and could serve as a non-toxic carrier for drugs, metal ions or other chemical substances.[114,115] Based on the size or diameter, liposomes are classified into different categories which range from the smallest vesicle (diameter 20 nm) to giant liposomes that are prominently visible and distinguishable under the light microscope, with $\geq$ 1 μm in diameter, almost

similar to the dimensions of cells.[114-116] Vesicles or liposomes are mainly divided into multilamellar vesicles (MLVs) and unilamellar vesicles (ULVs) in relation to structural composition of lipid membrane. ULVs are composed of a single phospholipid bilayer membrane with the diameter range of 0.02 – 200 µm. These unilamellar liposomes are classified into small unilamellar vesicles (SUVs) (diameter ~ 0.02 – 0.10 µm), large unilamellar vesicles (LUVs) (diameter ~ 0.2 – 1 µm) and giant unilamellar vesicles (diameter ~ 1 – 200 µm).[117]

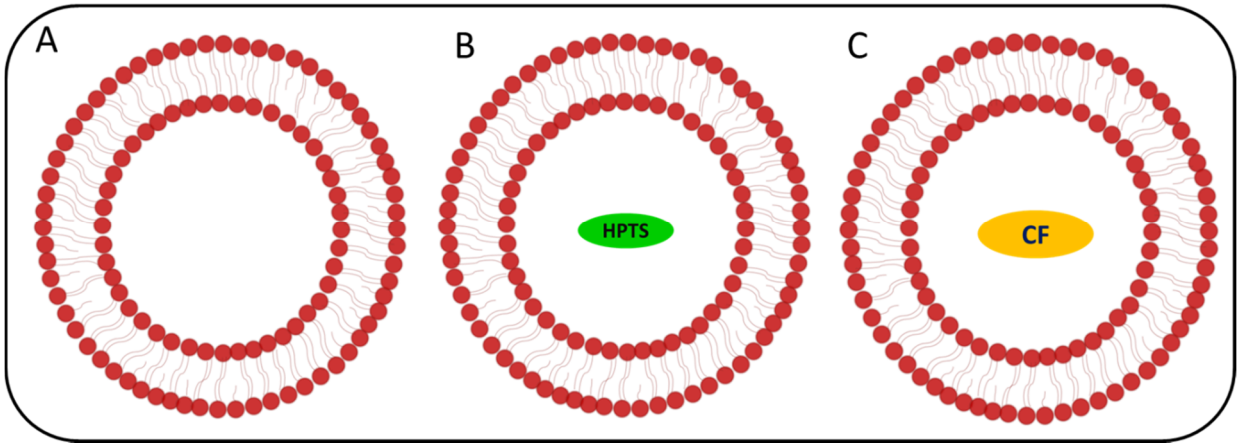

Figure 7. Schematic illustration of (A) blank, (B) HPTS & (C) CF entrapped Large Unilamellar Vesicles (LUVs).

Droplet Interface Bilayers (DIBs)

Apart from the vesicular model lipid bilayer membrane, one of the main objective of bottom-up synthetic biology involves reconstitution of structure, function and behavior of living systems from supramolecular chemical assemblies.[118,119] Now a days, a miniaturized version of natural membrane is often used i.e., water-in-oil

(w/o) droplets formed by stable lipid monolayer, where interaction between two droplets leads to the formation of a lipid bilayer at the droplet interface, which is referred as Droplet Interface Bilayers (DIBs).[119,120] DIBs possess many advantages over other traditional planar bilayer systems like black lipid membranes (BLMs) or aperture suspended bilayers, that includes more stability, compartmentalization of droplet content and the ability to support droplet volumes spanning three orders of magnitude from mililitre (ml) to picolitre (pl).[121]

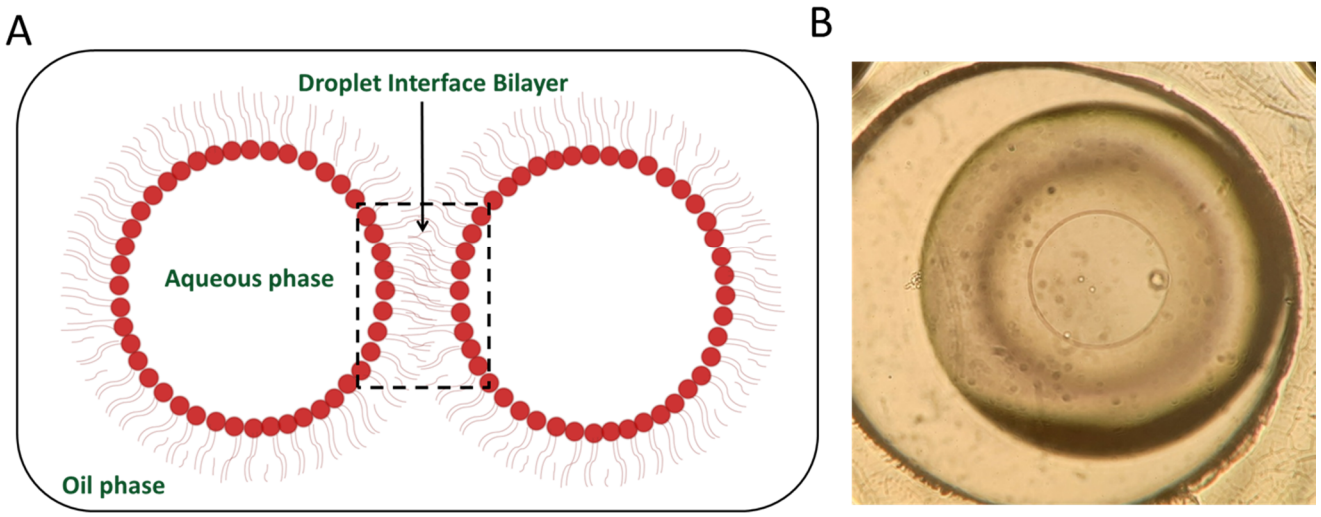

Figure 8. (A) Schematic representation of droplet interface bilayers (DIBs). (B) Microscopic image of DIB.

The DIB technology delivers miniaturized methods to screen ion channels, build high-throughput assays with very low volumes ranging from nanolitre to picolitre amounts of small molecules or drug candidates.[123] The droplet-interface-bilayer (DIB) system holds large-scale solutions to solve the challenges related to the

available live cell-based techniques, generation of artificial lipid membrane, in which ion channel studies can be performed by mimicking the cellular microenvironment .[124,125] Therefore, the use of DIBs play promising role to study intracellular ion channels by accompanying life-cell electrophysiology data.

Total Internal Reflection Fluorescence Microscope (TIRFM)

TIRFM is a sophisticated powerful technique to selectively image the fluorescent molecules like GFP, lipid membrane dyes, fluorochromes attached to DNA sequences, proteins or antibodies in an aqueous medium with comparatively high refractive index (e.g; cover glass).[126,127] The evanescent wave or evanescent field i.e., the thickness of the excitation depth can be < 100 nm from the solid surface in TIRF. In comparison, the thickness of a confocal image section is approximately 500 nm. The advantages of using TIRF microscope include: (1) the background is substantially decreased resulting in a high signal-to-background ratio to clearly see the structures at single molecule level (2) elimination of out-of focus fluorescence; (3) samples are readily exposed to very less amount of incident light.[128]

A total internal reflection fluorescence (TIRF) microscope with high spatial resolution and fast scanning is presently used to examine the localization and dynamics of ion channels in the cell membrane and model lipid membranes e.g., droplet interface bilayers.[129-131] In the field of biophysics and cell biology, TIRF microscopy is often used to observe the single molecule fluorescence and

localization of Ca^{2+} signaling.[132] The single molecule analysis by TIRF imaging in living cells provides valuable information on physiology and pathology of ion channel functions coupled with complex molecular system in the lipid membrane. In addition, TIRF imaging of spatiotemporal Ca^{2+} events that occur in the junctional structures of the plasma membrane specific to Ca^{2+} signal has facilitated in-depth understanding on the cellular mechanisms. Precise determinations of the distribution, dynamic behavior, subunit composition, and interacting molecules or proteins of ion channels by TIRF have been directly related to the channel function and development of therapeutics.[129-132]

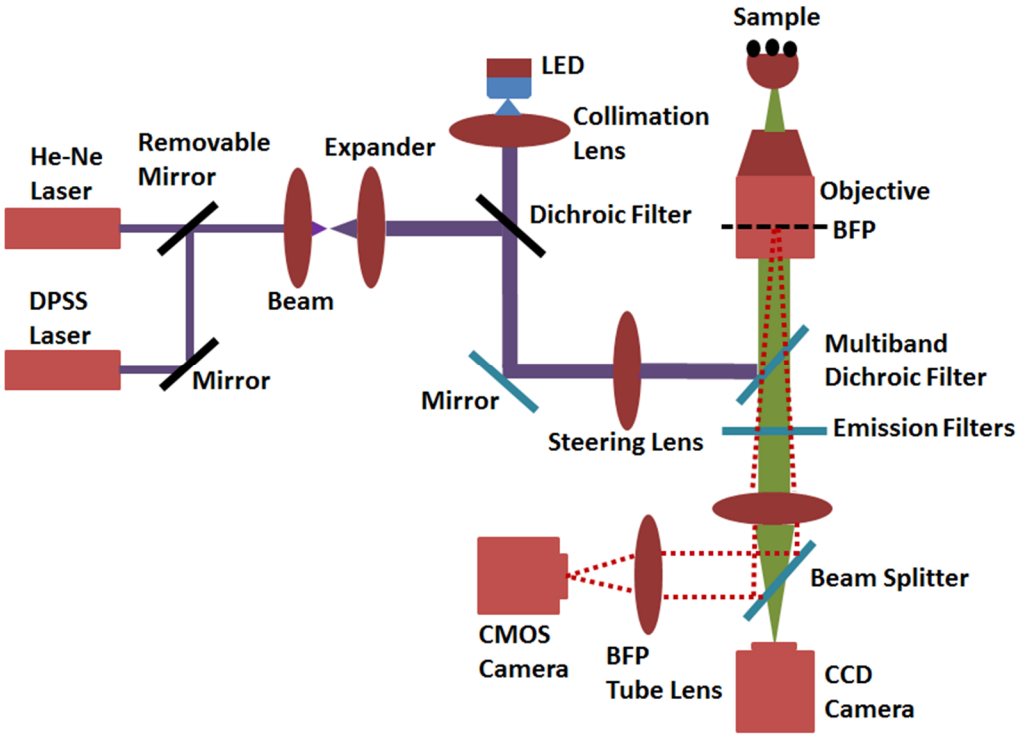

Figure 9. Schematic diagram of Total Internal Reflection Fluorescence (TIRF) Microscopic imaging system.

Small molecule based Artificial Ion Channels

Till date, a large variety of synthetic molecules have been reported to act as trans-membrane transporter of ions which show potent channel like activities. The synthetic ion channels may be classified based on the chemical structures, transport characteristics etc.[91,93,133]

Macrocyclic ion channels

Building synthetic ion channels with macrocyclic compounds has gained large attention in last few decades. Widely used example of such ion-channel building compounds are crown-ethers, cyclodextrins (CDs), cucurbit[n]urils (CBs), calix[n]arenes (CAs), pillar[n]arenes (PAs).[91]

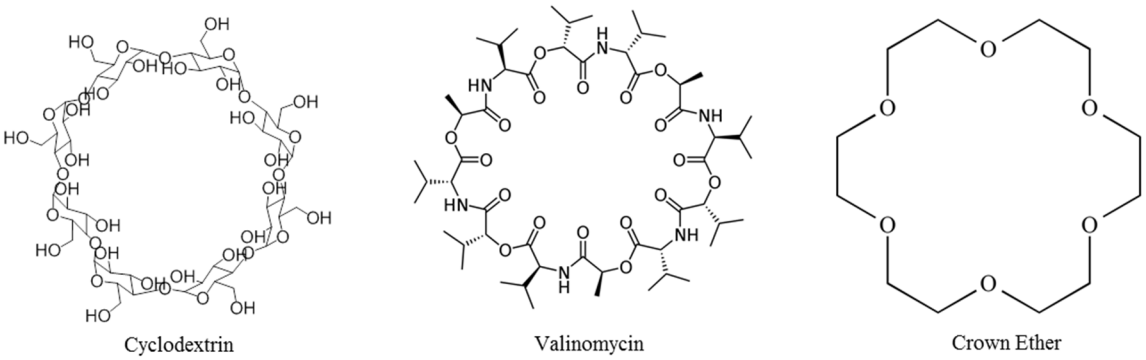

Figure 10. Schematic representation of artificial ion channel forming small molecules.

Peptide based ion channels[134]

Last few decades have seen a huge effort in the development of synthetic ion channels with the peptide and their mimetics. A large number of peptide based ligands have been reported to act as synthetic transporter of ions. Few examples of

such ion channel forming peptides include: peptide based foldamers, peptide based macrocycles, peptide-crown ether conjugated nanochannels, amphiphilic heptapeptides etc.

Helical ion channels

Guanine (G) like biomolecules could stack upon each other to form a central core in the presence of monovalent cations like K^+, Na^+, Cs^+ etc. leading to the formation of artificial ion channels. In 1960, Davis and co-workers discovered that the supramolecular self-assembly of guanine structures could lead to the formation of G-quadruplex structures via square-planar arrangement of G-tetrads in presence of metal ions like K^+. The G-quadruplex structure could form a hollow cavity like structure for its potential use as supra-molecular ion channel.[135] Matile et. al. reported a folate rosette structure to construct self-assembled folate quartet via π-π stacking interactions in the absence of cations. The supra-molecular self-assembly of folate resulted in the formation of cation selective ion transporter with high conductance values.[136] In 2008, Ling Ma et. al elucidated that ditopic guanosine coupled with lithocholic acid could form distinct channels in planar phospholipid bilayer via the formation of large stable pores.[137] Recently, our group demonstrated G-quadruplex based ion channels with high permeability and selectivity for K^+.[138]

References

1. P. Belmont, J.-F. Constant, M. Demeunynck, *Chemical Society Reviews* **2001**, *30*, 70-81.
2. J. D. Watson, F. H. Crick, *Nature* **1953**, *171*, 737-738.
3. J. Spiegel, S. Adhikari, S. Balasubramanian, *Trends in Chemistry* **2020**, *2*, 123-136.
4. R. L. Adams, *The biochemistry of the nucleic acids*, Springer Science & Business Media, **2012**.
5. N. Sugimoto, *Chemistry and Biology of Non-canonical Nucleic Acids*, John Wiley & Sons, **2021**.
6. J. Kypr, I. Kejnovská, D. Renčiuk, M. Vorlíčková, *Nucleic acids research* **2009**, *37*, 1713-1725.
7. J. T. Grün, H. Schwalbe, *Biopolymers* **2022**, *113*, e23477.
8. G. W. Collie, G. N. Parkinson, *Chemical Society Reviews* **2011**, *40*, 5867-5892.
9. M. Zuker, D. Sankoff, *Bulletin of mathematical biology* **1984**, *46*, 591-621.
10. J. L. Huppert, *Chemical Society Reviews* **2008**, *37*, 1375-1384.
11. J. SantaLucia, D. Hicks, *Annual review of biophysics and biomolecular structure* **2004**, *33*, 415-440.
12. D. Sen, W. Gilbert, *nature* **1988**, *334*, 364-366.
13. H. J. Lipps, D. Rhodes, *Trends in cell biology* **2009**, *19*, 414-422.
14. J.-C. Francois, C. Helene, *Biochemistry* **1995**, *34*, 65-72.
15. D. Bhattacharyya, G. Mirihana Arachchilage, S. Basu, *Frontiers in chemistry* **2016**, *4*, 38.
16. S. Burge, G. N. Parkinson, P. Hazel, A. K. Todd, S. Neidle, *Nucleic acids research* **2006**, *34*, 5402-5415.

17. Y. Ma, K. Iida, K. Nagasawa, *Biochemical and Biophysical Research Communications* **2020**, *531*, 3-17.
18. N. Smargiasso, F. Rosu, W. Hsia, P. Colson, E. S. Baker, M. T. Bowers, E. De Pauw, V. Gabelica, *Journal of the American Chemical Society* **2008**, *130*, 10208-10216.
19. A. Guedin, J. Gros, P. Alberti, J.-L. Mergny, *Nucleic acids research* **2010**, *38*, 7858-7868.
20. H. L. Lightfoot, T. Hagen, N. J. Tatum, J. Hall, *FEBS letters* **2019**, *593*, 2083-2102.
21. J. Dai, M. Carver, D. Yang, *Biochimie* **2008**, *90*, 1172-1183.
22. J. Eddy, N. Maizels, *Nucleic acids research* **2006**, *34*, 3887-3896.
23. T. A. Brooks, S. Kendrick, L. Hurley, *The FEBS journal* **2010**, *277*, 3459-3469.
24. C. M. Croce, *New England journal of medicine* **2008**, *358*, 502-511.
25. B. Hoffman, D. A. Liebermann, *Oncogene* **1998**, *17*, 3351-3357.
26. K. B. Marcu, *Bioessays* **1987**, *6*, 28-32.
27. D. J. Patel, A. T. n. Phan, V. Kuryavyi, *Nucleic acids research* **2007**, *35*, 7429-7455.
28. S. Pelengaris, M. Khan, G. Evan, *Nature Reviews Cancer* **2002**, *2*, 764-776.
29. C. V. Dang, L. M. Resar, E. Emison, S. Kim, Q. Li, J. E. Prescott, D. Wonsey, K. Zeller, *Experimental cell research* **1999**, *253*, 63-77.
30. D. Yang, L. H. Hurley, *Nucleosides, Nucleotides, and Nucleic Acids* **2006**, *25*, 951-968.
31. T. A. Brooks, L. H. Hurley, *Nature Reviews Cancer* **2009**, *9*, 849-861.
32. S. Balaratnam, J. S. Schneekloth Jr, in *Annual Reports in Medicinal Chemistry, Vol. 54*, Elsevier, **2020**, pp. 361-407.
33. W. Wang, S. Hu, Y. Gu, Y. Yan, D. B. Stovall, D. Li, G. Sui, *Biochimica et Biophysica Acta (BBA)-Reviews on Cancer* **2020**, *1874*, 188410.

34. L. K. Ashman, R. Griffith, *Expert opinion on investigational drugs* **2013**, *22*, 103-115.
35. M. Bejugam, M. Gunaratnam, S. Müller, D. A. Sanders, S. Sewitz, J. A. Fletcher, S. Neidle, S. Balasubramanian, *ACS Med. Chem. Lett.* **2010,** *1*, 306-310.
36. D. Wei, J. Husby, S. Neidle, *Nucleic Acids Res.* **2014,** *43*, 629-644.
37. K. I. McLuckie, Z. A. Waller, D. A. Sanders, D. Alves, R. Rodriguez, J. Dash, G. J. McKenzie, A. R. Venkitaraman, S. Balasubramanian, *J. Am. Chem. Soc.* **2011,** *133*, 2658-2663.
38. X. Xia, Y.-C. Lo, A. A. Gholkar, S. Senese, J. Y. Ong, E. F. Velasquez, R. Damoiseaux, J. Z. Torres, *ACS Chem. Biol.* **2019.**
39. T. Furitsu, T. Tsujimura, T. Tono, H. Ikeda, H. Kitayama, U. Koshimizu, H. Sugahara, J. H. Butterfield, L. K. Ashman, Y. Kanayama, *J Clin Investig.* **1993,** *92*, 1736-1744.
40. E. Weisberg, P. W. Manley, S. W. Cowan-Jacob, A. Hochhaus, J. D. Griffin, *Nat. Rev. Cancer.* **2007,** *7*, 345-356.
41. Q.-L. Guo, H.-F. Su, N. Wang, S.-R. Liao, Y.-T. Lu, T.-M. Ou, J.-H. Tan, D. Li, Z.-S. Huang, *Eur. J. Med. Chem.* **2017,** *130*, 458-471.
42. R. Rigo, C. Sissi, *Biochemistry* **2017,** *56*, 4309-4312.
43. C. Ducani, G. Bernardinelli, B. r. Högberg, B. K. Keppler, A. Terenzi, *J. Am. Chem. Soc.* **2019,** *141*, 10205-10213.
44. A. T. Phan, V. Kuryavyi, S. Burge, S. Neidle, D. J. Patel, *J. Am. Chem. Soc.* **2007,** *129*, 4386-4392.
45. P. S. Shirude, B. Okumus, L. Ying, T. Ha, S. Balasubramanian, *J. Am. Chem. Soc.* **2007,** *129*, 7484-7485.

46. Z. A. Waller, S. A. Sewitz, S.-T. D. Hsu, S. Balasubramanian, *J. Am. Chem. Soc.* **2009,** *131*, 12628-12633

47. A. Chauhan, S. Paladhi, M. Debnath, S. Mandal, R.N. Das, S. Bhowmik and J. Dash, *Bioorg. Med. Chem* **2014**, *22*, 4422-4429.

48. S. Rankin, A. P. Reszka, J. Huppert, M. Zloh, G. N. Parkinson, A. K. Todd, S. Ladame, S. Balasubramanian, S. Neidle, *J. Am. Chem. Soc.* **2005**, *127*, 10584-10589.

49. J. T. Opferman, A. Kothari, *Cell Death & Differentiation* **2018**, *25*, 37-45.

50. K. Yip, J. Reed, *Oncogene* **2008**, *27*, 6398-6406.

51. T. Knight, D. Luedtke, H. Edwards, J. W. Taub, Y. Ge, *Biochemical pharmacology* **2019**, *162*, 250-261.

52. J. Dai, D. Chen, R. A. Jones, L. H. Hurley, D. Yang, *Nucleic acids research* **2006**, *34*, 5133-5144.

53. J. Dai, T. S. Dexheimer, D. Chen, M. Carver, A. Ambrus, R. A. Jones, D. Yang, *Journal of the American Chemical Society* **2006**, *128*, 1096-1098.

54. S. A. Stewart, R. A. Weinberg, *Annual review of cell and developmental biology* **2006**, *22*, 531-557.

55. M. A. Blasco, *Nature Reviews Genetics* **2005**, *6*, 611-622.

56. S. Neidle, G. N. Parkinson, *Current opinion in structural biology* **2003**, *13*, 275-283.

57. A. T. Phan, J. L. Mergny, *Nucleic acids research* **2002**, *30*, 4618-4625.

58. J. Zhao, Q. Zhai, *Bioorganic Chemistry* **2020**, *103*, 104229.

59. L. Dumas, P. Herviou, E. Dassi, A. Cammas, S. Millevoi, *Trends in Biochemical Sciences* **2021**, *46*, 270-283.

60. E. Ruggiero, S. N. Richter, *Annual reports in medicinal chemistry, Vol. 54*, Elsevier, **2020**, pp. 101-131.
61. E. Ruggiero, I. Zanin, M. Terreri, S. N. Richter, *International Journal of Molecular Sciences* **2021**, *22*, 10984.
62. J. Yuan, H. Yun, W. Lan, W. Wang, S. G. Sullivan, S. Jia, A. H. Bittles, *American journal of infection control* **2006**, *34*, 234-236.
63. H. Yang, Z. Rao, *Nature Reviews Microbiology* **2021**, *19*, 685-700.
64. B. Hu, H. Guo, P. Zhou, Z.-L. Shi, *Nature Reviews Microbiology* **2021**, *19*, 141-154.
65. A. A. T. Naqvi, K. Fatima, T. Mohammad, U. Fatima, I. K. Singh, A. Singh, S. M. Atif, G. Hariprasad, G. M. Hasan, M. I. Hassan, *Biochimica et Biophysica Acta (BBA)-Molecular Basis of Disease* **2020**, *1866*, 165878.
66. R. A. Khailany, M. Safdar, M. Ozaslan, *Gene reports* **2020**, *19*, 100682.
67. Z. Miao, A. Tidu, G. Eriani, F. Martin, *RNA biology* **2021**, *18*, 447-456.
68. A. Wacker, J. E. Weigand, S. R. Akabayov, N. Altincekic, J. K. Bains, E. Banijamali, O. Binas, J. Castillo-Martinez, E. Cetiner, B. Ceylan, *Nucleic acids research* **2020**, *48*, 12415-12435.
69. D. Ji, M. Juhas, C. M. Tsang, C. K. Kwok, Y. Li, Y. Zhang, *Briefings in bioinformatics* **2021**, *22*, 1150-1160.
70. E. Belmonte-Reche, I. Serrano-Chacón, C. Gonzalez, J. Gallo, M. Bañobre-López, *PloS one* **2021**, *16*, e0250654.
71. C. Zhao, G. Qin, J. Niu, Z. Wang, C. Wang, J. Ren, X. Qu, *Angewandte Chemie* **2021**, *133*, 436-442.
72. N. Panera, A. E. Tozzi, A. Alisi, *Drugs* **2020**, *80*, 941-946.

73. A. Awadasseid, X. Ma, Y. Wu, W. Zhang, *Biomedicine & Pharmacotherapy* **2021**, *139*, 111550.

74. S. Müller, R. Rodriguez, *Expert review of clinical pharmacology* **2014**, *7*, 663-679.

75. F. B. Johnson, in *Annual reports in medicinal chemistry, Vol. 54*, Elsevier, **2020**, pp. 3-44.

76. F. Raguseo, S. Chowdhury, A. Minard, M. Di Antonio, *Chemical Communications* **2020**, *56*, 1317-1324.

77. M.-Y. Kim, H. Vankayalapati, K. Shin-Ya, K. Wierzba, L. H. Hurley, *Journal of the American Chemical Society* **2002**, *124*, 2098-2099.

78. T. Tauchi, K. Shin-Ya, G. Sashida, M. Sumi, S. Okabe, J. Ohyashiki, K. Ohyashiki, *Oncogene* **2006**, *25*, 5719-5725.

79. A. M. Burger, F. Dai, C. M. Schultes, A. P. Reszka, M. J. Moore, J. A. Double, S. Neidle, *Cancer research* **2005**, *65*, 1489-1496.

80. L.-Y. Liu, T.-Z. Ma, Y.-L. Zeng, W. Liu, Z.-W. Mao, *Journal of the American Chemical Society* **2022**.

81. H. Han, D. R. Langley, A. Rangan, L. H. Hurley, *Journal of the American Chemical Society* **2001**, *123*, 8902-8913.

82. A. A. Ahmed, S. Neidle, *Molecules* **2020**, *25*, 5407.

83. H. Xu, M. Di Antonio, S. McKinney, V. Mathew, B. Ho, N. J. O'Neil, N. D. Santos, J. Silvester, V. Wei, J. Garcia, *Nature communications* **2017**, *8*, 1-18.

84. C. M. O'Connor, J. U. Adams, J. Fairman, *Cambridge, MA: NPG Education* **2010**, *1*, 54.

85. G. Banfalvi, in *Permeability of biological membranes*, Springer, **2016**, pp. 1-71.

86. P. Janmey, P. K. Kinnunen, *Trends in cell biology* **2006**, *16*, 538-546.

87. F. Lang, M. Föller, K. Lang, P. Lang, M. Ritter, E. Gulbins, A. Vereninov, S. Huber, *The Journal of membrane biology* **2005**, *205*, 147-157.

88. K. Kunzelmann, *The Journal of membrane biology* **2005**, *205*, 159-173.

89. C. A. Hübner, T. J. Jentsch, *Human molecular genetics* **2002**, *11*, 2435-2445.

90. M. Mayer, J. Yang, *Accounts of chemical research* **2013**, *46*, 2998-3008.

91. S. p. Zheng, L. b. Huang, Z. Sun, M. Barboiu, *Angewandte Chemie International Edition* **2021**, *60*, 566-597.

92. Y. Tu, F. Peng, A. Adawy, Y. Men, L. K. Abdelmohsen, D. A. Wilson, *Chemical reviews* **2016**, *116*, 2023-2078.

93. T. M. Fyles, *Chemical Society Reviews* **2007**, *36*, 335-347.

94. G. W. Gokel, S. Negin, *Accounts of Chemical Research* **2013**, *46*, 2824-2833.

95. I. Alfonso, R. Quesada, *Chemical Science* **2013**, *4*, 3009-3019.

96. M. S. Gin, E. G. Schmidt, P. Talukdar, Wiley Online Library, **2007**, pp. 3-15.

97. J. K. Chui, T. Fyles, *Organic & biomolecular chemistry* **2014**, *12*, 3622-3634.

98. A. D. Peters, S. Borsley, F. Della Sala, D. F. Cairns-Gibson, M. Leonidou, J. Clayden, G. F. Whitehead, I. J. Vitórica-Yrezábal, E. Takano, J. Burthem, *Chemical science* **2020**, *11*, 7023-7030.

99. S. K. Berezin, *The Journal of Membrane Biology* **2015**, *248*, 713-726.

100. M. Edidin, *Nature Reviews Molecular Cell Biology* **2003**, *4*, 414-418.

101. R. Fettiplace, D. Andrews, D. Haydon, *The Journal of membrane biology* **1971**, *5*, 277-296.

102. J. F. Nagle, S. Tristram-Nagle, *Current opinion in structural biology* **2000**, *10*, 474-480.

103. W. C. Wimley, S. H. White, *Biochemistry* **1993**, *32*, 6307-6312.

104. A. A. Spector, M. A. Yorek, *Journal of lipid research* **1985**, *26*, 1015-1035.

105. S. J. Singer, G. L. Nicolson, *Science* **1972**, *175*, 720-731.

106. G. L. Nicolson, *Discoveries* **2013**, *1*.

107. P. V. Escribá, J. M. González-Ros, F. M. Goñi, P. K. Kinnunen, L. Vigh, L. Sánchez-Magraner, A. M. Fernández, X. Busquets, I. Horváth, G. Barceló-Coblijn, *Journal of cellular and molecular medicine* **2008**, *12*, 829-875.

108. B. Alberts, D. Bray, K. Hopkin, A. D. Johnson, J. Lewis, M. Raff, K. Roberts, P. Walter, *Essential cell biology*, Garland Science, **2015**.

109. C. Peetla, A. Stine, V. Labhasetwar, *Molecular pharmaceutics* **2009**, *6*, 1264-1276.

110. A. Luchini, G. Vitiello, *Biomimetics* **2020**, *6*, 3.

111. A. Bangham, *Chemistry and physics of lipids* **1993**, *64*, 275-285.

112. A. Bangham, M. Standish, N. Miller, *Nature* **1965**, *208*, 1295-1297.

113. M. Antonietti, S. Förster, *Advanced Materials* **2003**, *15*, 1323-1333.

114. P. V. Torchilin, V. Torchilin, V. Torchilin, V. Weissig, *Liposomes: a practical approach*, Oxford University Press, **2003**.

115. M. Çağdaş, A. D. Sezer, S. Bucak, *Application of nanotechnology in drug delivery* **2014**, *1*, 1-50.

116. A. Akbarzadeh, R. Rezaei-Sadabady, S. Davaran, S. W. Joo, N. Zarghami, Y. Hanifehpour, M. Samiei, M. Kouhi, K. Nejati-Koshki, *Nanoscale research letters* **2013**, *8*, 1-9.

117. M. C. Woodle, D. Papahadjopoulos, *Methods in enzymology* **1989**, *171*, 193-217.

118. A. J. Dzieciol, S. Mann, *Chemical Society Reviews* **2012**, *41*, 79-85.

119. Y. Elani, *Biochemical Society Transactions* **2016**, *44*, 723-730.

120. H. Bayley, B. Cronin, A. Heron, M. A. Holden, W. L. Hwang, R. Syeda, J. Thompson, M. Wallace, *Molecular BioSystems* **2008**, *4*, 1191-1208.

121. W. L. Hwang, M. Chen, B. Cronin, M. A. Holden, H. Bayley, *Journal of the American Chemical Society* **2008**, *130*, 5878-5879.

122. Y. Huang, G. Fuller, V. C. Suja, *Advances in Colloid and Interface Science* **2022**, 102666.

123. A. B. Theberge, F. Courtois, Y. Schaerli, M. Fischlechner, C. Abell, F. Hollfelder, W. T. Huck, *Angewandte Chemie International Edition* **2010**, *49*, 5846-5868.

124. B. Schlicht, M. Zagnoni, *Scientific reports* **2015**, *5*, 1-8.

125. T. Trantidou, M. Friddin, A. Salehi-Reyhani, O. Ces, Y. Elani, *Lab on a Chip* **2018**, *18*, 2488-2509.

126. F. Abdulkader, R. P. de Campos, J. A. da Silva, F. Ortis, in *Tools and Trends in Bioanalytical Chemistry*, Springer, **2022**, pp. 179-201.

127. H. Yamamura, Y. Suzuki, Y. Imaizumi, *Journal of Pharmacological Sciences* **2015**, *128*, 1-7.

128. K. I. Mortensen, L. S. Churchman, J. A. Spudich, H. Flyvbjerg, *Nature methods* **2010**, *7*, 377-381.

129. O. K. Castell, J. Berridge, M. I. Wallace, *Angewandte Chemie International Edition* **2012**, *51*, 3134-3138.

130. M. Szabo, M. I. Wallace, *Biochimica et Biophysica Acta (BBA)-Biomembranes* **2016**, *1858*, 613-617.

131. J. T. Sengel, M. I. Wallace, *Proceedings of the National Academy of Sciences* **2016**, *113*, 5281-5286.

132. S. Shashkova, M. C. Leake, *Bioscience reports* **2017**, *37*.

133. G. W. Gokel, I. A. Carasel, *Chemical Society Reviews* **2007**, *36*, 378-389.

134. F. Otis, M. Auger, N. Voyer, *Accounts of Chemical Research* **2013**, *46*, 2934-2943.

135. S. L. Forman, J. C. Fettinger, S. Pieraccini, G. Gottarelli, J. T. Davis, *Journal of the American Chemical Society* **2000**, *122*, 4060-4067.

136. N. Sakai, Y. Kamikawa, M. Nishii, T. Matsuoka, T. Kato, S. Matile, *Journal of the American Chemical Society* **2006**, *128*, 2218-2219.

137. L. Ma, M. Melegari, M. Colombini, J. T. Davis, *Journal of the American Chemical Society* **2008**, *130*, 2938-2939.

138. M. Debnath, S. Chakraborty, Y. P. Kumar, R. Chaudhuri, B. Jana, J. Dash, *Nature communications* **2020**, *11*, 1-12.

Chapter 1

Targeting oncogenic G4s by molecular probes

Chapter 1A

A polyamide downregulates c-KIT expression via targeting G-quadruplex in leukemia cells

Selective recognition and modulation of genomic structures by synthetic small molecules are fundamental approaches of chemical biology.[1] Besides the storage of genetic information, the regulation of gene expression is a key function of nucleic acids.[2] Therefore, specific recognition of a gene is pivotal to selectively regulate its expression inside cells.[3] Owing to the occurrence of G-quadruplexes (G4s) in oncogenic promoters (e.g., *c-KIT, c-MYC, BCL-2, KRAS)* and telomeres; targeting these structures has become an elegant approach for cancer therapeutics and diagnostics.[2-10] G4s adopt four-stranded stacked guanine quartets construct in the presence of monovalent cations (e.g., Na^+, K^+). As discussed in the previous section, the distinctive structural morphology and promising biological role make the G4s smart targets for the design of synthetic ligands.[11, 12] Owing to globular structures of G4s with large planes, they can be targeted with high selectivity in contrary to single-stranded and duplex DNAs having linear structures.[13, 14]

In the last two decades, a variety of small molecule ligands have been reported as G4 binding compounds that downregulate mRNA and protein expression of oncogenes.[14-17] Notably, most of the reported compounds exhibit promiscuous cross reactivity and cytotoxicity; thus they might not be suitable for selective recognition and regulation of oncogenes. However, a few ligands like thiazole orange analogues, BMVC (3,6-bis(1-methyl-4-vinylpyridinium)carbazolediiodide), IMT (a benzothiazole derivative), N-TASQ have been studied to act as fluorescent light-up molecular probe for G4 detection in cancer cells.[17] Considering the putative biological importance of quadruplexes, it is a worthy goal to develop and exploit quadruplex specific ligands as

tools for potential therapies as well as to examine and understand G4-related biological mechanisms.[18-22] Herein, we delineate a potential G4 binder, which specifically recognizes quadruplex and attenuate the *c-KIT* proto-oncogene expression without influencing the morphological properties of cells.

c-KIT codifies a type-III RTK (receptor tyrosine kinase) for stem cell factor (SCF), which is a key to cell proliferation, migration, maturation and survival in different cancer types.[23] The overexpression of *c-KIT* is observed in various malignant cancers like myeloid leukemia (due to kinase mutation causing *c-KIT* protein auto phosphorylation), pancreatic cancers, Gastric Intestinal Stromal Tumors (GIST), colorectal cancers etc.[24-26] In particular, identification of novel antileukemic agents and markers became a challenge due to the non-adherent and drug resistance property of leukemia cells.[27, 28] Imatinib is the only clinically approved chemotherapeutic drug which acts through preserving the bcr-abl kinase in an inert state to treat chronic myeloid leukemia (CML).[29] However, due to high mutation rate in bcr-abl kinase, imatinib resistance and it´s adverse effects are so common in patients with CML. Though some second generation inhibitors have been developed to circumvent the challenge, mitigating *c-KIT* oncogene expression via small molecules is considered as an effective way for the treatment of CML.[27-30] The *c-KIT* promoter comprises three neighboring regions capable of folding into parallel G4 structures: *c-KIT1*, *c-KIT** (a G-rich Sp1 binding site) and *c-KIT2* which are positioned between −109 and −182 nucleotides upstream of the ATG start site. Experimental evidences as well as theoretical studies indicate that *c-KIT1* G4 possesses parallel

topology wherein one non-G-tract guanine takes part in the center of stacked G-quartets. It is noteworthy to state that the *KIT1* G4 has a strong influence on biological role of the whole promoter.[31-37] Till date, it has emerged as a difficult task to develop selective inhibitors of *c-KIT*. In this work, we have developed a G4 sensing bis-thiazole polyamide that preferentially binds to *c-KIT1* G4, and modulates *c-KIT* expression in leukemia cells.

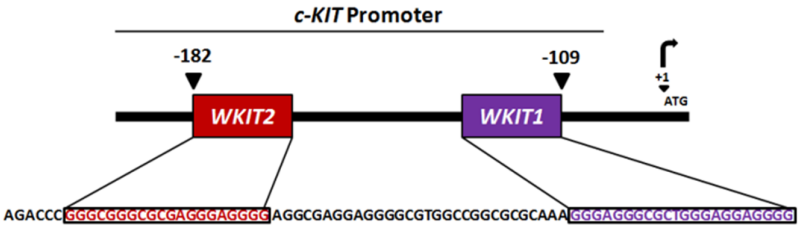

Figure 1A.1. Schematic representation of native *c-KIT* constructs containing wild type promoter region. *WKIT1* and *WKIT2* represent the wild type *c-KIT1* and *c-KIT2*, respectively.

Results and Discussion

We have designed and synthesized a new class of thiazole polyamide and studied the binding interactions with several G4 structures present in the proto-oncogene promoter (*c-KIT1*, *c-KIT2*, *c-MYC*, *BCL-2*, *KRAS*), telomeres *(h-TELO)* and *ds26* DNA.

G-quadruplex ligand design and synthesis

Polyamides are known to bind B-DNA[38] and non B-DNA structures[39] in a sequence-specific manner. Their cellular uptake can further be improved by tuning the physicochemical parameters. Several polyamides are known to recognize DNA minor grooves[39,40] and modulate gene expression inside cells exogenously. Thiazole moiety is present in numerous natural products and pharmaceuticals that exhibit potent biological

activities. Notably, the five-membered thiazole component is present in promising antitumor agents like bleomycin (induces DNA damage), dasatinib (inhibitor of Bcr-Abl tyrosine kinase), tiazofurin (IMP dehydrogenase inhibitor).[41,42] We have designed and synthesized thiazole ligands having pyridine/benzene core that could bind to G-tetrad via π-π stacking interactions. In addition, –NMe2 groups present in the ligand with pyridine core could impart water solubility and binding with G4s through electrostatic interactions.[43]

Bis-thiazole ligands were prepared in two to three steps by using easily accessible starting materials. Bis-thiazole esters **TBE** and **TPE** with a benzene and pyridine ring were synthesized by amide coupling of isophthalic acid **1** and pyridine-2,6-dicarboxylic acid **2** with thiazolyl amino ester **5** via the corresponding acid chlorides **3** and **4**. Ester hydrolysis afforded the corresponding bisacids **TBA** and **TPA** (Scheme 1A.1). The amine side chains were subsequently incorporated by amide coupling of **TPA** with dimethylamino propylamine **6** using HBTU as a coupling reagent to obtain the compound **TPW** (Scheme 1A.1).

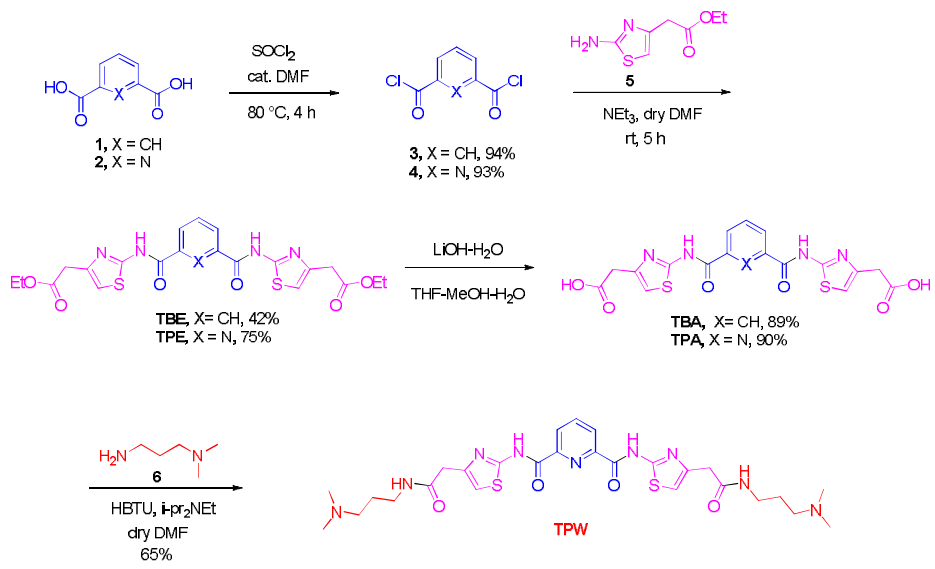

Scheme 1A.1. Synthesis of bis-thiazole compounds containing a benzene ring and pyridine ring.

These compounds contain two thiazole rings. **TPE**, **TPA** and **TPW** contain a pyridine ring and ligands **TBE** and **TBA** contain a benzene core. In polyamide **TPW**, water soluble side chains are connected with the thiazoles through amide bond formation. Thiazole polyamide **TPW**, the bis-esters (**TPE** and **TBE**) and the bis-acids (**TPA** and **TBA**) were studied as G4 targeting compounds for exogenous tuning of oncogene expression using different biophysical and in-cellulo assays.

TPW preferentially binds to *c-KIT1* G4

FRET based melting experiment

The potential of **TPW**, **TPE**, **TPA**, **TBE** and **TBA** to stabilize G4 was evaluated by FRET based melting assay on a panel of 5'-FAM and 3'-TAMRA tagged G4 forming sequences (*c-KIT1*, *c-KIT2*, *c-MYC (Pu27)*, *BCL-2*, *KRAS*, *VEGF*, *h-TELO*) and *ds26* DNA or *duplex* DNA. This high throughput method is used to determine the stabilization induced by the ligand for the G4s and *ds26* DNA by comparing the melting temperature

(T_M) of control (without ligand) and ligand bound DNA.[44] Negligible changes in melting temperature (ΔT_M = 0 to 1.4 °C) were observed for all the investigated G4s with **TPE**, **TPA**, **TBE** and **TBA** up to 10 µM (50 equivalent con.). **TPW** displayed ΔT_M values of 4.8 °C, 2.7 °C and 1.6 °C for *c-KIT1*, *c-KIT2* and *c-MYC* respectively at 1 µM concentration. Intriguingly, **TPW** did not alter the T_M of *BCL-2*, *KRAS*, *VEGF* and *h-TELO* G4s. An overall highest stabilization for *c-KIT1* G4 (ΔT_M = 4.8 °C) was observed with **TPW** at 1 µM (5 equivalent con.) (Figure 1A.2). The melting temperature of *ds26* DNA was not altered with any of these ligands. These results indicate that **TPW** selectively stabilizes *c-KIT1* G4 compared to other investigated G4s and *ds26* DNA.

A FRET competition study was also carried out to further examine the selectivity of **TPW** with *c-KIT1* G4 over *ds26* and *ct* (*calf thymus*) DNA (Figure 1A.2). The melting temperature of 200 nM 5′-FAM *c-KIT1* TAMRA -3′ was observed with **TPW** (1 µM) in the presence of 10 µM *ds26* (*ds26*:*c-KIT1* = 50:1) and *ct* DNA (*ct*:*c-KIT1* = 50:1). **TPW** did not cause any change in ΔT_M value (4.8 °C) of *c-KIT1* G4 in the presence of excess concentration of *ds26* and *ct* DNA (50 equivalent con.).

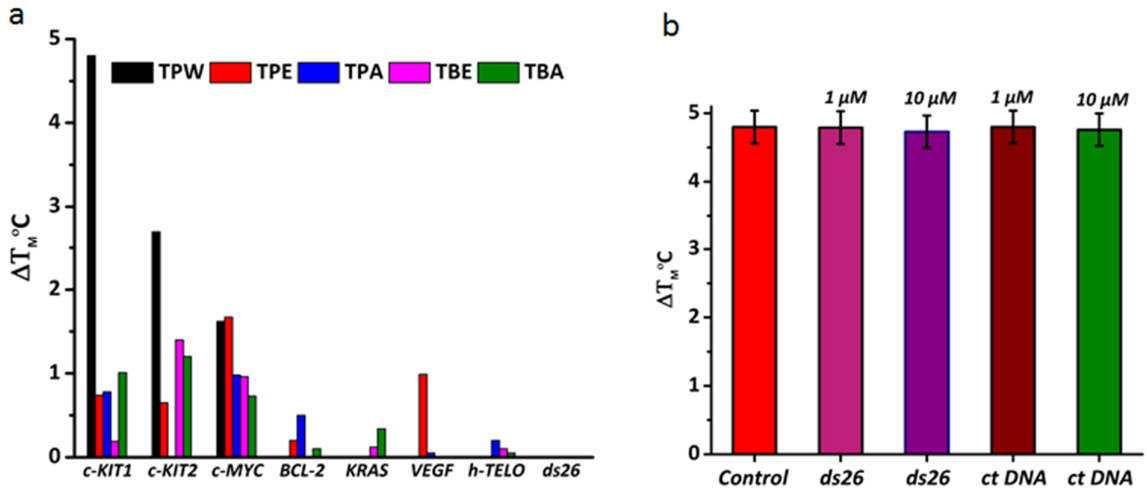

Figure 1A.2. (a) Thermal stabilization values (ΔT_M) of the G4s (*c-KIT1*, *c-KIT2*, *c-MYC*, *BCL-2*, *KRAS*, *VEGF*, *h-TELO*) and *ds26* DNA in presence of **TPW**, **TPE**, **TPA**, **TBE** and **TBA** at 1 μM concentration in 60 mM potassium cacodylate (K-Caco) buffer (pH 7.4). (b) FRET competition assay of **TPW** (1.0 μM) bound *c-KIT1* G4 (0.2 μM) [Control] in the presence of competitor *ds26* and *ct* (*calf thymus*) DNA (up to 50 equivalent con.) in 60 mM potassium cacodylate buffer (pH 7.4).

Fluorescence titrations

Fluorescence profile reveals that **TPW** exhibits a maximum at 355 nm upon excitation at 290 nm while **TPE** (λ_{ex} 325 nm) and **TPA** (λ_{ex} 290 nm) display maxima at 455 nm. **TBE** and **TBA** exhibit a fluorescence maximum at ~ 440 nm when excited at 290 nm. Fluorescence emission intensity of **TPW** altered significantly upon incremental addition of pre-annealed *c-KIT1* G4 DNA (Figure 1A.3). Remarkably, a new peak generated at 455 nm with a ~ 10-fold fluorescence enhancement (quantum yield, Φ = 0.094). Only moderate changes in fluorescence (~ 2 fold) were detected when **TPW** was titrated with *c-MYC* G4. However, no noticeable changes in fluorescence intensity were observed after adding sufficient concentrations (up to 5 μM) of other quadruplexes like *c-KIT2*, *KRAS*, *BCL-2*, *h-TELO* and *ds26* DNA.

Table 1.1. Fluorescence titration study to determine binding affinity (K_d) and fold intensities (F/F_0)

DNA[a]	TPW		TPE		TPA		TBE		TBA	
	K_d[b]	F/F_0[c]	K_d[b]	F_0/F[c]	K_d[b]	F/F_0[c]	K_d[b]	F/F_0[c]	K_d[b]	F/F_0[c]
c-KIT1	0.438	9.87	0.743	7.35	>30	1.56	n.d	1.25	19.72	1.20
c-KIT2	15.42	1.26	2.25	4.47	6.63	2.93	n.d	1.52	15.92	1.22
c-MYC	12.17	2.19	6.71	1.84	9.48	2.81	n.d	1.12	20.66	1.29
BCL-2	n.d	0.94	5.29	1.90	21.12	1.17	n.d	1.17	22.70	1.09
KRAS	19.09	1.24	0.972	7.13	17.02	1.39	n.d	1.26	19.72	1.20
h-TELO	n.d	0.98	3.85	3.20	17.80	1.39	n.d	1.54	19.33	1.28
ds26	n.d	1.2	2.8	4.41	14.32	1.50	n.d	2.18	19.89	1.08

[a]The oligonucleotides were pre-annealed in 60 mM potassium cacodylate buffer (pH 7.4)

[b]The binding affinity expressed in μM (K_d = ±5%)

[c]Fold change in terms of initial (F_0) and final (F) fluorescence intensity

The fluorescence maxima of **TPA, TBE** and **TBA** were not altered significantly in the presence of *c-KIT1* and other investigated quadruplexes. The changes in fluorescence intensity were used to determine the binding affinities of ligands for quadruplexes and *ds26* DNA. **TPW** displays a dissociation constant (K_d) value of *0.45* μM (determined by Hill1 equation) for the *c-KIT1* quadruplex (Table 1.1, Figure 1A.3). The K_d value of **TPW** for *BCL-2* quadruplex and *ds26* DNA could not be determined owing to the observed insignificant changes in its fluorescence upon their addition. Moreover, the K_d values of **TPW** for *c-KIT2* (*15* μM), *c-MYC* (*12* μM), and *KRAS* (*19* μM) were determined to be higher compared to *c-KIT1* G4. This suggests that **TPW** is highly selective towards *c-KIT1* G4 over other investigated G4s and *ds26* DNA.

The fluorescence intensity of **TPE** quenched up to ~7.4 fold and ~7.1 fold in the presence of *c-KIT1* (K_d = *0.74* μM) and *KRAS* (K_d = *0.97* μM) quadruplexes, respectively while ~ 4.5 fold quenching was observed with *c-KIT2* (K_d = 2.2 μM) and *ds26* (K_d = *2.8* μM) (Table 1.1, Figure 1A.4). **TPE** also displayed a K_d of *3.8* μM for *h-TELO*. These

results indicate that ligand **TPE** shows non-specific binding to all the studied G4s and *ds26* sequences. Thiazole ligands **TPA**, **TBE** and **TBA** showed insignificant changes in fluorescence intensity after titration with quadruplexes and *ds26* DNA and exhibited low K_d values for quadruplexes in comparison to **TPW** and **TPE** (Table 1.1). The K_d values of **TBE** for the quadruplexes and *ds26* DNA could not be determined owing to negligible changes in fluorescence after addition of pre-annealed quadruplexes and *ds26* DNA. Notably, despite **TPE** displayed comparable binding affinity for *c-KIT1*, **TPW** showed far greater selectivity towards this particular quadruplex DNA. These results indicate that **TPE**, containing ester end groups can also interact with DNA sequences. The affinity of **TPW** for the *c-KIT1* G-quadruplex was further analyzed by evaluating it´s ability to displace TO (thiazole-orange) from TO bound *c-KIT1* G4 (Figure 1A.4F).

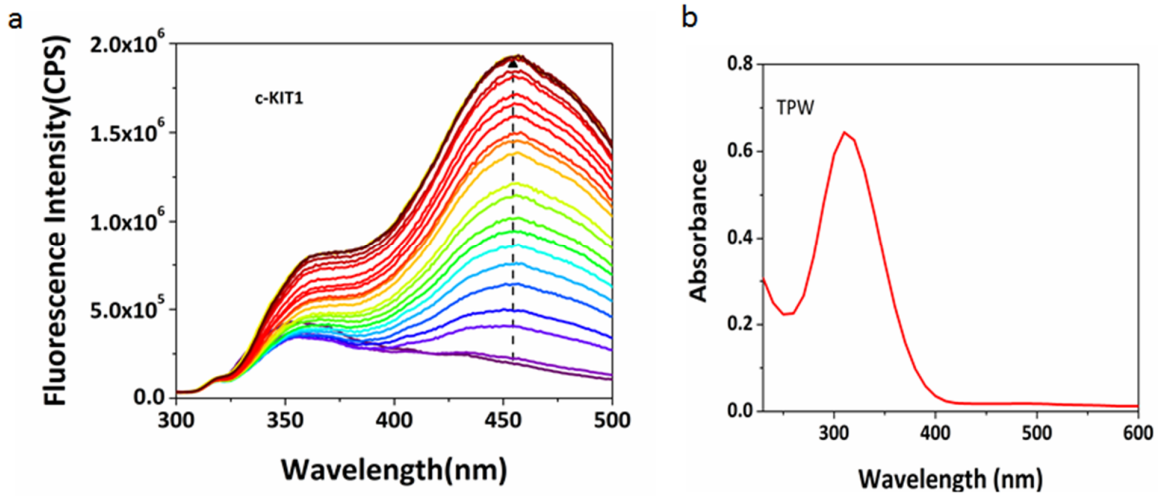

Figure 1A.3. (a) Fluorometric titration of **TPW** with *c-KIT1* G4 in the presence of 60 mM K-Caco buffer (pH 7.4). (b) Uv visible spectrum of **TPW**.

TPW exhibited a DC_{50} value of 0.88 µM for *c-KIT1* G4. This result is in accord with the fluorescence titration data suggesting it´s higher affinity for the *c-KIT1* G4. However, the DC_{50} value for other G4s could not be determined due to insignificant

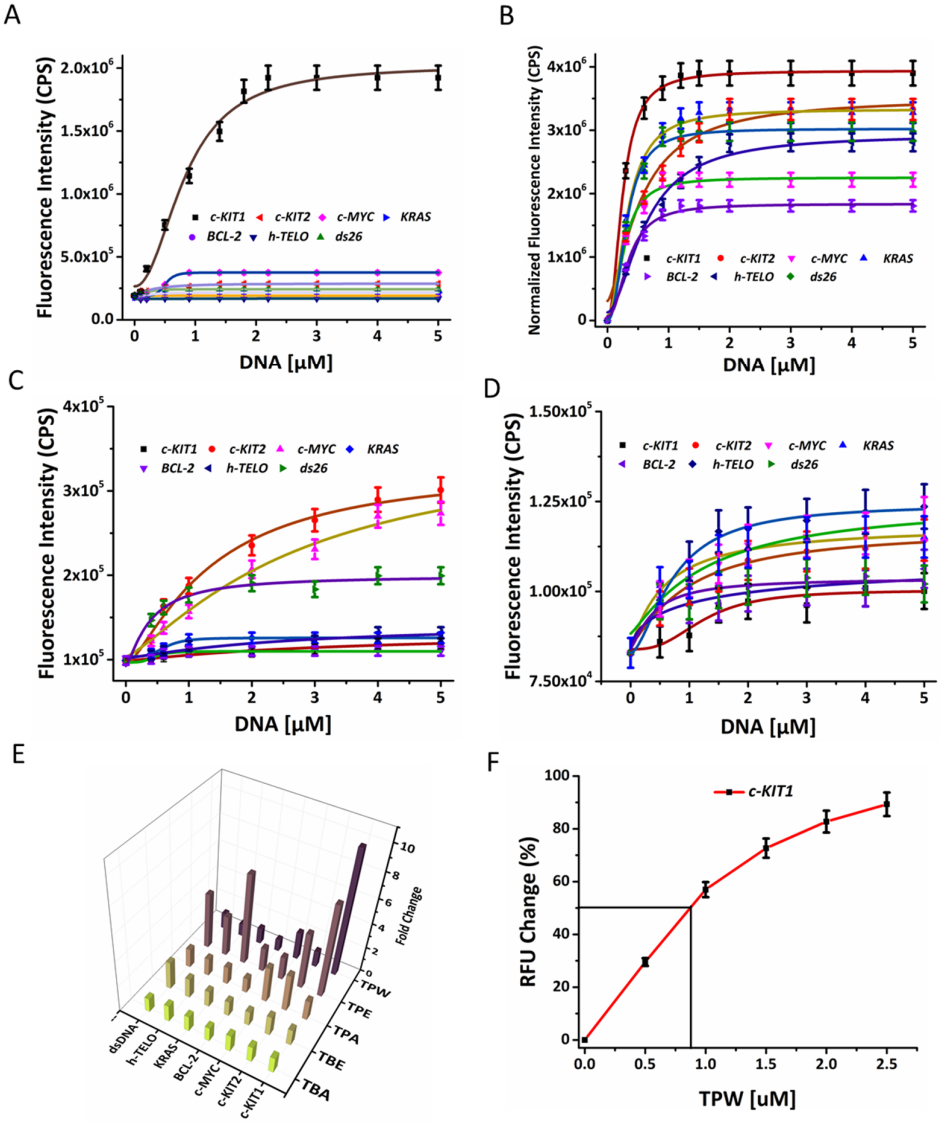

Figure 1A.4. Fluorometric titration of (A) **TPW** (10 µM) (B) **TPE** (10 µM), (C) **TPA** (10 µM), and (D) **TBA** (10 µM) in the presence of G4s (*c-KIT1*, *c-KIT*2, *c-MYC*, *KRAS*, *BCL-2*, *h-TELO*) and *ds26* DNA. (E) 3D Bar diagram showing fluorescence intensity fold change of **TPW**, **TPE**, **TPA**, **TBE** and **TBA** after addition of DNA up to 5 µM. (F) Thiazole orange displacement in terms of Relative Fluorescence Units (RFU) change (%) after titration of **TPW** with *c-KIT1* quadruplex.

Isothermal calorimetric titrations

In order to further validate the fluorescence data and obtain thermodynamic insights into the interaction of thiazole ligands with *c-KIT1* and other quadruplexes, isothermal titration calorimetry experiments were performed. These ligands differed significantly in their binding affinity towards quadruplexes and *ds26* DNA. Thermodynamic analysis revealed a typical sigmoidal binding isotherm of **TPW** for *c-KIT1* over other investigated quadruplexes and *ds26*. The binding isothermal profile was fitted using an appropriate binding site model. More importantly, the K_d value of **TPW** for *c-KIT1* determined using ITC (*0.69* μM) was in agreement with the K_d value obtained from fluorescence titration (Table 1.2, Figure 1A.5). In comparison, **TPW** possessed weak binding affinity for *c-KIT2* (K_d = *7.4* μM), *c-MYC* (K_d = *29* μM), *KRAS* (K_d = *5.5* μM), and *h-TELO* (K_d = *33* μM) (Table 1.2). However, the K_d values for *BCL-2* and *ds26* DNA could not be obtained from the binding isotherms of **TPW**. Besides that, **TPW** possessed most favorable binding energy i.e., Gibbs free energy (ΔG = -8.40 kcal/mol) for *c-KIT1* quadruplex, which signifies spontaneous interaction of **TPW** with *c-KIT1* and it´s high specificity towards *c-KIT1* over other quadruplexes and *ds26*.[45, 46] As shown in Table 1.2, **TPE** displayed more binding affinity towards *c-KIT1* (K_d = *4.7* μM) compared to other quadruplexes. However, calorimetric data revealed that **TPE** shows a binding affinity of *3.8* μM for *ds26* DNA, indicating more affinity towards

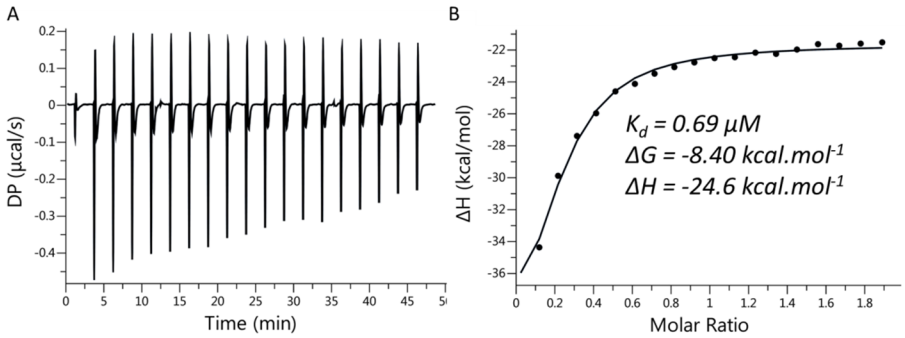

Figure 1A.5. Representative binding isotherms for the binding of **TPW** with the *c-KIT1* G4 monitored through ITC in the presence of 60 mM potassium cacodylate buffer (pH 7.4) at 25 ℃. (A) Heat burst curves and (B) the equilibrium K_d obtained through fitting the raw data.

Table 2. Thermodynamic parameters obtained from Isothermal calorimetry (ITC) titrations

		c-KIT1	***c-KIT2***	***c-MYC***	***BCL-2***	***KRAS***	***h-TELO***	***ds26 DNA***
TPW	K_d (µM)	*0.69±0.03*	*7.4±0.39*	*29±1.4*	*n.d*	*5.5±0.28*	*33±1.6*	*n.d*
	ΔG (kcal.mol^{-1})	-8.40	-7	-6.20	n.d	-7.21	-6.11	n.d
	N (sites)	1.01	1.59	1.8	n.d.	0.82	2.1	n.d
TPE	K_d (µM)	*4.2±0.2*	*36±1.8*	*13±0.64*	*16±0.8*	*15±0.73*	*291±14*	*3.8±0.19*
	ΔG (kcal.mol^{-1})	-7.34	-6.03	-4.30	-6.55	-6.60	-4.6	-7.40
	N (sites)	1.13	1.71	1.38	1.46	1.41	2.6	1.16
TPA	K_d (µM)	*9.8±0.49*	*18±0.91*	*21±1.06*	*12±0.62*	*n.d*	*n.d*	*26±1.31*
	ΔG (kcal.mol^{-1})	-6.83	-6.47	-6.38	-6.69	n.d	n.d	-6.25
	N (sites)	0.96	1.31	1.33	1.17	n.d	n.d	1.42
TBE	K_d (µM)	*22±1.1*	*27±1.3*	*35±1.7*	*n.d*	*21±1*	*17±0.87*	*33±1.63*
	ΔG (kcal.mol^{-1})	-6.34	-4.7	-6.08	n.d	-6.38	-6.49	-6.12
	N (sites)	1.28	1.43	1.47	n.d	1.19	1.08	1.37
TBA	K_d (µM)	*30±1.5*	*n.d*	*17±0.86*	*31±1.5*	*12.0±0.6*	*21±1*	*n.d*
	ΔG (kcal.mol^{-1})	-6.16	n.d	-6.50	-6.14	-6.72	-6.39	n.d
	N (sites)	1.67	n.d	1.53	1.76	1.44	1.54	n.d

ds26 DNA and non-specific interaction for investigated quadruplexes (Table 1.2). However, the other three compounds **TPA**, **TBE** and **TBA** do not exhibit any significant binding affinities and binding energy values for the investigated quadruplexes (Table 1.2). These results suggest that **TPW** shows superior selectivity for *c-KIT1* quadruplex with greater binding affinity compared to other quadruplexes and *ds26* DNA. ITC data also show that **TPW** binds to the *c-KIT1* G4 with a ~1:1 stoichiometry. Moreover, the total binding enthalpy (the sum of individual enthalpic values from the fits) was negative for the interaction of this thiazole series with all the G4s and *ds26* DNA, suggesting that the entire process was enthalpically favorable.[47]

Biophysical assays revealed that the polyamide **TPW** showed selective and potent electrostatic interactions with *c-KIT1* G4 and **TPE** exhibited non-specific interactions with the G4s and *ds26*. Consequently, both **TPW** and **TPE** were examined for cytotoxicity profile and oncogene regulatory roles in cancer cells by cell viability (XTT) assay, confocal microscopy, quantitative real time PCR (qRT-PCR), immunoblot and luciferase reporter assays.

Growth inhibition analysis of TPW and TPE in Cells

We evaluated the IC_{50} values of **TPW** and **TPE** in cancer cells and normal cells. **TPW** and **TPE** exerted IC_{50} values of ~ 70 µM and ~ 95 µM in myeloid leukemia (K562) cells after 24 hours of treatment, respectively. After longer incubation

period of 72 hrs, **TPW** and **TPE** showed IC_{50} values of 48 µM and 63 µM in leukemia cells. They displayed >80 µM IC_{50} values for breast cancer (MCF-7) and lung carcinoma (A549) cell lines after 72 hrs of incubation period. Both ligands did not show inhibitory activity on normal kidney epithelial (NKE) cells up to 200 µM. Cell cycle analysis also revealed that **TPW** causes cell cycle arrest at the rate of 7% and 3.5% in S phase and G2/M phase of K562 cells respectively, at 40 µM.

TPW co-localizes with BG4 antibody inside cancer cells

Cellular localization & Immunofluorescence

Confocal imaging revealed that **TPW** can efficiently enter into cancer cell nuclei and exhibit high fluorescence. It is worth noting that the fluorescence of **TPW** increased significantly inside the cellular nuclei which might be due to the interactions of **TPW** with G4s. Owing to the fluorescence enhancement property of **TPW** inside the cell nuclei, it can be used as a nucleus labeling probe in cancer cells.

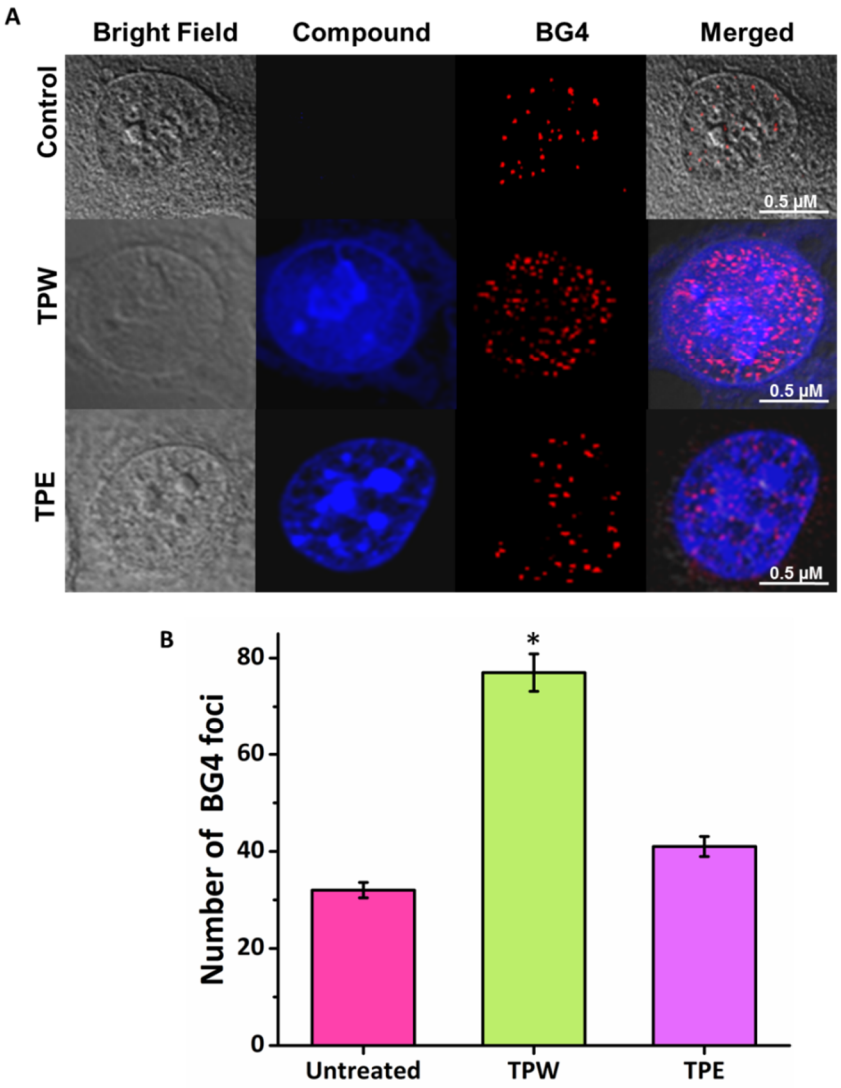

Figure 1A.6. (A) Confocal images of HeLa cell nuclei (fixed) stained with **TPW (blue)**, **TPE (blue)** and **BG4 (red)**. (B) Quantification of BG4 foci per nucleus. For the analysis, >50 cells were counted and the standard error of the mean was calculated from three replicates. *P <0.05 (Student's 't' test).

To demonstrate whether **TPW** could enter into nucleus and bind G4s, an immunofluorescence assay (Figure 1A.6) with BG4, a well-known G4 specific antibody was performed in HeLa cells.[48] As revealed in Figure 1A.6, the

immunofluorescence images of HeLa cells show that **TPW** efficiently entered and localized into the nucleus. The number of BG4 foci significantly increased after treatment with **TPW** as compared to untreated or control cells, indicating the ability of **TPW** to stabilize G4s at pertinent sites (Figure 1A.6B). Confocal images further reveal that ligand **TPE** can also penetrate the cell membrane and localize into nucleus. However, **TPE** could stabilize less number of BG4 foci in comparison to **TPW**. It may be due to it´s non-specific interactions with DNAs and fluorescence quenching property as observed in the fluorescence experiment.

TPW preferentially down-regulates *c-KIT* expression in K562 cells

Gene expression analysis

The gene regulatory role of both **TPW** and **TPE** on well-known G4-driven genes *c-KIT*, *c-MYC* and *BCL-2* were evaluated in K562 cells by quantifying mRNA steady-state levels using quantitative real-time PCR (Figure 1A.7A,7B). The results illustrate that **TPW** selectively represses *c-KIT* expression at m-RNA level in myeloid leukemia cells. The *c-KIT* expression level decreased significantly by 43% and 77% after treatment with **TPW** at two different doses 20 µM and 40 µM, respectively (Figure 1A.7B). In comparison, **TPW** minimally affected the *c-MYC* and *BCL-2* expression. However, **TPE** upregulated *c-KIT* expression slightly by ~ 2% and ~ 9% at similar concentrations of 20 µM and 40 µM, respectively.

Unexpectedly, **TPE** could also raise the *c-MYC* and *BCL-2* expression levels up to ~ 80% and 30% respectively, at 40 µM (Figure 1A.7B).

Luciferase reporter assay

To investigate whether the effects of **TPW** and **TPE** on *c-KIT* expression were consequent to their binding with *KIT* promoter, the modulation on luciferase activity was studied using *c-KIT* wild promoter and pRL-TK constructs (Figure 1A.7C,7D). In addition, luciferase activity of *c-MYC* and *BCL-2* was also investigated to understand the specificity of ligands for a particular promoter. The pRL-TK construct does not harbor G4 sequences and it is independent of G4 mediated regulation. The normalization of *c-KIT*, *c-MYC* and *BCL-2* promoter luciferase expression was accomplished with pRL-TK expression.

Apparently, **TPW** decreased the luciferase expression in a dose dependent manner for *c-KIT* promoter construct. **TPW** at two different concentrations of 20 µM and 40 µM exhibited ~ 25% and ~ 66% reduction in luciferase activity, respectively for *c-KIT* promoter, while negligible or no changes were observed for *c-MYC* and *BCL-2* expression (Figure 1A.7C). However, **TPE** (at 40 µM concentration) increased *c-MYC* and *BCL-2* luciferase expression up to ~ 48% and ~ 40%, respectively. A mild increase in *c-KIT* expression (~ 10%) was also monitored at

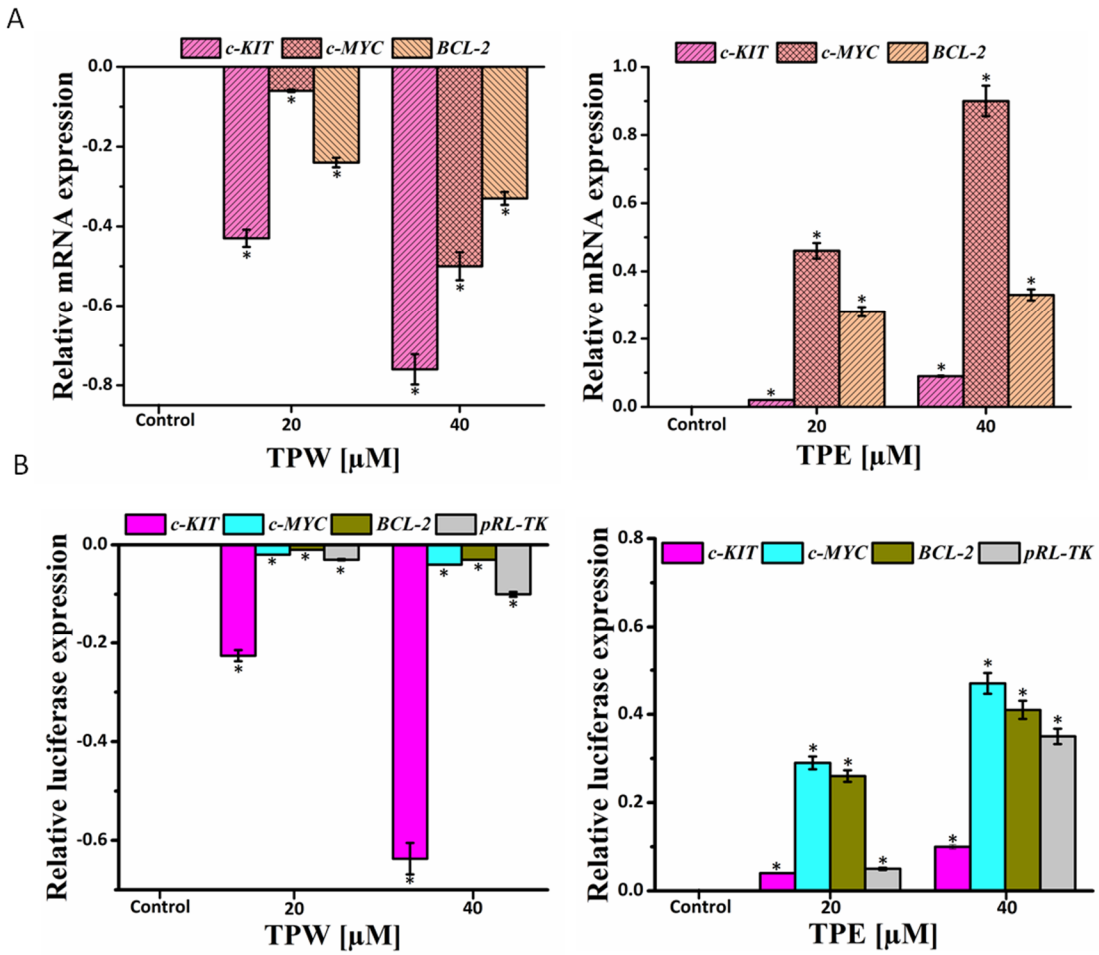

Figure 1A.7. (a) qRT-PCR analysis for transcriptional regulation of *c-KIT*, *c-MYC* and *BCL-2* after treatment with **TPW** or **TPE** in leukemia cells (K562) for 24 h. Quantification was done in terms of fold change by double delta C_T method using 18s rRNA or GAPDH as housekeeping or reference gene. Fold change of ligand treated relative gene expression is normalized with control or untreated value of 0. Three biological replicates were employed for the quantifications. Error bars represent mean ±SD.*P<0.05 (Student's t test), versus control or untreated leukemia cells. (b) Relative luciferase expression of *c-KIT*, *c-MYC* and *BCL-2* promoters normalized with the Renilla plasmid pRL-TK after treatment with **TPW** or **TPE** at two different doses for 48 h. Fold change of ligand treated relative luciferase expression is normalized with control or untreated value of 0. Error bars correspond to mean ±SD. *P<0.05 (Student's t test), versus untreated leukemia cells.

the highest dose of **TPE** (Figure 1A.7D). These results point towards the ability of **TPW** to inhibit *c-KIT* oncogene expression via its effective interactions with the

promoter G-quadruplex. The observed up-regulation by **TPE** might be the result of its non-specific interaction and downstream biological effect inside the cancer cells. The detailed molecular mechanism for up-regulatory effects of **TPE** will be further studied in future.

Western blot.

In order to substantiate the alteration in mRNA levels by **TPW** and **TPE**, immunoblotting was performed to examine whether there were any significant changes in *c-KIT*, *c-MYC* and *BCL-2* expression at protein levels (Figure 2A.8). *c-KIT* protein levels were significantly reduced by ~ 0.5 fold (i.e., decreased by 50%) and ~ 0.7 fold (i.e., decreased by 70%) in leukemia cells following treatment with **TPW** at two different doses of 20 µM and 40 µM, respectively. However, **TPW** did not cause any noticeable change in *c-MYC* protein expression while a mild down-regulation in *BCL-2* expression (~ 20%) was observed at highest dose (40 µM) treatment. In agreement with qRT-PCR results, up-regulation of *c-KIT*, *c-MYC* and *BCL-2* genes at protein levels was detected after treatment with **TPE** (20 µM and 40 µM). The expression of *c-KIT*, *BCL-2* and *c-MYC* genes were augmented by ~ 0.4 fold, ~ 0.7 fold and ~ 0.9 fold (i.e., increased by 40%, 70% and 90%) respectively at 40 µM of **TPE**. Almost no change in protein expression was observed in case of housekeeping gene *GAPDH* after treatment with **TPW** and

TPE. These results signify that **TPW** selectively down-regulates *c-KIT* protein expression.

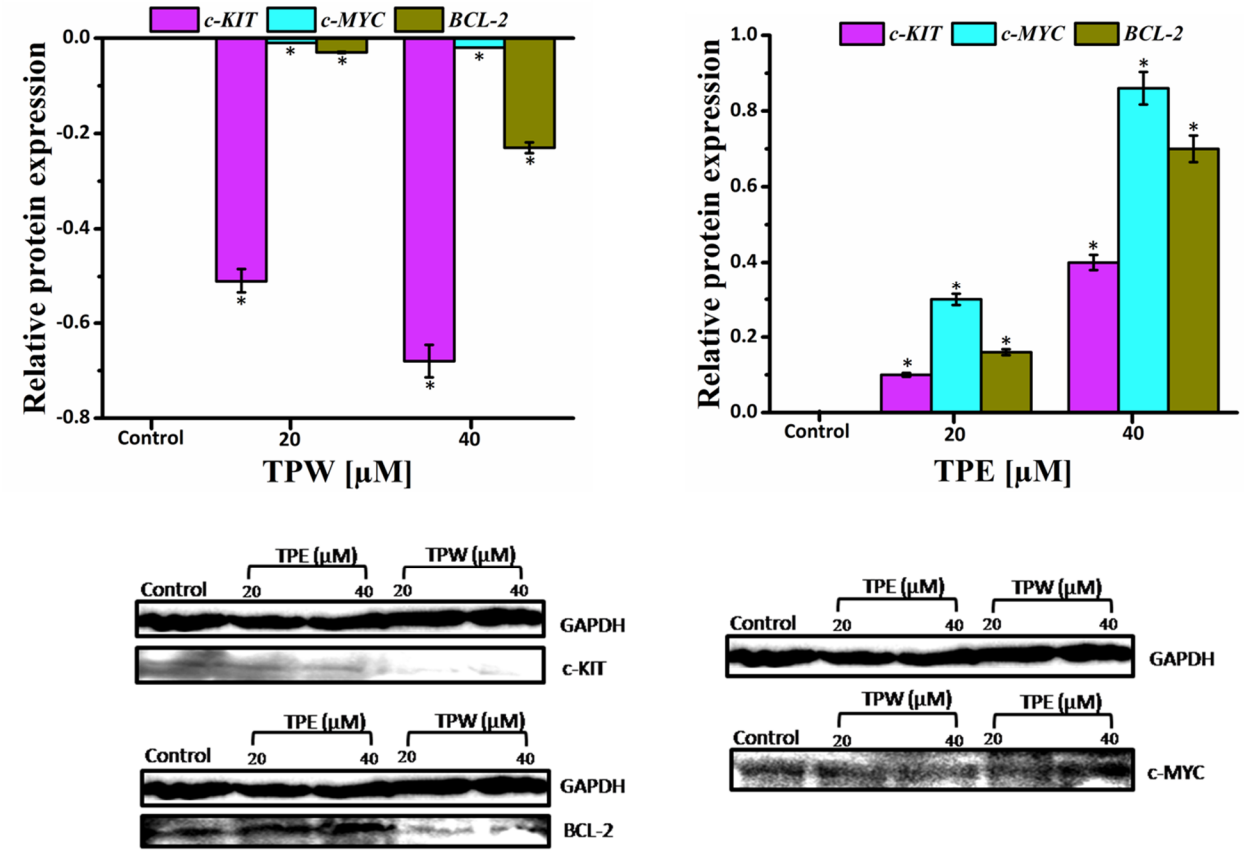

Figure 1A.8. Western blot analysis for monitoring relative protein expression of *c-KIT*, *c-MYC* and *BCL-2* by densitometric analysis of immunoreactive bands after treatment with **TPW** or **TPE** in K562 cells for 24 h. Fold change of ligand treated relative protein expression is normalized with control or untreated value of 0. Error bars correspond to mean ±SD. *P<0.05 (Student's t test), versus leukemia cells.

Structure-activity relationship

In order to understand the possible binding mode, docking studies of **TPW** and **TPE** were performed with *c-KIT1* (PDB: 4WO2), *c-KIT2*, *c-MYC*, *BCL-2*, *KRAS*,

h-TELO G4s (Figure 1A.9). Both **TPW** and **TPE** possessed an extended conformation following energy minimization while the structures were found to adopt constrained topologies after interacting with the quadruplexes. The docking results illustrate that **TPW** can effectively stack on the 5′ end of *c-KIT1* G4 with a lowest binding energy (- 9.317 kcal.mol^{-1}) compared to other investigated G4s. However, **TPE** also binds to the *c-KIT1* G4 via stacking mode of interactions but with higher energy (- 4.49 kcal.mol^{-1}) as compared to **TPW**.

Modeling studies further revealed that thiazole-pyridine units of **TPW** occupy a larger plane of the G-quartet and the amine side chains participate in electrostatic interactions with the phosphate backbone. The docking results further reinforce our experimental data that thiazole incorporated molecule with water soluble amine side chains preferentially binds to *c-KIT1* G4 with 1:1 stoichiometry. Even though the G4 structures (*c-KIT1*, *c-KIT*2, *c-MYC, KRAS* and *BCL-2*) except *h-TELO*, employed in this work possess parallel topology, the intervening loop sequences and flanking areas (capping structures) are different. The alkyl amine-containing side chains of **TPW** play a critical role for the selective recognition of *c-KIT1* G4, due to favourable electrostatic interactions with negatively charged phosphate backbone in the groove regions of *KIT1* G4.

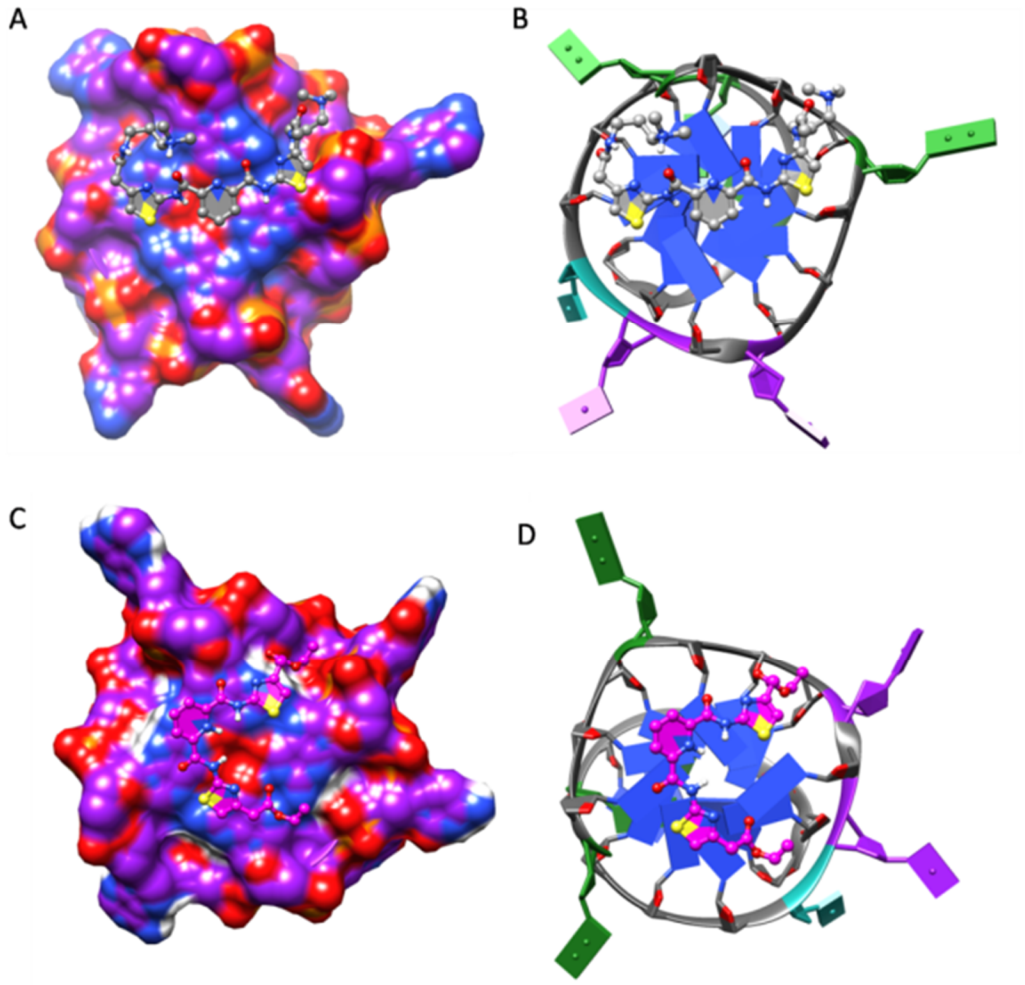

Figure 1A.9. Molecular docking of **TPW** with *c-KIT1* (A, B) (energy = -9.317 kcal.mol^{-1}) and **TPE** with *c-KIT1* (C, D) (energy = -4.49 kcal.mol^{-1}) obtained from Autodock 4.0. Ligands (shown in stick and ball mode) stacked on a terminal G-quartet, represented as hydrophobic surface. **TPW** and **TPE** were represented in dim gray and magenta color respectively.

Conclusion

A novel and less-toxic G4 binding small molecule **TPW** selectively detects *c-KIT1* G4 and transcriptionally inhibits *c-KIT* expression in leukemia cells. This polyamide ligand containing a pyridine unit and two thaizoles preferentially targets nuclei structures and emit high fluorescence inside the cell nuclei. The expansion

of such less-toxic molecules could serve as alternatives to extremely cytotoxic molecules, often used for diagnostic and therapeutic purposes. Specific targeting of genes with this class of compounds could improve bioavailability and further, their low toxicity could reduce adverse effects in cellular system. Such molecules with the potential to recognize complex biological systems could open up new avenues for the development of novel molecular agents for cancer.

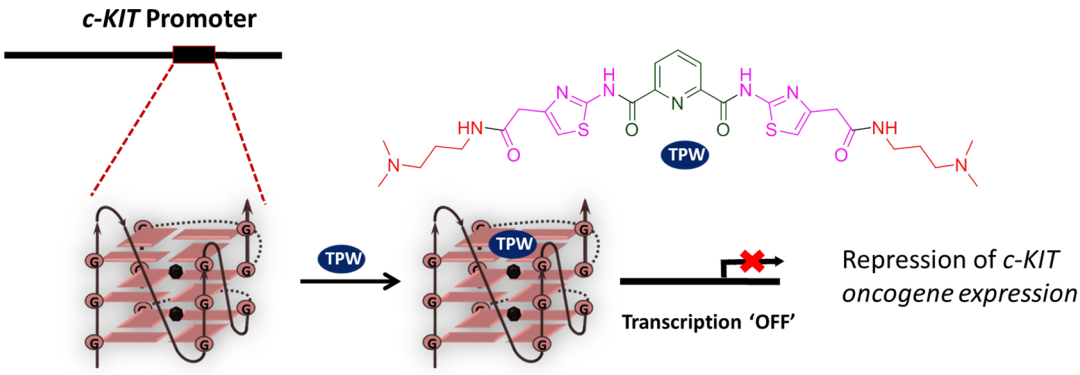

Scheme 1A.2. Schematic representation of **TPW** mediated repression of *c-KIT* oncogene expression.

References

1. M.-H. Hu, J. Zhou, W.-H. Luo, S.-B. Chen, Z.-S. Huang, R. Wu, J.-H. Tan, *Anal. chem.* **2019,** *91*, 2480-2487.
2. S. Balasubramanian, L. H. Hurley, S. Neidle, *Nat. Rev. Drug Discov.* **2011,** *10*, 261.
3. S. Mandal, Y. Kawamoto, Z. Yue, K. Hashiya, Y. Cui, T. Bando, S. Pandey, M. E. Hoque, M. A. Hossain, H. Sugiyama, *Nucleic Acids Res.* **2019,** *47*, 3295-3305.
4. A. P. David, A. Pipier, F. Pascutti, A. Binolfi, J. Weiner, M. Andrea, E. Challier, S. Heckel, P. Calsou, D. Gomez, *Nucleic Acids Res.* **2019.**
5. M. L. Bochman, K. Paeschke, V. A. Zakian, *Nat. Rev. Genet.* **2012,** *13*, 770.
6. E. Y. N. Lam, D. Beraldi, D. Tannahill, S. Balasubramanian, *Nat. Commun.* **2013,** *4*, 1796.
7. K. V. Diveshkumar, S. Sakrikar, F. Rosu, S. Harikrishna, V. Gabelica, P. Pradeepkumar, *Biochemistry* **2016,** *55*, 3571-3585.
8. J. Amato, L. Cerofolini, D. Brancaccio, S. Giuntini, N. Iaccarino, P. Zizza, S. Iachettini, A. Biroccio, *Nucleic Acids Res.* **2019**, *47*, 9950-9966.
9. T. Frelih, B. Wang, J. Plavec, P. Šket, *Nucleic Acids Res.* **2020,** *48*, 2189-2197.
10. S. Jonchhe, C. Ghimire, Y. Cui, S. Sasaki, M. McCool, S. Park, K. Iida, K. Nagasawa, H. Sugiyama, H. Mao, *Angew. Chem. Int. Ed.* **2019,** *58*, 877-881.
11. A. l. Laguerre, L. Stefan, M. Larrouy, D. Genest, J. Novotna, M. Pirrotta, D. Monchaud, *J. Am. Chem. Soc.* **2014,** *136*, 12406-12414.
12. X. Wang, C.-X. Zhou, J.-W. Yan, J.-Q. Hou, S.-B. Chen, T.-M. Ou, L.-Q. Gu, Z.-S. Huang, J.-H. Tan, *ACS Med. Chem. Lett.* **2013,** *4*, 909-914.

13. M. Zuffo, A. Guédin, E.-D. Leriche, F. Doria, V. Pirota, V. Gabelica, J.-L. Mergny, M. Freccero, *Nucleic Acids Res.* **2018,** *46*, e115-e115.

14. S. Asamitsu, T. Bando, H. Sugiyama, *Chem. Eur.* **2019,** *25*, 417-430.

15. A. Minard, D. Morgan, F. Raguseo, A. Di Porzio, D. Liano, A. G. Jamieson, M. Di Antonio, *Chem Commun.* **2020,** *56*, 8940-8943.

16. B. Zheng, M.-T. She, W. Long, Y.-Y. Xu, Y.-H. Zhang, X.-H. Huang, W. Liu, J.-Q. Hou, W.-L. Wong, Y.-J. Lu, *Chem Commun.* **2020**

17. P. Chilka, N. Desai, B. Datta, *Molecules* **2019,** *24*, 752.

18. J. Dash, P. S. Shirude, S.-T. D. Hsu, S. Balasubramanian, *J. Am. Chem. Soc.* **2008,** *130*, 15950-15956.

19. M. Nadai, F. Doria, M. Scalabrin, V. Pirota, V. Grande, G. Bergamaschi, V. Amendola, F. R. Winnerdy, A. T. n. Phan, S. N. Richter, *J. Am. Chem. Soc.* **2018,** *140*, 14528-14532.

20. A. D. Moorhouse, A. M. Santos, M. Gunaratnam, M. Moore, S. Neidle, J. E. Moses, *J. Am. Chem. Soc.* **2006,** *128*, 15972-15973.

21. A. Głuszyńska, B. Juskowiak, M. Kuta-Siejkowska, M. Hoffmann, S. Haider, *Molecules* **2018,** *23*, 1134.

22. S. Asamitsu, S. Obata, Z. Yu, T. Bando, H. Sugiyama, *Molecules* **2019,** *24*, 429.

23. L. K. Ashman, R. Griffith, *Expert opinion on investigational drugs* **2013**, *22*, 103-115.

24. M. Bejugam, M. Gunaratnam, S. Müller, D. A. Sanders, S. Sewitz, J. A. Fletcher, S. Neidle, S. Balasubramanian, *ACS Med. Chem. Lett.* **2010,** *1*, 306-310.

25. D. Wei, J. Husby, S. Neidle, *Nucleic Acids Res.* **2014,** *43*, 629-644.

26. K. I. McLuckie, Z. A. Waller, D. A. Sanders, D. Alves, R. Rodriguez, J. Dash, G. J. McKenzie, A. R. Venkitaraman, S. Balasubramanian, *J. Am. Chem. Soc.* **2011,** *133*, 2658-2663.

27. X. Xia, Y.-C. Lo, A. A. Gholkar, S. Senese, J. Y. Ong, E. F. Velasquez, R. Damoiseaux, J. Z. Torres, *ACS Chem. Biol.* **2019.**

28. T. Furitsu, T. Tsujimura, T. Tono, H. Ikeda, H. Kitayama, U. Koshimizu, H. Sugahara, J. H. Butterfield, L. K. Ashman, Y. Kanayama, *J Clin Investig.* **1993,** *92*, 1736-1744.

29. E. Weisberg, P. W. Manley, S. W. Cowan-Jacob, A. Hochhaus, J. D. Griffin, *Nat. Rev. Cancer.* **2007,** *7*, 345-356.

30. Q.-L. Guo, H.-F. Su, N. Wang, S.-R. Liao, Y.-T. Lu, T.-M. Ou, J.-H. Tan, D. Li, Z.-S. Huang, *Eur. J. Med. Chem.* **2017,** *130*, 458-471.

31. R. Rigo, C. Sissi, *Biochemistry* **2017,** *56*, 4309-4312.

32. C. Ducani, G. Bernardinelli, B. r. Högberg, B. K. Keppler, A. Terenzi, *J. Am. Chem. Soc.* **2019,** *141*, 10205-10213.

33. A. T. Phan, V. Kuryavyi, S. Burge, S. Neidle, D. J. Patel, *J. Am. Chem. Soc.* **2007,** *129*, 4386-4392.

34. P. S. Shirude, B. Okumus, L. Ying, T. Ha, S. Balasubramanian, *J. Am. Chem. Soc.* **2007,** *129*, 7484-7485.

35. Z. A. Waller, S. A. Sewitz, S.-T. D. Hsu, S. Balasubramanian, *J. Am. Chem. Soc.* **2009,** *131*, 12628-12633

36. A. Chauhan, S. Paladhi, M. Debnath, S. Mandal, R.N. Das, S. Bhowmik and J. Dash, *Bioorg. Med. Chem* **2014**, *22*, 4422-4429.

37. S. Rankin, A. P. Reszka, J. Huppert, M. Zloh, G. N. Parkinson, A. K. Todd, S. Ladame, S. Balasubramanian, S. Neidle, *J. Am. Chem. Soc.* **2005,** *127*, 10584-10589.

38. G. Padroni, J. A. Parkinson, K. R. Fox, G. A. Burley, *Nucleic Acids Res.* **2018,** *46*, 42-53.

39. M. J. Cocco, L. Hanakahi, M. D. Huber, N. Maizels, *Nucleic Acids Res.* **2003,** *31*, 2944-2951.

40. M. A. Marques, R. M. Doss, S. Foister, P. B. Dervan, *J. Am. Chem. Soc.* **2004,** *126*, 10339-10349.

41. D. Dutta, M. Debnath, D. Müller, R. Paul, T. Das, I. Bessi, H. Schwalbe, J. Dash, *Nucleic Acids Res.* **2018,***46*, 5355-5365.

42. P. C. Sharma, K. K. Bansal, A. Sharma, D. Sharma, A. Deep, *Eur. J. Med. Chem.* **2020,** *188*, 112016.

43. X. Xie, B. Choi, E. Largy, R. Guillot, A. Granzhan, M. P. Teulade-Fichou, *Chem. Eur.* **2013**, *19*, 1214-1226.

44. J.-L. Mergny, L. Lacroix, M.-P. Teulade-Fichou, C. Hounsou, L. Guittat, M. Hoarau, P. B. Arimondo, J.-P. Vigneron, J.-M. Lehn, J.-F. Riou, T. Garestier, C. Hélène, *Proc. Natl. Acad. Sci. U. S. A.* **2001,** *98*, 3062-3067.

45. J. S. Hudson, L. Ding, V. Le, E. Lewis, D. Graves, *Biochemistry* **2014,** *53*, 3347-3356.

46. J. Amato, B. Pagano, N. Borbone, G. Oliviero, V. Gabelica, E. D. Pauw, S. D'Errico, V. Piccialli, M. Varra, C. Giancola, *Bioconjugate Chem*. **2011,** *22*, 654-663.

47. M. Bončina, Č. Podlipnik, I. Piantanida, J. Eilmes, M.-P. Teulade-Fichou, G. Vesnaver, J. Lah, *Nucleic Acids Res.* **2015,** *43*, 10376-10386.

48. M. Di Antonio, A. Ponjavic, A. Radzevičius, R. T. Ranasinghe, M. Catalano, X. Zhang, J. Shen, L.-M. Needham, S. F. Lee, D. Klenerman, *Nat. Chem.* **2020,** 1-6.

Chapter 1B

Targeting c-MYC oncogenic G4 by thiazole based peptidomimetics

Since last few decades, steering the DNA structures by small molecules has evolved into a graceful approach to pause the transcription machinery of cancer cells, which has been turned out to be a useful strategy to advance the therapeutics and diagnostics for cancer.[1-3] Except double stranded structures of DNA, guanine (G)-rich quadruple DNA motifs are abundant in oncogenic promoters (*c-MYC*, *BCL-2*, *c-KIT*, *KRAS)* and telomeres (*h-TELO*) of cancer cells; named as G-quadruplexes (G4s).[4,5] Despite being dynamic structures, such G4 structures can be targeted with higher affinity and selectivity with artificial ligands.

Cancer cells have been found to have proto-oncogenes *MYC*, one of the key proto-oncogenes, which are believed to overexpress in ~ 80% of all cancer types. The regulation of *MYC* is pivotal for proliferation, differentiation, apoptosis, tumor progression and drug resistance in cancer cells.[6-8] *MYC* acts like a transcriptional accelerator in cancer cells and repressing the *MYC* oncogene can cause inhibition of tumor growth and induction of tumor regression permanently.[9-12] For such rationale, *MYC* holds wide interest as a major target in anticancer therapeutics.[12-14] The NHE (nuclease hypersensitive element) III_1 of *MYC* promoter, thatregulates the transcriptional activity (~ 90%), harbors a G4 forming sequencewhich acts like a transcriptional repressor.[12-18] G4s are four stranded nucleic acid secondary structures shaped by stacked G-quartet in the presence of K^+ or Na^+ like monovalent cations.[19-21]

Stabilization of those G4 structures present in oncogene promoters by small molecules has emerged as a potential strategy towards the drug development for cancer therapeutics and diagnostics.[22-24] Synthetic ligands that stabilize the *MYC* G4s can hinder the progression of *MYC* and thus could induce apoptosis and impede the growth of cancer cells. Even though, a series of molecules (e.g., BRACO-19, carbazole derivatives, thiazole derivatives etc.) have been reported to stabilize *MYC* G4s, the binding affinity and selectivity are a major concern for drug discovery.[25,26] However, over the last decade, peptidomimetic ligands have found more attention towards the development of cancer therapeutics due to their cell membrane permeability and selective toxicity for cancer cells.[26-29]

In this section, a thiazole based peptide ligand **TBT1** has been designed to investigate its G4 binding potential followed by subsequent modulation of oncogene expression in cancer cells. FRET based melting analysis shows the highest stabilization potential of **TBT1** for *MYC* G4 and fluorescence spectroscopy revealed that it possesses the highest and selective binding affinity towards *MYC* over other investigated G4s and *dsDNA*. **TBT1** shows potent toxicity towards cancer cells as demonstrated by cell growth inhibition (XTT) assay. This work provides the insights on structure specific G4 recognition by a thiazole peptide and anticancer activity in cancer cells.

Melting assay by FRET

The stabilization property of the thiazole peptidomimetic ligands (**TBT1-TBT6**) for G4s was evaluated by FRET based melting assays on a panel of 5'-FAM and 3'-TAMRA tagged DNA oligo sequences. This high throughput method quantified the stabilization induced by the ligand for the G4s and *ds26* DNA, by comparing the melting temperature pre and post complexation.

An overall highest stabilization for *c-MYC* G4 was observed at the low concentration of 0.5 to 1 µM. **TBT1** displayed the stabilization potential for the *c-MYC* G4 with a ΔT_M value of ~18.3 $^{\circ}$C. Lower or no measurable ΔT_M values were observed with dual labeled other quadruplexes and *ds26* DNA. Hairpin *ds26* DNA did not display any increase in stabilization at low concentration, although measurable stabilizations were recognized with higher ligand quantities. In order to attain analogous ΔT_M values with compound **TBT1**, the concentration was increased to 5 µM, equivalent to 10-fold the amount of DNA (Figure 1B.1A). Besides that, the 3D plot (Figure 1B.1B) provides fascinating information on its easily comparable stabilization property for G4s over duplex DNA. Indeed, no stabilization was observed for duplex DNA even at such a high ligand concentration.

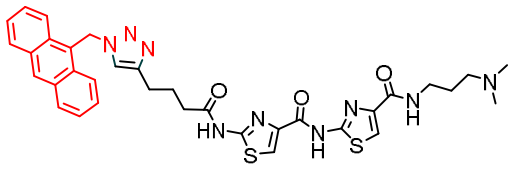

TBT1

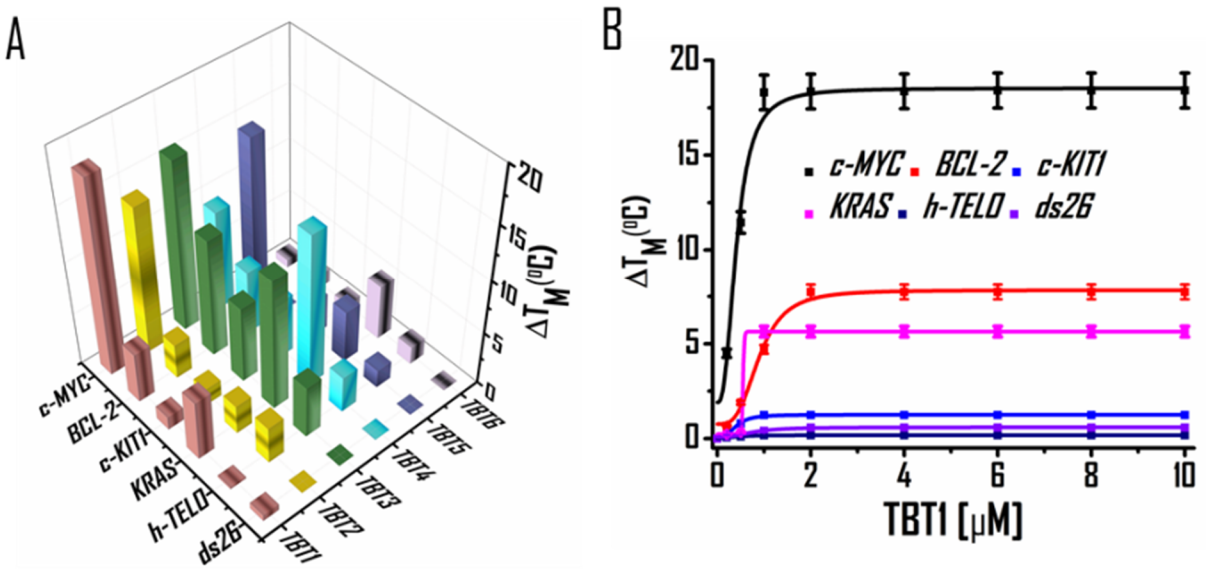

Figure 1B.1. (A) 3D plot of thermal stabilization profile (ΔT_M) of the G4s (*c-MYC*, *BCL-2*, *c-KIT1*, *KRAS*, *h-TELO*) and *ds26* DNA in the presence of peptidomimetic ligands at 2 μM concentration in 60 mM potassium cacodylate (K-Caco) buffer (pH 7.4). (B) FRET titration of **TBT1** with the G4s (*c-MYC*, *BCL-2*, *c-KIT1*, *KRAS*, *h-TELO*) and *ds26* DNA in 60 mM potassium cacodylate (K-Caco) buffer (pH 7.4).

Fluorometric titration

The thiazole peptide ligands were screened for their binding properties upon interaction with the *Pu22* c-*MYC*, *BCL-2*, *c-KIT1*, *KRAS*, *h-TELO* G4 DNA and *dsDNA* structures via fluorescence based titration (Figure 1B.2). **TBT2**, **TBT3**, **TBT4**, **TBT5** and **TBT6** only showed negligible or no changes in fluorescence after subsequent addition of either the G4s or *dsDNA*. On the contrary, **TBT1** displays interesting fluorescence properties, showed a ~1.6 -fold decrease in fluorescence followed by ~2.5 fold increase upon binding with *Pu22 c-MYC* G4 DNA structure. The Hill1 analysis reveals that **TBT1** displays the lowest K_d value

of ~ *0.5±0.01* µM for Pu22 *c-MYC* G4 while it does not exhibit comparable binding affinities for *BCL-2* (*128* µM), *KRAS* (*97* µM), *c-KIT1* (n.d), *h-TELO* (n.d) G4s and *ds26* DNA.

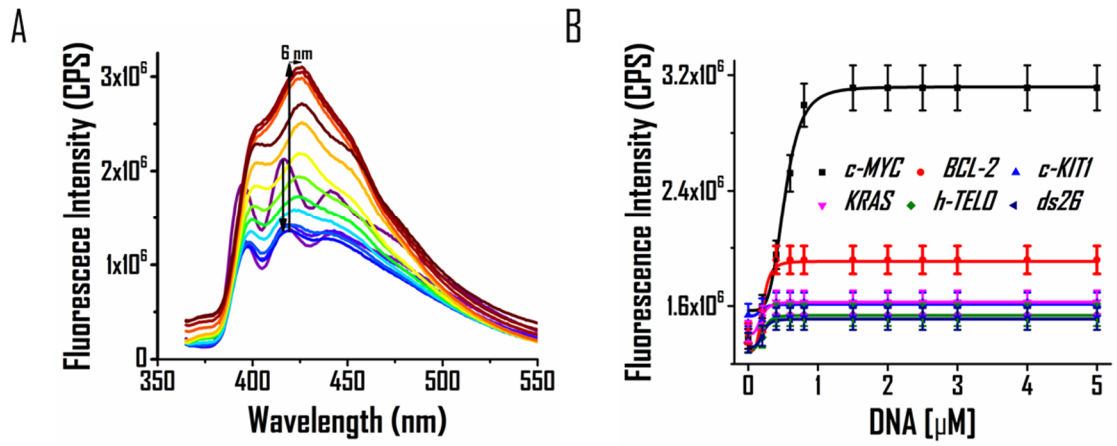

Figure 1B.2. (A) Determining the K_d value of **TBT1** with G4s and *ds26* DNA, & **(B)** Fluorometric titration of **TBT1** with *c-MYC22* in the presence of 60 mM K-Caco buffer (pH 7.4).

The fluorescence data indicates that the anthracene conjugated thiazole peptidomimetic **TBT1** possesses highest binding affinity for *Pu22 c-MYC* G4 over other investigated G4s and *ds26* DNA.

Growth inhibition of Cancer cells by TBT1

Cell viability assay

Cell Proliferation inhibitory activity of ligand **TBT1** was evaluated in cervical cancer (HeLa), breast cancer (MCF-7), and lung carcinoma (A549) and normal kidney epithelial

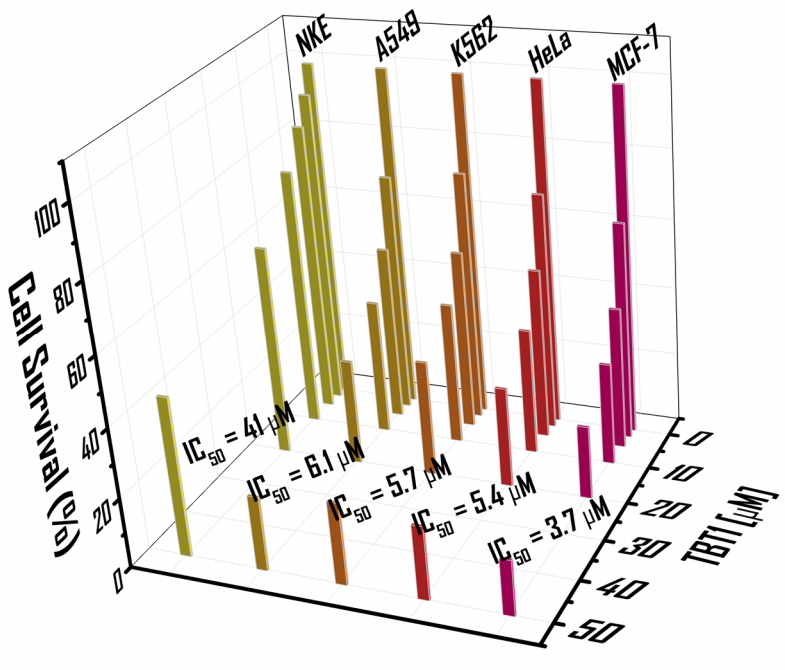

Figure 1B.3. Cell viability determination of **TBT1** in HeLa cells.

(NKE) cell lines through XTT assay. Cells treated with 0.1% DMSO was used as control. **TBT1** exhibited an IC_{50} value of 3.7 ± 0.6 µM for MCF-7 and 5.4 ± 0.4 µM for HeLa cells, 5.7 ± 2.8 µM and 6.1 ± 2.2 µM for K562 and A549 cells, respectively (Figure 1B.3). However, ligands **TBT1** showed negligible cytotoxicity towards normal kidney epithelial cells (IC_{50} > 40 µM). The data suggests that **TBT1** could inhibit the proliferation of cancer cells, and the surviving cell numbers indicate that **TBT1** possesses strong inhibitory activity on cancer cell growth.

Cellular localization of TBT1

Cellular uptake of **TBT1** was first examined by confocal microscopy in fixed MCF-7 cells (Figure 1B.4). The merged images of nuclear staining dye, NucRed

and compound indicate towards cellular compartmentalization of **TBT1**. Further, the image analysis illustrates that **TBT1** could efficiently invade the cell membrane and localizes in the nucleus of cancer (MCF-7) cells. The confocal imaging results point towards the comprehensive characteristics of **TBT1** in cancer cells.

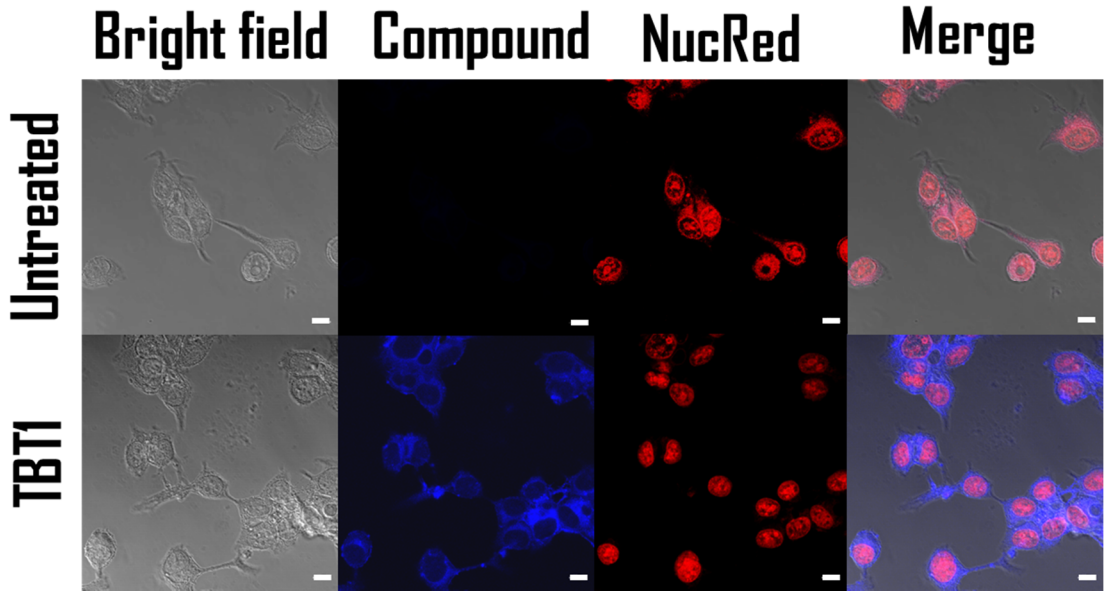

Figure 1B.4. Cellular localization of **TBT1** in HeLa cells.

***TBT1** down-regulates the c-MYC transcription and translation in cancer cells*

Quantitative real-time PCR was performed to evaluate the regulatory role of **TBT1** on the transcriptional activity of *c-MYC* proto-oncogene (Figure 1B.5A). The PCR analysis reveals that **TBT1** can reduce the *c-MYC* m-RNA level up to ~ 53% at 2 µM concentrations while exceptional decline of ~ 96% can be observed at 4 µM. The above data suggest that **TBT1** could induce the cell death via transcriptional down-regulation of *c-MYC* oncogenes in cancer cells. Further measurements of *c-*

MYC protein level by western blot assay illustrate that **TBT1** could reduce the *c-MYC* expression up to ~ 84% at the maximum dose of ~ 4 µM (Figure 1B.5B). This was in great agreement with the qRT-PCR data that **TBT1** plays a critical role as a *c-MYC* repressor, which might be due to the interaction with *c-MYC* promoter G4 in cancer cells.

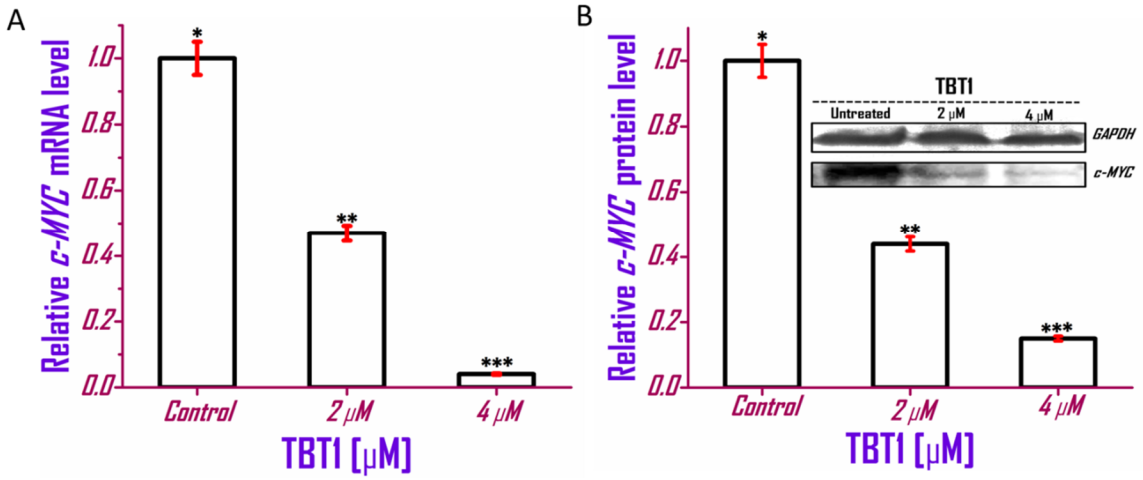

Figure 1B.5. (A) qRT-PCR analysis for transcriptional regulation of *c-MYC* after treatment with **TBT1** in MCF-7 cells for 24 h. Quantification was done in terms of fold change by double delta C_T method using 18s rRNA as housekeeping or reference gene. Fold change of ligand treated relative gene expression is normalized with control. (B) Western blot analysis for translational regulation of *c-MYC* after treatment with **TBT1** in MCF-7 cells for 24 h. Three biological replicates were employed for the quantifications. Error bars represent mean ±SD. *P<0.05, **P<0.05 and ***P<0.001 (Student's t test), versus control MCF-7 cells.

Conclusion

In summary, a cytotoxic thiazole incorporated peptidomimetic has been developed to preferentially stabilize the *c-MYC* G4 and hold back *c-MYC* transcription machinery in breast cancer cells. The biophysical analysis suggests that **TBT1** shows highest stabilization potential (ΔT_M = 18.3 $^{\circ}$C) and selective binding affinity (K_d ~ 0.5 µM) for *c-MYC* G4 DNA over other G4s and *ds26* DNA. In cell investigation elucidates that **TBT1** could display preferably more potent toxicity towards the breast cancer cell lines (IC_{50} ~ 3.7 µM) compared to cervical (IC_{50} ~ 5.4 µM), lung carcinoma (IC_{50} ~ 5.7 µM) and leukemia (IC_{50} ~ 6.1 µM) cells. It is of more importance that the peptidomimetic ligand **TBT1** does not show comparable toxicity (IC_{50} ~ 41 µM) in normal kidney epithelial cells indicating reduction of adverse effects unlike other chemotherapeutic small molecules. Intriguingly, fluorescence microscopy image depicts that **TBT1** could efficiently colocalize into nucleus with NucRed, suggesting cell membrane permeability and nucleus imaging property of **TBT1** in cancer cells. Quantitative m-RNA analysis and protein expression study illustrate that the ligand could inhibit the *c-MYC* protooncogene and protein expression up to ~ 95% and ~ 86% in MCF-7 cells, respectively. Further measurement of oncogene promoter activity via luciferase reporter assay points towards the **TBT1** mediated stabilization of *c-MYC* G4 following subsequent downregulation of *c-MYC* protooncogene in breast cancer

cells. The development of such G4 selective cytotoxic peptidomimetics could play a significant role as substitutes to non-specific DNA binding small molecules, often used for cancer theranostics. Altogether, the outcomes may provide insights into the design of new anticancer molecules with preferential affinity for the *c-MYC* G4-structures which in-turn may ease the off-target toxicity and increase bioavailability and also might help to escape the drug resistance property of cancer cells.

References

1. L. H. Hurley, *Nature Reviews Cancer* **2002**, *2*, 188-200.
2. R. M. Wadkins, *Current medicinal chemistry* **2000**, *7*, 1-15.
3. T. Tian, Y.-Q. Chen, S.-R. Wang, X. Zhou, *Chem* **2018**, *4*, 1314-1344.
4. J. Spiegel, S. Adhikari, S. Balasubramanian, *Trends in Chemistry* **2020**, *2*, 123-136.
5. D. Yang, in *G-Quadruplex Nucleic Acids*, Springer, **2019**, pp. 1-24.
6. B. Hoffman, D. A. Liebermann, *Oncogene* **1998**, *17*, 3351-3357.
7. K. B. Marcu, *Bioessays* **1987**, *6*, 28-32.
8. D. J. Patel, A. T. n. Phan, V. Kuryavyi, *Nucleic acids research* **2007**, *35*, 7429-7455.
9. S. Pelengaris, M. Khan, G. Evan, *Nature Reviews Cancer* **2002**, *2*, 764-776.
10. C. V. Dang, L. M. Resar, E. Emison, S. Kim, Q. Li, J. E. Prescott, D. Wonsey, K. Zeller, *Experimental cell research* **1999**, *253*, 63-77.
11. D. Yang, L. H. Hurley, *Nucleosides, Nucleotides, and Nucleic Acids* **2006**, *25*, 951-968.
12. T. A. Brooks, L. H. Hurley, *Nature Reviews Cancer* **2009**, *9*, 849-861.
13. S. Balaratnam, J. S. Schneekloth Jr, in *Annual Reports in Medicinal Chemistry, Vol. 54*, Elsevier, **2020**, pp. 361-407.
14. W. Wang, S. Hu, Y. Gu, Y. Yan, D. B. Stovall, D. Li, G. Sui, *Biochimica et Biophysica Acta (BBA)-Reviews on Cancer* **2020**, *1874*, 188410.
15. R. Rigo, M. Palumbo, C. Sissi, *Biochimica et Biophysica Acta (BBA)-General Subjects* **2017**, *1861*, 1399-1413.
16. A. Siddiqui-Jain, C. L. Grand, D. J. Bearss, L. H. Hurley, *Proceedings of the National Academy of Sciences* **2002**, *99*, 11593-11598.
17. F.-Y. Teng, Z.-Z. Jiang, M. Guo, X.-Z. Tan, F. Chen, X.-G. Xi, Y. Xu, *Cellular and Molecular Life Sciences* **2021**, *78*, 6557-6583.
18. V. González, L. H. Hurley, *Annual review of pharmacology and toxicology* **2010**, *50*, 111-129.

19. E. Largy, J.-L. Mergny, V. Gabelica, in *The Alkali Metal Ions: Their Role for Life*, Springer, **2016**, pp. 203-258.
20. J. H. Han, J. H. Kim, S. K. Kim, Y. J. Jang, *Journal of Biomolecular Structure and Dynamics* **2020**, *38*, 2575-2581.
21. J.-L. A. Saccabourdoncle, F. J. G. Mergny, A. B. D. C. Rosu, L. Lacroix, *Quadruplex Nucleic Acids* **2007**, 31.
22. M. Düchler, *Journal of drug targeting* **2012**, *20*, 389-400.
23. J. Xu, R. Jiang, H. He, C. Ma, Z. Tang, *TrAC Trends in Analytical Chemistry* **2021**, *139*, 116257.
24. E. Mendes, I. M. Aljnadi, B. Bahls, B. L. Victor, A. Paulo, *Pharmaceuticals* **2022**, *15*, 300.
25. S. Neidle, *Quadruplex Nucleic Acids As Targets For Medicinal Chemistry*, Academic Press, **2020**.
26. C. Nakanishi, H. Seimiya, *Biochemical and biophysical research communications* **2020**, *531*, 45-50.
27. X.-N. Wang, X.-X. Su, S.-Q. Cheng, Z.-Y. Sun, Z.-S. Huang, T.-M. Ou, *Expert Opinion on Therapeutic Patents* **2019**, *29*, 353-367.
28. A. Głuszyńska, B. Juskowiak, M. Kuta-Siejkowska, M. Hoffmann, S. Haider, *International journal of biological macromolecules* **2018**, *114*, 479-490.
29. I. Alessandrini, M. Recagni, N. Zaffaroni, M. Folini, *International journal of molecular sciences* **2021**, *22*, 5947.

Chapter 2

Stabilizing SARS-CoV-2 RNA G4s by small molecules

Immense scientific efforts have been made towards the development of potential antiviral therapeutics for SARS-CoV-2 (SCoV-2) since the 2020 outbreak.[1] Despite impressive vaccination trials to combat the disease worldwide; the recurrence of SCoV-2 is a serious concern due to its high mutation rate; even vaccination might not give a full protection to an individual.[2-4] Hence, there is an emergence of developing new strategies to combat this critical deadly disease. Several experimental and computational approaches have been published in literature to develop small molecule based SCoV-2 therapeutics.[5-7] Most of the studies are based on targeting the viral genome by well-known small molecules, which are previously FDA approved for other pathological conditions.[8] Therefore, this type of strategy has led to non-specific interaction of the molecules with biological macromolecules present in the human genome. However, a very few number of studies have been reported to target the RNA secondary structures of SCoV-2 genome.[9,10] The SCoV-2 RNA harbors G-rich four stranded secondary structures known as G-quadruplexes,[11,12] which could be a promising target to achieve the antiviral therapeutics against SCoV-2.[12,13] However, targeting the RNA G-quadruplex structures by small molecules has been a daunting task until today.

Analysis of SARS-CoV2 RNA G4 structures by CD spectroscopy

G4 structures exhibit circular dichroism (CD) owing to the presence of overall chirality. CD spectra of G4s are typically interpreted in an empirical manner.

When the polarity of all the strands is oriented in same direction, the G4 holds the parallel topology and displays a positive peak near 265 nm and a negative peak at 240 nm.[14] Antiparallel G4s with alternating strand polarity possess a different spectrum with a positive peak near 295 nm along with a negative peak 260 nm.[14,15] Mixed orientation is also possible when maxima near 295 and 265 nm are present, indicating the presence of both parallel and antiparallel folding in the solution, or a mixed-hybrid-type G4 structure of three parallel strands and one antiparallel strand.[14-16]

The CD spectra recorded in 100 mM Tris-KCl buffer depicts that all of the pre-annealed RNA G4 forming oligonucleotides *RG-1* (*5′- GGCUGGCAAUGGCGG- 3′*), *RG-2* (*5′- GGUAUGUGGAAAGGUUAUGG -3′*) and *RG-3* (*5′- GGCUUAUAGGUUUAAUGGUAUUGG -3′*) exhibited CD positive peaks at ~265 nm and negative peaks at ~240 nm. These data indicate that the *RG-1, RG-2* and *RG-3* form potential G4 structures and hold a parallel type conformation in the presence of K^+. However, Figure 2.1 also illustrates that among those RNA G4 structures, *RG-1* and *RG-2* hold most promising topology over the *RG-3* sequence. The mutated sequences of *RG-1* and *RG-2* do not exhibit putative quadruplex like CD waveforms indicating conserved quadruplex structures for wild type *RG-1* and *RG-2*.

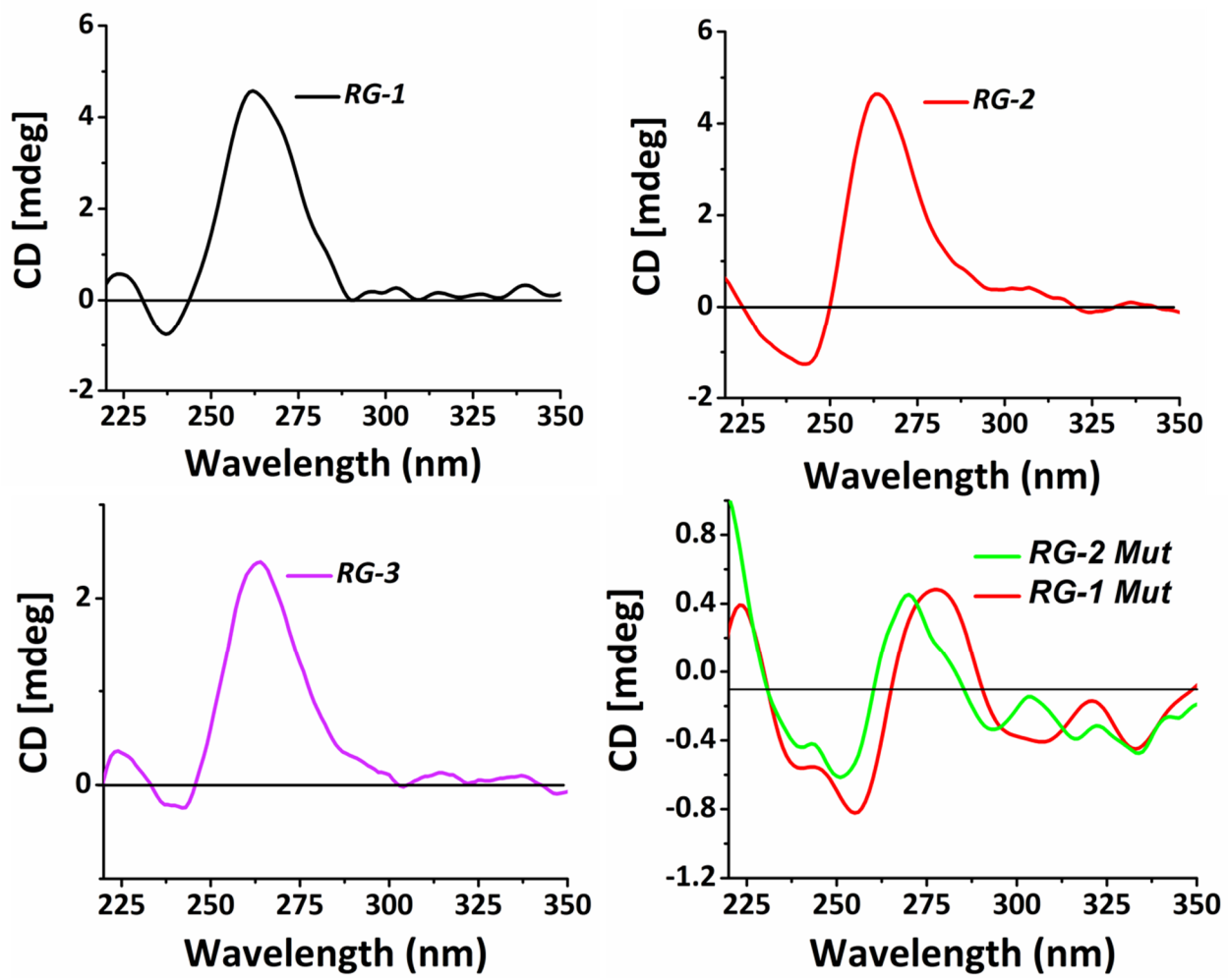

Figure 2.1. CD profiles of SARS-CoV-2 *RG-1*, *RG-2*, *RG-3*, *RG-1 (Mut)* and *RG-2 (Mut)* at the 5 µM concentrations in the presence of 100 mM Tris-KCl buffer (pH 7.4).

FRET based melting assay

The RNA G4 stabilizing feature of peptidomimetic ligands were primarily assessed by melting experiments on RNA G4 forming sequences (*RG-1*, *RG-2* and *RG-3*) and *dsDNA* or duplex DNA conjugated with 5'-FAM and 3'-TAMRA. The FRET based melting technique was used to inspect the ligand tempted stabilization for the RNA G4s and *dsDNA* by comparing the RNA or DNA melting temperature

(T_M) of control (without ligand) and ligand treated RNA or DNA (Figure 2.2). **RD1** did not possess significant alteration in the melting temperature (ΔT_M) of RNA G4s (*RG1* = 0 °C, *RG-2* = 4.8±0.2 °C, *RG-3* = 4.6±0.2 °C) and *dsDNA* (0 °C) at 2 µM or 10 eq. concentration of RNA or *dsDNA*. **RD2**, **RD3** and **RD4** also possess almost similar deviation in ΔT_M value for the RNA G4s (**RD2**: *RG-1* = 0 °C, *RG-2* = 4.6±0.2 °C, *RG-3* = 3.2±0.2 °C; **RD3**: *RG1* = 1.7±0 °C, *RG-2* = 4.9±0.2 °C, *RG-3* = 3.7±0.1 °C; **RD4**: *RG1* = 1.7±0 °C, *RG-2* = 4.9±0.2 °C, *RG-3* = 3.3±0.1 °C) and *dsDNA* (0 °C). However, **RD5** shows exceptional stabilization potential for *RG-2* (ΔT_M = 23.7±1.2 °C) over *RG-1* (ΔT_M = 9±0.5 °C) and *RG-3* (ΔT_M = 4±0.2 °C) quadruplexes.

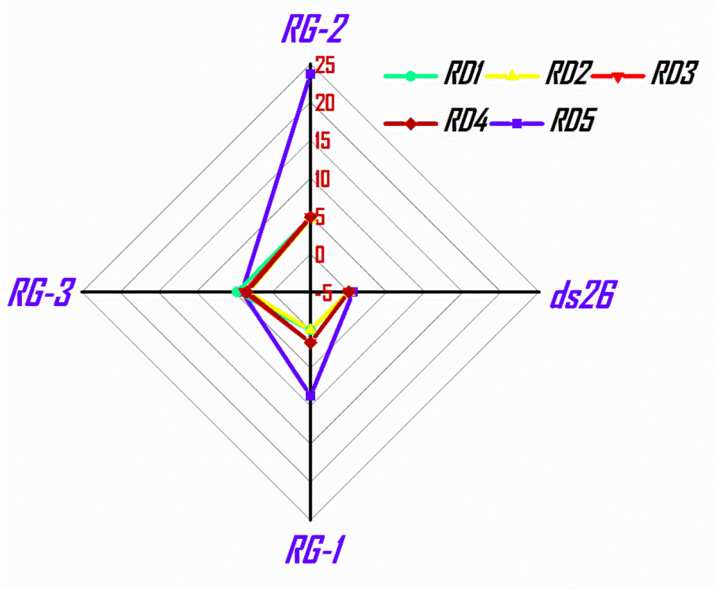

Figure 2.2. Determining the stabilization potential of **RD5** for *RG-1*, *RG-2*, *RG-3* SARS-CoV-2 quadruplex and *dsDNA* in the presence of 100 mM Tris-KCl buffer (pH 7.4).

More interestingly, **RD5** does not hold any stabilization property for duplex or *dsDNA*. Thus, the FRET based data indicate that the peptidomimetic **RD5** preferentially stabilizes the *RG-2* RNA over other investigated SARS-CoV-2 RNA G4s and *dsDNA*.

Fluorescence spectroscopy

The peptidomimetic ligand **RD5** was further evaluated for its binding properties upon interaction with the *RG-1*, *RG-2*, *RG-3* RNA and *ds26* DNA structures via fluorescence spectroscopic titration experiment. Fluorometric measurements show that **RD5** exhibit maxima at 434 nm upon excitation at 325 nm in 100 mM Tris-KCl buffer, pH 7.4 (Figure 2.3). Intriguingly, upon addition of *RG-2*, a new peak generated at 356 nm and the intensity of **RD5** was enhanced up to ~ 13 fold until saturation (K_d = 1±0.05 µM). Only mild or no alterations in fluorescence were obtained when **RD5** was titrated with *RG-1* (K_d = 4.2±0.2 µM), *RG-3* (K_d = 34±1.7 µM) and *dsDNA* (K_d = n.d). The above fluorescence data illustrate that the coumarin conjugated peptidomimetic ligand **RD5** preferentially binds to *RG-2* RNA G4 over other tested G4s and *ds26* DNA.

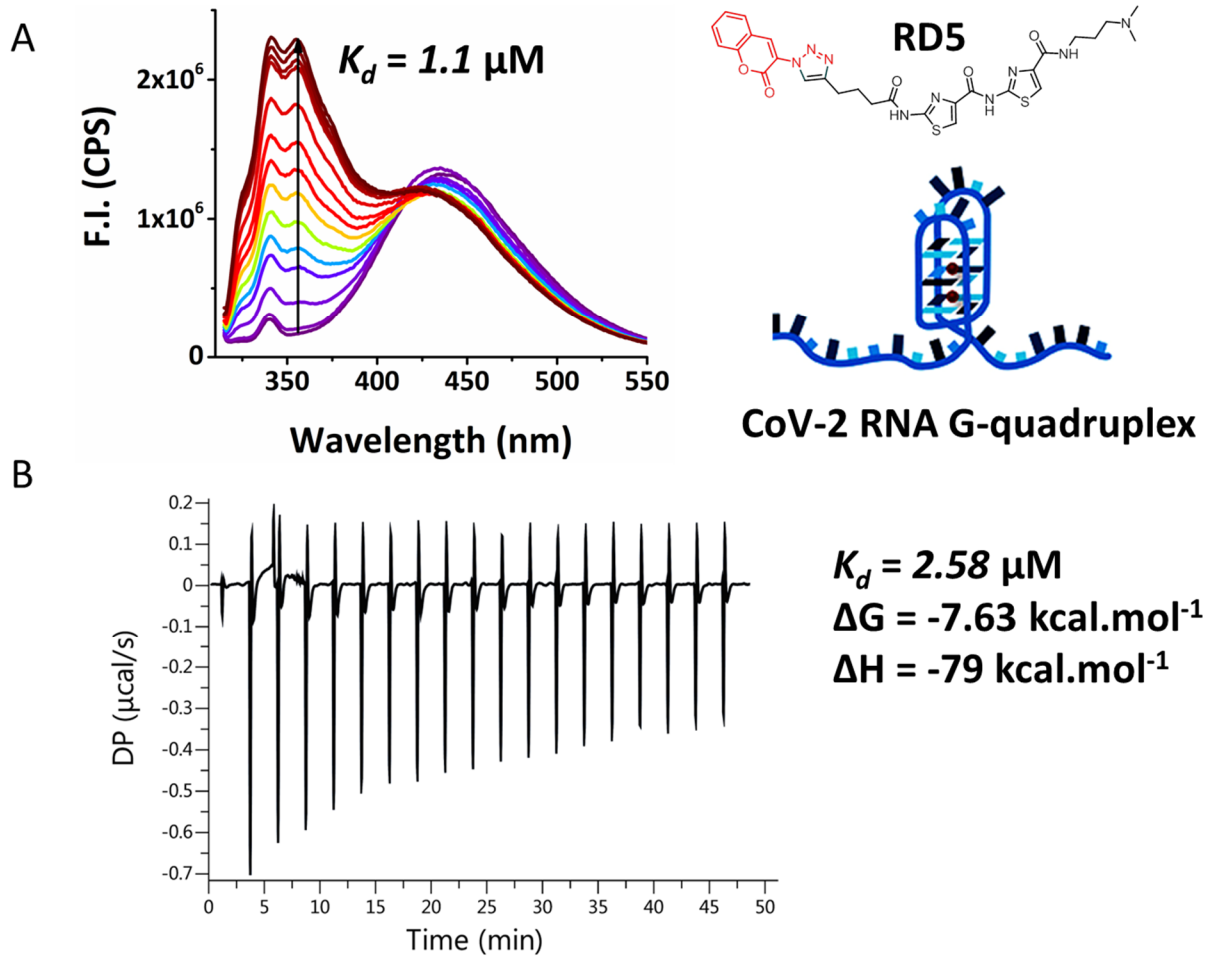

Figure 2.3. (A) Fluorometric titration of **RD5** with *RG-2* G4 in the presence of 100 mM Tris-KCl buffer. (B) Isothermal calorimetric titration experiment of **RD5** with *RG-2* in the presence of 100 mM Tris-KCl buffer (pH 7.4).

In comparison, **RD1 RD2 RD3** and **RD4** do not display binding affinity towards either RNA G4s or *ds26 DNA* as revealed from fluorescence titration. The above fluorescence data illustrate that the coumarin conjugated peptidomimetic ligand **RD5** preferentially binds to *RG-2* RNA G4 over other tested G4s and *ds26* DNA.

Isothermal calorimetric titration

Isothermal titration calorimetry (ITC) illuminates the thermodynamic parameters and binding insights of the peptidomimetic ligand with CoV-2 RNA G4s and *dsDNA*, as shown in Figure 2.3B. These ligands differed significantly in their binding affinity towards RNA G4s and *dsDNA*. The isothermal profiles were plotted using correct binding site model. Thermodynamic analysis revealed a sigmoidal binding isotherm of **RD5** for *RG-2* over *RG-1*, *RG-3* G4s and *dsDNA*. More importantly, the K_d value of **RD5** for *RG-2* determined using ITC (~ 1.8±0.1 μM) was in agreement with the K_d value obtained from fluorescence titration (Figure 2.3B). In comparison, **RD5** possessed moderate binding affinity for *RG-1* (K_d = 8±0.4 μM) while it possessed weak binding affinity for *RG-3* (K_d = 17±0.9 μM) compared to *RG-2*. However, it does not display affinity towards the *dsDNA*. Apart from that, **RD5** retains most favorable binding energy or Gibbs free energy of ΔG = ~ -8 kcal/mol for *RG-2*, which is indicative of spontaneous interaction of **RD5** with *RG-2* and it´s selective interaction towards the *RG-2* over other investigated CoV-2 G4s and *dsDNA*.

The isothermal profile correlates with the fluorescence titration and reveals that **RD5** preferentially interacts with the SARS-CoV-2 *RG-2* with 1:1 stoichiometry over *RG-1*, *RG-3* and *dsDNA*.

Conclusion

The novel coronavirus, COVID-19 has emerged as a global threat to mankind since 2020. In this chapter, a coumarin based peptidomimetic ligand has been developed that specifically interacts with SARS-CoV-2 RNA quadruplex over duplex DNA as revealed from biophysical assays. The FRET analysis elucidates that the molecule **RD5** possesses the highest stabilization potential for the *RG-2* G4s (ΔT_M = 23.7±1.2 °C) over other SARS-CoV G4 structures like *RG-1*, *RG-3* and duplex DNA. The fluorescence spectroscopic results illustrate that the ligand preferentially binds to the *RG-2* (K_d = 1±0.05 μM) with high affinity compared to *RG1*, *RG-3* and *dsDNA*. More intriguingly, ligand **RD5** interacts with the *RG-2* with potential binding energy (ΔG = ~ -8 kcal/mol) and 1:1 stoichiometry as indicated in calorimetric data. Overall, the study suggests that the peptidomimetic ligand **RD5** harbors the unique feature to be able to specifically interact with COVID-19 quadruplex *RG-2*. We predict that the ligand could inhibit the replication of SARS-CoV-2 via the stabilization of G-quadruplex which will be further studied in near future. This work will further inspire and propagate the design and synthesis of new peptidomimetic synthetic molecules to target the SARS-CoV-2 RNA secondary structures towards the development of antiviral therapeutics and biomolecular devices in pharmaceutical sectors.

References

1. D. Wu, T. Wu, Q. Liu, Z. Yang, *International journal of infectious diseases* **2020**, *94*, 44-48.
2. D. Mercatelli, F. M. Giorgi, *Frontiers in microbiology* **2020**, *11*, 1800.
3. J. A. Malik, S. Ahmed, A. Mir, M. Shinde, O. Bender, F. Alshammari, M. Ansari, S. Anwar, *Journal of infection and public health* **2022**.
4. W. Zhou, W. Wang, *Signal transduction and targeted therapy* **2021**, *6*, 1-6.
5. D. Tian, Y. Liu, C. Liang, L. Xin, X. Xie, D. Zhang, M. Wan, H. Li, X. Fu, H. Liu, *Biomedicine & Pharmacotherapy* **2021**, *137*, 111313.
6. E. N. Muratov, R. Amaro, C. H. Andrade, N. Brown, S. Ekins, D. Fourches, O. Isayev, D. Kozakov, J. L. Medina-Franco, K. M. Merz, *Chemical Society Reviews* **2021**.
7. E. Y. Lau, O. A. Negrete, W. D. Bennett, B. J. Bennion, M. Borucki, F. Bourguet, A. Epstein, M. Franco, B. Harmon, S. He, *Frontiers in Molecular Biosciences* **2021**, *8*, 678701.
8. S. Drożdżal, J. Rosik, K. Lechowicz, F. Machaj, K. Kotfis, S. Ghavami, M. J. Łos, *Drug resistance updates* **2020**, *53*, 100719.
9. S. Hegde, Z. Tang, J. Zhao, J. Wang, *Frontiers in chemistry* **2021**, *9*, 802766.
10. C. Zhao, G. Qin, J. Niu, Z. Wang, C. Wang, J. Ren, X. Qu, *Angewandte Chemie* **2021**, *133*, 436-442.
11. D. Ji, M. Juhas, C. M. Tsang, C. K. Kwok, Y. Li, Y. Zhang, *Briefings in bioinformatics* **2021**, *22*, 1150-1160.
12. E. Belmonte-Reche, I. Serrano-Chacón, C. Gonzalez, J. Gallo, M. Bañobre-López, *PloS one* **2021**, *16*, e0250654.
13. E. Ruggiero, I. Zanin, M. Terreri, S. N. Richter, *International Journal of Molecular Sciences* **2021**, *22*, 10984.
14. A. Randazzo, G. P. Spada, M. W. d. Silva, *Quadruplex nucleic acids* **2012**, 67-86.
15. S. Masiero, R. Trotta, S. Pieraccini, S. De Tito, R. Perone, A. Randazzo, G. P. Spada, *Organic & biomolecular chemistry* **2010**, *8*, 2683-2692.
16. R. del Villar-Guerra, R. D. Gray, J. B. Chaires, *Current protocols in nucleic acid chemistry* **2017**, *68*, 17.18. 11-17.18. 16.

Chapter 3

Bio-inspired Artificial Ion Channels

Chapter 3A

Synthetic Ion Channel Fabrication with G-quadruplex Ligand

Natural ion channel-forming peptides play pivotal role in cellular homeostasis by transporting ions across the lipid bilayer membrane.[1,2] Selectivity filter inside the channels commands the cation or anion to pass through the channel.[2,3] It is noteworthy to assert that biological channels possess remarkable properties to be capitalized in the development of chemotherapeutics and diagnostics.[2-4] The complex structures of channel proteins and biological mechanism for ion transport make natural ion channels one of the critical species for practical use.[4-6] Nevertheless, scientists have reported elegant approaches to build synthetic ion channels by imitating definite characteristics of natural ion channels. In last two decades, effort has been made to develop robust artificial ion channels by mimicking the activity of natural peptides or proteins. This peptide based synthetic ion channels have found applications in antibacterial and anticancer therapeutics, biosensing, nanodevices, drug delivery tools etc.[7-13] However, limited number of studies have reported that small molecules alone can act as chemotherapeutics agenst and synthetic transporter of ions in biological model systems.[14-19] Apart from that, the mechanism behind the chemotherapeutic role of these artificial transporters typically remains unexplored. Henceforth, there is an emerging need to establish mechanistic insights of cancer therapy by these peptidomimetic ion transporters which might further help to design novel blueprint for potential chemotherapeutic agent.[20-34] Targeting DNA secondary structures by peptidomimetic small molecules became one of the important chemotherapeutic strategies in last few decades.[35-38]

The non B-DNA four stranded DNA secondary structures e.g., G-quadruplex (G4) play key role in cellular growth by regulating the replication and transcription machinery inside the cells.[39-41] G4s are often prevalent in the promoter G-rich region of various proto-oncogenes (e.g., *c-MYC*, *BCL-2*, *KRAS*, *c-KIT*) and telomere (*h-TELO*) of cancer cells.[40-42] *c-MYC* is one of the most abundant proto-oncogenes among diverse cancers types (cervical cancer, breast cancer, lung carcinoma etc.) and responsible for cell proliferation, apoptosis and drug resistance.[41-46] The overexpression of this specific protooncogene leads to tumorigenesis which makes the *c-MYC* a potential biological target for chemotherapeutics. The far upstream element (FUSE) and the nuclease hypersensitive element (NHE III_1), two upstream elements of the P1 and P2 promoter of *c-MYC* possess the propensity to undergo conformational changes into non-B-DNA structures. The NHE (nuclease hypersensitive element) III_1 of *c-MYC* promoter, regulates the transcriptional activity (~90%), harbors G4 forming sequences which act like transcriptional repressors. The G4 forming sequence in the promoter NHE III_1 region preserves the highest tendency to fold into G4 structures in presence of monovalent cations like Na^+ and K^+.[42-49] Stabilization of these G4 structures present in *c-MYC* oncogene promoter by small molecules evolved as a potential strategy towards drug development for cancer therapeutics.[49-56] We have previously reported that peptidomimetic ligand **TH3** can act as potential *c-MYC* G4 binder and represses transcription in cancer cells to induce cell death.[37] Herein, we have designed and developed an artificial ion channel with a thiazole based novel peptidomimetic which can

effectively transport Na^+ and K^+ ions across model lipid bilayer membrane. In addition, the biophysical assays revealed that the small molecule **TBP2** can selectively bind to *c-MYC* G4 with a 1:1 stoichiometry. In vitro cellular results indicated that **TBP2** inhibits the growth of cancer cells through *MYC* mediated transcriptional downregulation.

A series of biophysical assays e.g., HPTS assay using Large Unilamellar Vesicles (LUVs), patch clamp studies for measurement of ion conductance via Giant Unilamellar Vesicles (GUVS), CF release assay to determine membrane integrity were carried out to validate the formation of ion channel by the peptidomimetics. Besides that, Transmission Electron Microscopy (TEM) imaging was performed to investigate the formation of nanostructures shaped by these thiazolyl peptidomimetics. To further explore the impact of these ionophores in biological system and study the mechanistic insights, different biophysical (e.g., melting experiments by FRET, fluorescence titration, NMR titration) and biological assays (e.g., confocal imaging, cell viability assay, qRT-PCR, luciferase reporter assay) were implemented.

Results and Discussion

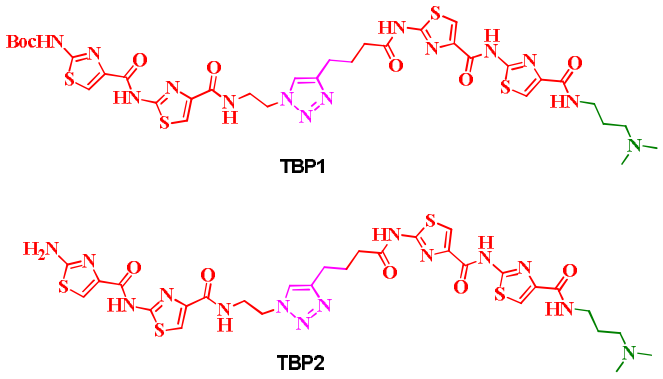

Figure 3A.1. Design of thiazolyl peptidomimetics **TBP1** and **TBP2**

TBP2 transports Na^+ and K^+ ions across artificial lipid bilayer

HPTS assay

The ion-transport activities of **TBP1** and **TBP2** were examined by fluorescence based HPTS (8-hydroxypyrene-1, 3, 6-trisulfonic acid trisodium salt) assay[6]: HPTS was entrapped in EYPC (Egg Yolk L-α-Phosphatidylcholine) liposomes (large unilamellar vesicles, LUVs of ~ 70 nm (average diameter) as measured by dynamic light scattering method) containing HEPES NaCl or HEPES KCl (10 mM HEPES, 100 mM NaCl or KCl, pH 6.4) buffer. The liposomes were suspended in 10 mM HEPES buffer (pH 6.4) containing 100 mM of MCl_2 (M^{n+}= Na^+, K^+). Next, after introduction of **TBP1** and **TBP2** (dissolved in DMSO) in the bilayer membrane, an external pH gradient was generated by NaOH addition. Thereafter, the pH dependent change in fluorescence intensity of HPTS was observed against the function of time. **TBP1** did not show significant change in HPTS fluorescence up to 20 μM while the **TBP2** displayed high transport activity for K^+

(~70%) and Na^+ (~65%) in presence of HEPES NaCl or HEPES KCl internal buffer (pH7.4) (Figure 3A.2). Hill equation was used to determine the EC_{50} values

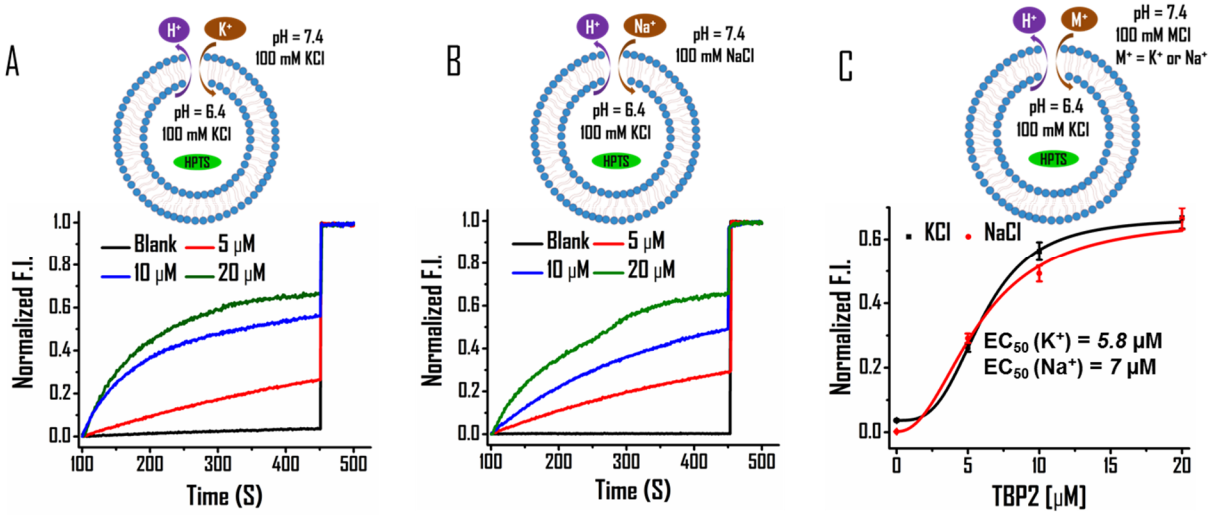

Figure 3A.2. HPTS assay & determination of EC_{50} values for measuring the ion transport activity of **TBP2** in presence of Na^+ and K^+. Buffer composition: Internal – 10 mM HEPES 100 mM KCl (pH 6.4); External –10 mM HEPES 100 mM KCl (pH 7.4). **(C)** EC_{50} value determination of **TBP2** in presence of external buffer – 10 mM HEPES 100 mM NaCl or KCl (pH 7.4), internal buffer – 10 mM HEPES 100 mM KCl (pH 6.4).

(concentration of molecules to achieve 50% ion transport activity) of these thiazolyl peptidomimetics. **TBP2** displayed EC_{50} value of 5.8 μM and 7 μM for K^+ and Na^+, respectively in the presence of HEPES KCl or NaCl (Internal:10 mM HEPES 100 mM KCl, pH 6.4, External: 10 mM HEPES 100 mM NaCl, pH 7.4). **TBP2** exhibits comparatively greater transport efficiency for K^+ and Na^+ in presence of alternate internal buffers which might be due to exchange of both the K^+ and Na^+ ions. The Hill coefficient of **TBP2** for K^+ (n_{K^+} = 1.64) indicates more than one molecule forms the supramolecular ion channel to transport K^+. However, one molecule of **TBP2** creates channel to transport Na^+ (n_{Na^+} = 0.92) via vesicular lipid membrane as determined by Hill1 equation. The

above HPTS data indicate that **TBP2** is capable of acting as an ionophore to form synthetic ion channel and shows greater efficiency to transport K^+ and Na^+ compared to **TBP1**.

***TBP2** preserves membrane integrity*

CF release assay

To determine the effects of **TBP1** and **TBP2** on membrane integrity, a self-quenched carboxyfluorescein dye (CF) (<1 nm in size) was encapsulated inside the LUVs (Fig. 3A.3). CF leakage assay principles state that, highly fluorescent monomeric CF molecules form nearly non-fluorescent dimers at 40-50 mM. Similarly, the membrane impermeable CF dye (40 mM) can efflux from the vesicles as a result of a pore (>1 nm) formation or disruption of the LUVs, which in order will cause increase in fluorescence intensity. The CF release (%) can be quantified by observing the fluorescence intensity of released CF after addition of compounds compared to a 100% release by destroying the liposomes using 1X cell lysis buffer. The CF discharge percentage after addition of **TBP1** and **TBP2** was calculated to be 52% and 2.7% after 8 min, respectively into the extravesicular solution of HEPES-KCl (10 mM HEPES, 100 mM KCl, pH 7.4). Less percentage of CF release in the presence of **TBP2** indicate conserved membrane integrity of LUVs while the higher CF discharge illustrates that **TBP1** could disrupt the membrane structure or may form larger opening in vesicles. This CF dye release experiment substantiates that the observed ion transport behaviour are due to the channel forming properties of **TBP2**.

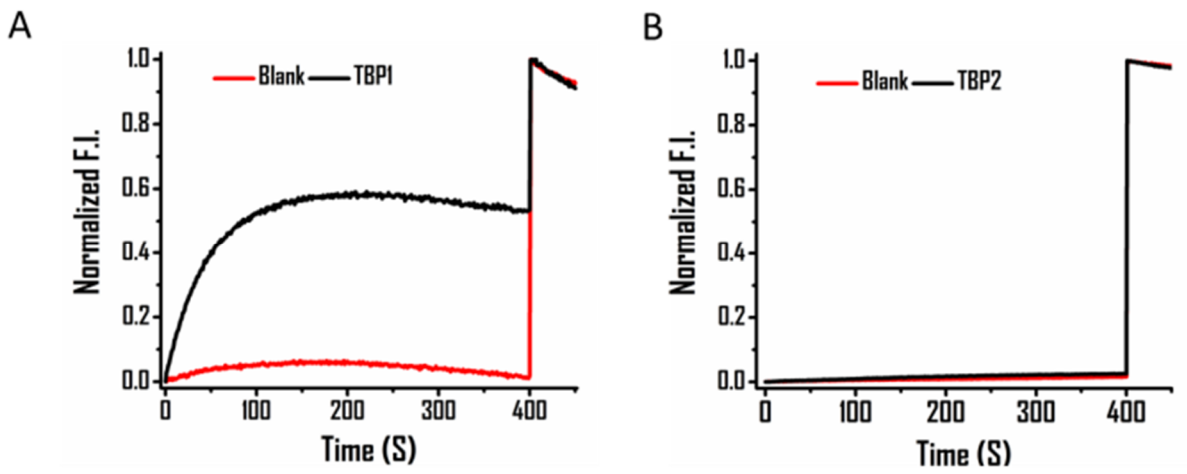

Figure 3A.3. CF release assay. Determination of CF release percentage in presence of **TBP1** and **TBP2** (External: 10 mM HEPES 100 mM NaCl, pH 7.4, Internal : 10 mM HEPES 100 mM NaCl, pH 7.4) after 8 minutes.

Ionic conductance measurement by patch clamp studies

The planar lipid bilayer experiments by nanion patch clamp technique provide further insight into real-time channel formation behaviour of thiazolyl peptidomimetics **TBP2**. Cis and trans compartments containing 1 M NaCl or 1 M KCl solution were separated by a planar lipid bilayer membrane composed of egg yolk L-α-Phosphatidylcholine (EYPC) lipid. Currents were measured as a function of time against different positive and negative applied potentials. The addition of **TBP2** to the planar bilayer resulted in distinctive channel openings and closing at +80 mV and -80 mV which in line confirms the formation of channel across planar lipid bilayer membrane (Figure 3A.4).The transport activity of both Na^+ and K^+ immediately starts after the addition of **TBP2**. The I-V plot of **TBP2** shows an ohmic-linear relationship between current vs. voltage (Figure 3A.3H). In presence of 1 M NaCl at both *cis* and *trans* side, **TBP2** displayed multiple channel opening to transport Na^+ at -80 mV. It also exhibited multiple square-top

behaviour at the holding potential of +80 mV. The average conductance for transporting Na^+ was measured to be ~0.56 nS which indicate high Na^+ conductivity via **TBP2** induced channel across the lipid bilayer. Moreover, **TBP2** generates stronger transport activity for K^+ with an average conductance of ~0.68 nS in presence of 1 M KCl. The above results indicate that **TBP2** can pass both the Na^+ and K^+ via model lipid bilayer system in a systematic manner. Figure 3A.4 suggests that **TBP2** could hold the channel like behaviour for Na^+ over a longer duration compared to K^+ while it is capable of transporting K^+ with higher conductance intensity in a shorter period of time compared to Na^+. Overall, the patch clamp studies suggest that **TBP2** could efficiently transport Na^+ and K^+ with high ionic conductance via planar lipid bilayer membrane.

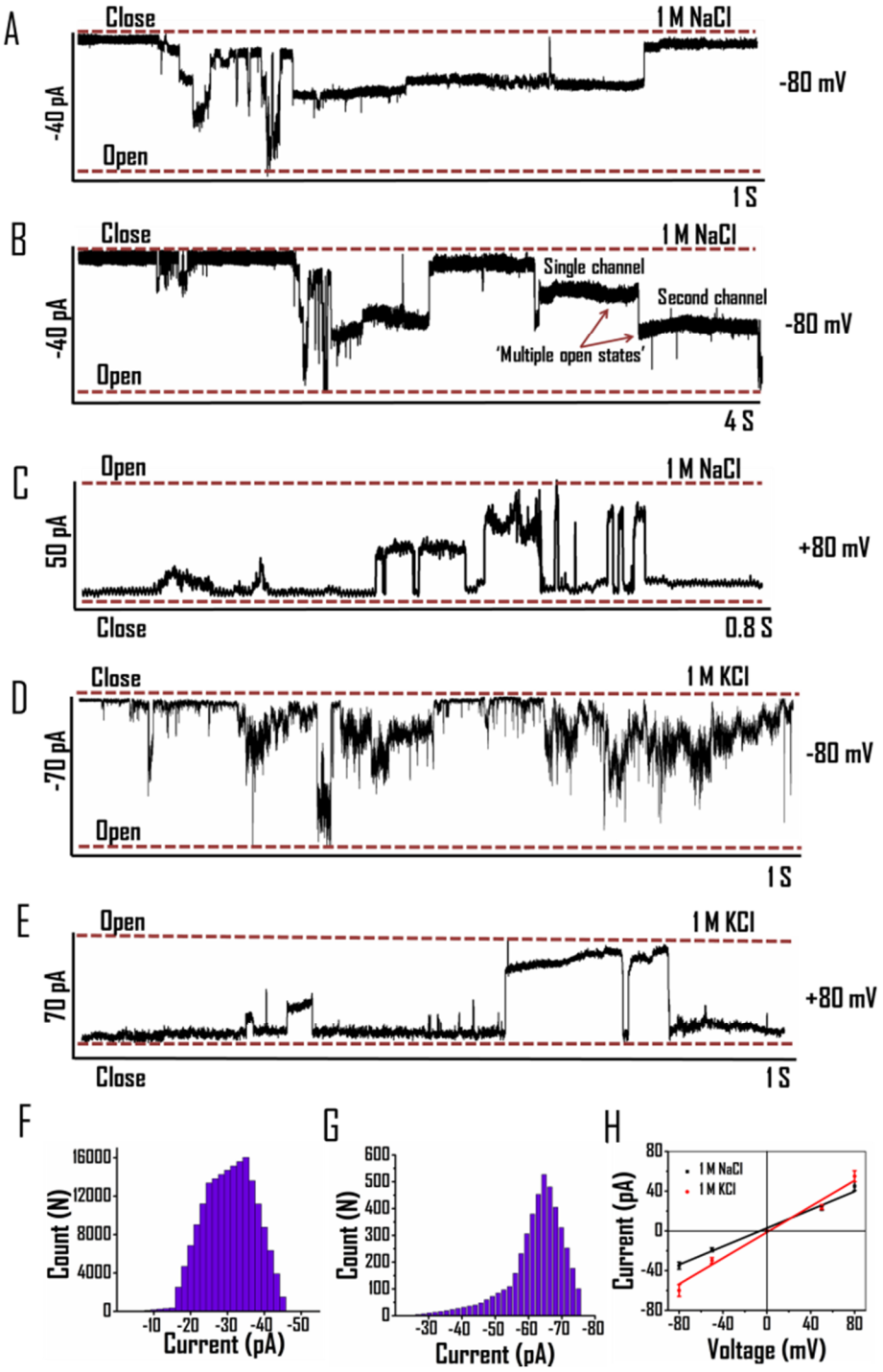

Figure 3A.4. Current measurement of **TBP2** in the presence of 1 M NaCl at (A, B) -80 mV, (C) +80 mV or 1 M KCl at (D) -80 mV and (E) +80 mV, respectively. (F) Bar diagram for frequency vs current of **TBP2** in the presence of 1 M NaCl (G) or 1 M KCl (at -80 mV). (H) I-V curve plot of **TBP2** in the presence of 1 M NaCl or 1 M KCl.

***TBP2** binds to vesicular membrane*

Confocal microscopy was performed by the formation of GUVs (stained with nile red) to assess the membrane embedding feature of **TBP2**. Microscopic imaging results indicated that **TBP2** can adsorb and colocalize with the membrane staining dye nile red into GUV membrane (Figure 3A.5) while no changes in fluorescence of control or untreated GUVs were detected. Thus, confocal microscopy demonstrated that **TBP2** can incorporate into the lipid membrane of unilamellar vesicles.

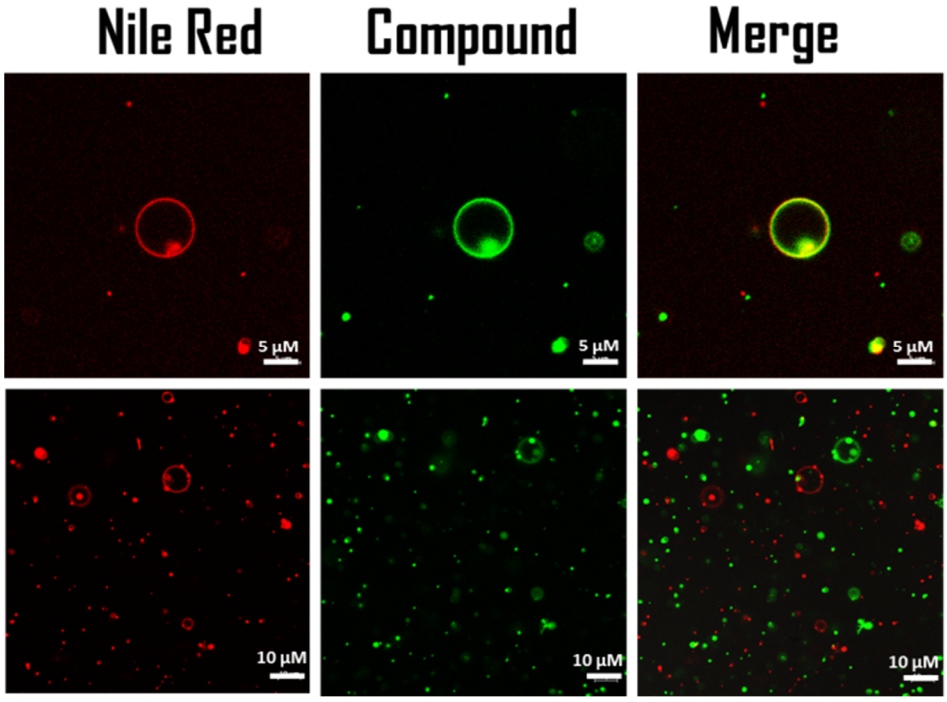

Figure 3A.5. Membrane colocalization of **TBP2** in GUVs by confocal microscopy

***TBP2** forms a self-assembled nanostructure*

Transmission Electron Microscopy imaging

The thiazolyl peptidomimetic **TBP2** was subjected to undergo transmission electron microscopy to assess the possibility of nanostructures formation. **TBP2** formed self-

assembled fibrous structures in presence of both NaCl and KCl buffer. Interestingly, supramolecular self-assembly of these nanostructures also resulted in the formation of nanovesicle like structures (Figure 3A.6). We assume that the both hydrophobic and hydrophilic part of the compound plays important role in the formation of vesicular structures.

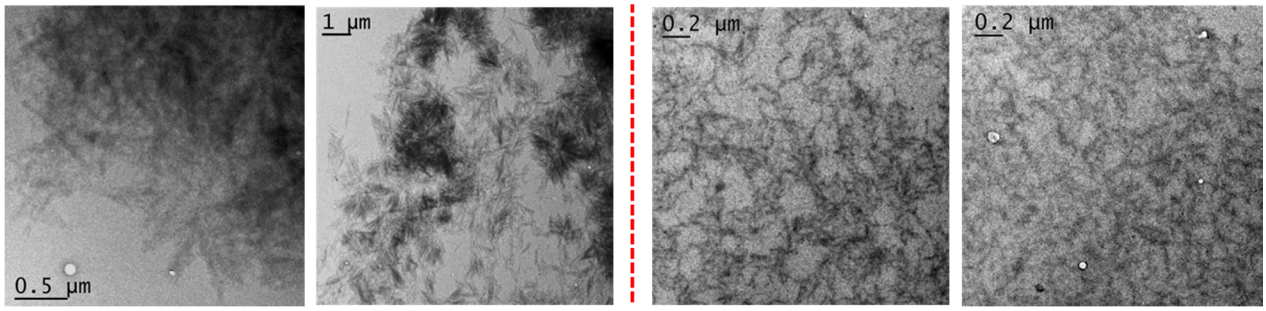

Figure 3A.6. TEM images of **TBP2** in both NaCl and KCl buffer (pH 7.4).

TBP2 *selectively binds to c-MYC G4 over ds26 DNA*

FRET based melting assay

The G4 stabilizing feature of **TBP1** and **TBP2** was primarily assessed by melting experiments on a series of G4 forming sequences (*c-MYC*22, *c-KIT1*, *c-KIT2*, *BCL-2*, *h-TELO*) and *ds26 DNA* or duplex DNA conjugated with 5'-FAM and 3'-TAMRA. The FRET based melting technique was used to evaluate the ligand tempted stabilization for the G4s and *ds26 DNA* by comparing the DNA melting temperature (T_M) of control (without ligand) and ligand treated DNA. **TBP1** (2 µM or 10 eq. concentration of DNA) did not show significant deviations in melting temperature (T_M) or ΔT_M values (*c-MYC*22 = 3.5±0.2 °C, *BCL-2* = 1±0 °C, *c-KIT1* = 0 °C, *c-KIT2* = 0.5±0 °C, *h-TELO* = 6±0.3 °C, *ds26 DNA* = 0 °C) for all the examined G4s and *ds26 DNA* (Figure 3A.7A,7B).

Intriguingly, **TBP2** displayed substantial ΔT_M values of 17±0.9 °C for *c-MYC*22 G4 DNA at 2 μM or 10 equivalent concentration of DNA. However, mild or no alterations in ΔT_M values (*BCL-2* = 3.8±0.19 °C, *c-KIT1* = 1.3±0.07 °C, *c-KIT2* = 4.1±0.2 °C, *h-TELO* = 4.2±0.2 °C, *ds26 DNA* = 0 °C) were detected for the other G4s and *ds26 DNA*. The above FRET based data demonstrate that **TBP2** exhibits highest stabilization potential (ΔT_M) for *c-MYC*22 G4 over other G4s and *ds26* DNA. Both **TBP1** and **TBP2** did not show any stabilization property for *ds26* or duplex DNA.

Fluorescence titration

Fluorometric measurements reveal that **TBP1** and **TBP2** exhibit maxima at 417 nm upon excitation at 325 nm in potassium cacodylate buffer (pH 7.4). Fluorescence emission intensity of **TBP2** was enhanced up to ~ 8 fold upon gradual addition of pre-annealed *c-MYC*22 G4 DNA (Figure 3A.7C,7D). Only mild or no alterations in fluorescence were obtained when **TBP1** was titrated with *c-MYC*22 G4. However, no noticeable changes in fluorescence intensity of **TBP2** were seen after titration with other DNA quadruplexes like *c-KIT1*, *c-KIT2*, *BCL-2*, *h-TELO* and *ds26 DNA*. The binding affinities of **TBP2** towards G4s and *ds26 DNA* were calculated based on the changes in fluorescence intensity of **TBP2**. As determined by Hill1 equation, **TBP2** exhibits a dissociation constant (K_d) value of *~1.6* μM for the *c-MYC*22 G4.

However, the K_d value of **TBP2** for *c-KIT1* (*9.5* μM), *h-TELO* (*8.2* μM) and *ds26 DNA* (*8.2* μM) were significantly higher as compared to *c-MYC*22 G4. In comparison, **TBP1** does not display binding affinity towards either G4s or *ds26 DNA* as revealed from

fluorescence titration. The fluorescence studies indicate that **TBP2** preferentially binds to *c-MYC* G4 over other experimented G4s and *ds26* DNA.

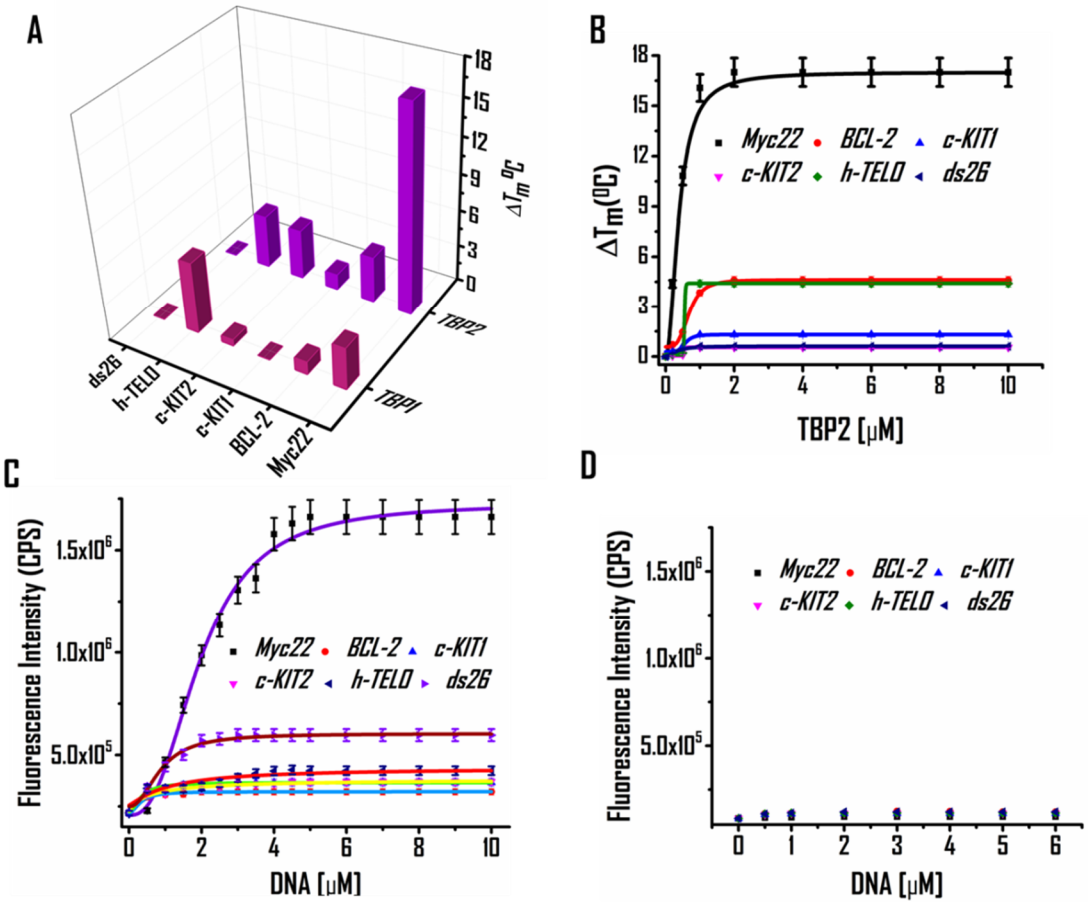

Figure 3A.7. (A) FRET based melting experiments to determine stabilization potenetial (ΔT_M) of **TBP1** and **TBP2** for G4s and *ds26* DNA and (B) FRET titration of **TBP2** with G4s and *ds26* DNA **TBP2** in 60 mM potassium cacodylate buffer (pH 7.4). Fluorescence titration of **TBP1** and **TBP2** in 60 mM potassium cacodylate buffer (pH 7.4).

***TBP2** inhibits the growth of cancer cells*

Biophysical properties of **TBP2** further instigate us to evaluate the biological activity of the same ligand in cancer cells. In-cellulo properties of **TBP2** were assessed by cell growth inhibition assay, quantifying the m-RNA level of *c-MYC* proto-oncogene and dual luciferase reporter assay.

XTT based cell viability assay

The antiproliferative activity of **TBP2** was examined in cancer cells (HeLa, K562, A549) and normal kidney epithelial (NKE) cells via XTT based cell viability assay (Figure 3A.8). **TBP2** exerted the IC_{50} values of 8.2 µM in cervical carcinoma (HeLa) cells while the same ligand showed IC_{50} values of ~10 µM and ~16 µM in leukemia (K562) and lung carcinoma (A549) cells, respectively. Intriguingly, **TBP2** did not display any IC_{50} value for normal kidney epithelial cells. The above results illustrate that **TBP2** can effectively inhibit the growth of cancer cells at considerable IC_{50} values. These preliminary data indicate that the ion transporter and *c-MYC* G4 binding peptidomimetic, **TBP2** can act as a new class of potential anticancer agent.

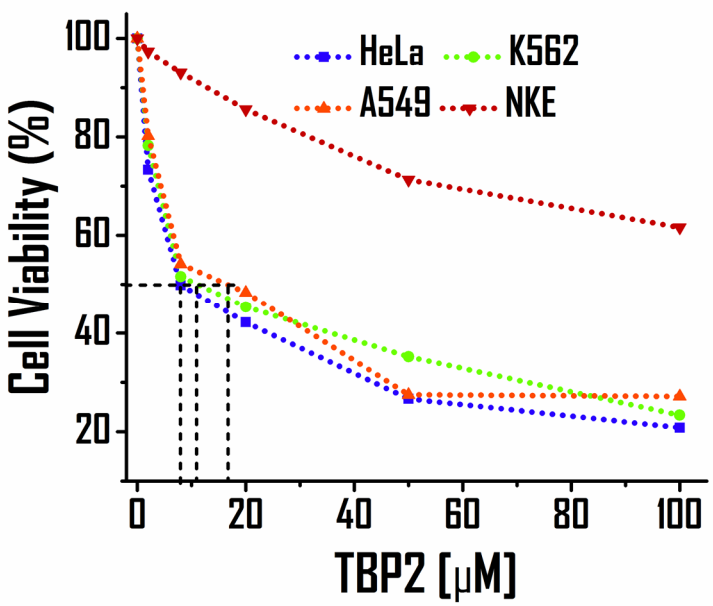

Figure 3A.8. Cell viability assay for **TBP2** in different cancer (HeLa, K562, A549) and normal kidney epithelial (NKE) cell lines.

***TBP2** localizes in cell membrane and nucleus*

In the next step, it was necessary to evaluate the cellular localization of **TBP2** in cancer cells by confocal imaging (Figure 3A.9). The imaging results show that **TBP2** can localize at both the cell membrane and nucleus of cancer cells. The little higher IC_{50} value might be the result of membrane and nuclear accumulation of **TBP2** in cancer cells. However, it is notable to state that **TBP2** can efficiently co-localizes with nucleus staining dye NucRed.

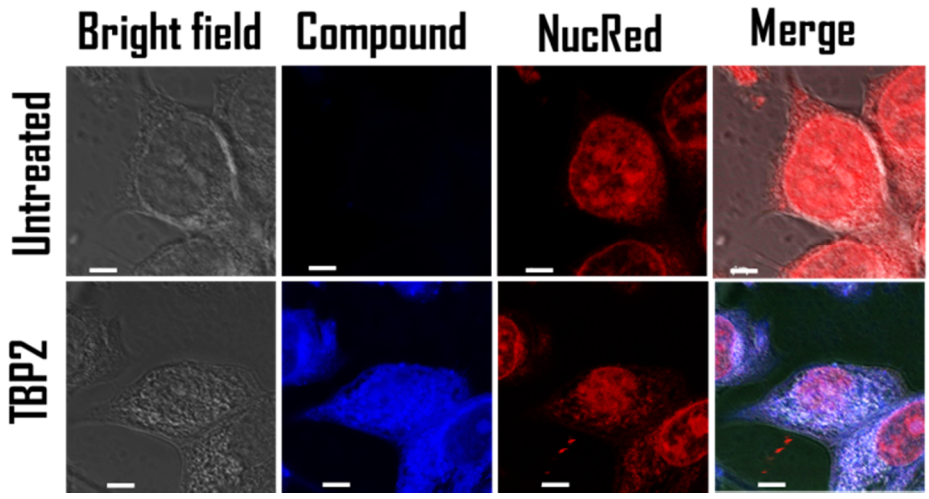

Figure 3A.9. Confocal images of HeLa cell (fixed) stained with **TBP2** (blue) and NucRed (red). Co-localization experiment of **TBP2** with NucRed in cancer cells. Scale bar represents 5 µm.

***TBP2** represses c-MYC transcription in cancer cells*

Gene expression analysis by Quantitative real-time PCR

TBP2 mediated oncogene regulation of *c-MYC* proto-oncogene was assessed in HeLa cells by quantifying relative mRNA steady-state levels via quantitative real-time PCR. The results elucidate that **TBP2** downregulates *c-MYC* expression at m-RNA level in cervical carcinoma cells. The *c-MYC* mRNA level was decreased significantly by 44% and 88% after treatment with **TBP2** at two different doses of 4 µM and 8 µM, respectively (Figure 3A.10A, 10B). As shown in Figure 3A.10B, a sharp decline in *c-MYC* expression level was observed in **TBP2** exposed cells at the lowest (4 µM) and highest (8 µM) concentration, compared to control cells. The above data exaggerate that **TBP2** plays pivotal role in the downregulation of *c-MYC* proto-oncogene expression to induce cell death in cancer cells.

Dual luciferase reporter assay

To examine whether the impact of **TBP2** on *c-MYC* oncogene expression was ensuing to their binding with *c-MYC* promoter, the luciferase expression was measured in HeLa cells using *c-MYC* wild type promoter and pRL-TK constructs (Figure 3A.10C). G4 forming sequences are not present in the pRL-TK construct (renila expressing plasmid) which makes the pRL-TK independent of G4 mediated regulation. The normalization of *c-MYC* promoter luciferase expression was achieved with pRL-TK expression. After 48 hours of treatment with **TBP2**, the *c-MYC* luciferase expression was exclusively reduced in a dose dependent mode for *c-MYC* wild type promoter construct. **TBP2** decreased the luciferase activity of *c-MYC* ~33% and ~24% at the two doses of 4 µM and 8 µM, respectively for *c-MYC* wild type promoter while there were negligible changes in luciferase expression of *c-MYC* mutants. These results indicate that **TBP2** could inhibit the *c-MYC* oncogene expression via potential stabilization of the *c-MYC* promoter G-quadruplex in cancer cells.

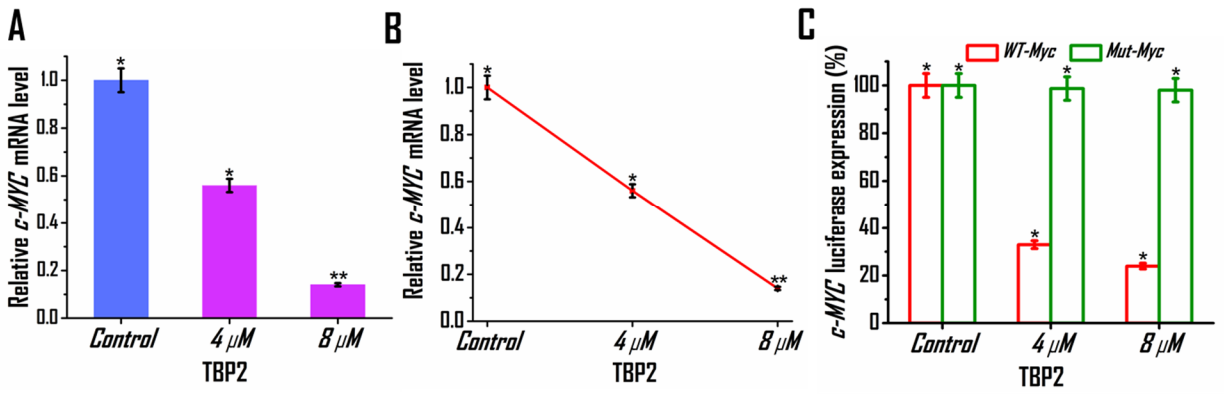

Figure 3A.10. qRT-PCR analysis (A, B) for transcriptional regulation of *c-MYC* after treatment with **TBP2** in HeLa cells for 24 h. Quantification was done in terms of fold change by double delta C_T method using 18s rRNA as housekeeping or reference gene. Fold change of ligand treated relative gene expression is normalized with control. Three biological replicates were employed for the quantifications. Error bars represent mean ±SD. *P<0.05 and **P<0.001 (Student's t test), versus control HeLa cells. (C) Relative luciferase expression of *c-MYC* promoter normalized with the Renilla plasmid pRL-TK after treatment with **TBP2** at two different doses for 48 h. Percentage change of ligand treated relative luciferase expression is normalized with control. Error bars stand for mean ±SD. *P<0.05 (Student's t test), versus untreated HeLa cells.

Conclusion

A very small number of molecules have been reported as synthetic ion transporters having chemotherapeutic properties with mechanistic insights till date. To the best of our knowledge, for the first time we present that an artificial ion channel can be constructed using a G-quadruplex binding thiazolyl peptidomimetic **TBP2** containing a triazole core. **TBP2** can transport metal ions in model lipid bilayer

membrane system and preferentially target G-quadruplex structure to mitigate *c-MYC* oncogene expression in cancer cells to induce cell death. HPTS assays revealed that **TBP2** serves as an efficient artificial ion transporter of Na^+ and K^+ via vesicular membrane. CF release assay and microscopic images illustrate that **TBP2** easily embedswithin model lipid bilayer membrane without disrupting membrane integrity. **TBP2** displays unique channel behaviour for a longer duration with higher conductance levels (~0.56 nS) in presence of Na^+ while it transports K^+ with greater magnitude of conductance (~0.68 nS) for a shorter period. Remarkably, TEM images elucidated that **TBP2** self-assembles to form vesicular structures and nanofibres. These supramolecular nanostructures contribute to the formation of transmembrane ion channel across model lipid bilayer. Intriguingly, **TBP2** exhibits toxicity towards cancer cells (IC_{50} 8.2 μM for HeLa), which could be due to downregulation of *c-MYC* oncogene expression via its interaction of with *c-MYC* G4, as demonstrated by biophysical and biological assays. Fluorescence based binding studies and NMR titration experiments suggest that **TBP2** shows strong affinity towards *c-MYC* G4 (1:1 stoichiometry) over other G4s and *ds26* DNA. Luciferase reporter assay confirmed that **TBP2** strongly binds to the *c-MYC* promoter region to repress transcription of *c-MYC* in cancer cells. **TBP2** localizes both in the cell membrane and nucleus of HeLa cells as shown via confocal microscopy. Membrane localization of **TBP2** indicates that it has the potential to

form ion channels in cellular system as well. We plan to explore the suitability of **TBP2** as a synthetic transporter in cellular system in future.

Nevertheless, these thiazolyl peptidomimetic cation transporters would provide critical structural and functional aspects of artificial ion channels to guide future efforts in both basic and applied research. The unique properties of these thiazole based small molecules would further help to develop novel synthetic ion transporter with improved chemotherapeutic or drug like properties in pharmaceutical sectors.

References

1. J. Montenegro, M. R. Ghadiri, J. R. Granja, *Acc. Chem. Res.* **2013**, *46*, 2955-2965.
2. F. Otis, M. Auger, N. Voyer, *Acc. Chem. Res.* **2013**, *46*, 2934-2943.
3. A. Fuertes, M. Juanes, J. R. Granja, J. Montenegro, *Chem. Commun.* **2017**, *53*, 7861-7871.
4. J. Kourie, A. Shorthouse, *Am. J. Physiol. Cell Physiol* **2000**, *278*, C1063-C1087.
5. B. Hille, *Ionic Channels of Excitable Membranes*, Sinauer Associates, Inc., Sunderland, MA, 3rd edn, **2001**.
6. M. J. Thompson, J. E. Baenziger, *Nat. Chem. Biol* **2020**, *16*, 1331-1342.
7. N. Sakai, S. Matile, *Langmuir* **2013**, 29, 9031-9040.
8. K. Sato, T. Muraoka, K. Kinbara, *Acc. Chem. Res.* **2021**, *54*, 3700-3709.
9. S. Howorka, *Nat. Nanotechnol.* **2017**, *12*, 619-630.
10. J. R. Burns, N. Al-Juffali, S. M. Janes, S. Howorka, *Angew. Chem. Int. Ed.* **2014**, *53*, 12466-12470; *Angew. Chem.* **2014**, *126*, 12674-12678.
11. S. P. Zheng, L. B. Huang, Z. Sun, M. Barboiu, *Angew. Chem. Int. Ed.* **2021**, *60*, 566-597; *Angew. Chem.* **2021**, *133*, 574-606.
12. J. Yang, G. Yu, J. L. Sessler, I. Shin, P. A. Gale, F. Huang, *Chem* **2021**, 7, 3256-3291.
13. C. J. Haynes, J. Zhu, C. Chimerel, S. Hernández-Ainsa, I. A. Riddell, T. K. Ronson, U. F. Keyser, J. R. Nitschke, *Angew. Chem. Int. Ed.* **2017**, *56*, 15388-15392; *Angew. Chem.* **2017**, *129*, 15590-15594.
14. A. Trabocchi, Small Molecule Drug Discovery, Elsevier: **2020**, pp 163-195.
15. E. Spruijt, S. E. Tusk, H. Bayley, *Nat. Nanotechnol* **2018**, *13*, 739-745.
16. H. Zhang, R. Ye, Y. Mu, T. Li, H. Zeng, *Nano Lett.* **2021**, *21*, 1384-1391.

17. S.-H. Park, S.-H. Park, E. N. Howe, J. Y. Hyun, L.-J. Chen, I. Hwang, G. Vargas-Zuñiga, N. Busschaert, P. A. Gale, J. L. Sessler, *Chem* **2019**, 5, 2079-2098.
18. A. Roy, P. Talukdar, *ChemBioChem* **2021**.
19. N. Rodríguez-Vázquez, M. Amorín, J. Granja, *Org. Biomol. Chem.* **2017**, *15*, 4490-4505.
20. I. Alfonso, R. Quesada, *Chem. Sci.* **2013**, *4*, 3009-3019.
21. F.-F. Shen, S.-Y. Dai, N.-K. Wong, S. Deng, A. S.-T. Wong, D. Yang, *J. Am. Chem. Soc.* **2020,** *142*, 10769-10779.
22. Y. El Ghoul, R. Renia, I. Faye, S. Rassou, N. Badi, V. Bennevault-Celton, C. Huin, P. Guégan, *Chem. Commun* **2013**, *49*, 11647-11649.
23. Y. P. Kumar, R. N. Das, S. Kumar, O. M. Schütte, C. Steinem, J. Dash, *Chem. Eur. J.* **2014**, *20*, 3023-3028.
24. W. Si, P. Xin, Z.-T. Li, J.-L. Hou, *Acc. Chem. Res.* **2015**, *48*, 1612-1619.
25. A. Gilles, M. Barboiu, *J. Am. Chem. Soc.* **2016**, *138*, 426-432.
26. S. Krishnan R, R. Satheesan, N. Puthumadathil, K. S. Kumar, P. Jayasree, K. R. Mahendran, *J. Am. Chem. Soc.* **2019**, *141*, 2949-2959.
27. A. R. Thomson, R. L. Brady, *Nat. Chem.* **2021**, *13*, 643-650.
28. D. P. August, S. Borsley, S. L. Cockroft, F. Della Sala, D. A. Leigh, S. J. Webb, *J. Am. Chem. Soc.* **2020**, *142*, 18859-18865.
29. S. Qi, C. Zhang, H. Yu, J. Zhang, T. Yan, Z. Lin, B. Yang, Z. Dong, *J. Am. Chem. Soc.* **2021**, *143*, 3284-3288.
30. G. Su, M. Zhang, W. Si, Z. T. Li, J. L. Hou, *Angew. Chem. Int. Ed.* **2016**, *55*, 14678-14682; *Angew. Chem.* **2016**, *128*, 14898-14902.

31. R. Ye, C. Ren, J. Shen, N. Li, F. Chen, A. Roy, H. Zeng, *J. Am. Chem. Soc.* **2019**, *141*, 9788-9792.
32. M. Debnath, S. Chakraborty, Y. P. Kumar, R. Chaudhuri, B. Jana, Dash, J., *Nat. commun* **2020**, *11*, 1-12.
33. S. Matile, N. Sakai, A. Hennig, **2012**, 473-500.
34. S. Chen, Y. Wang, T. Nie, C. Bao, C. Wang, T. Xu, Q. Lin, D.-H. Qu, X. Gong, Y. Yang, *J. Am. Chem. Soc.* **2018**, *140*, 17992-17998.
35. Y. El Ghoul, R. Renia, I. Faye, S. Rassou, N. Badi, V. Bennevault-Celton, C. Huin, P. Guégan, *Chem. Commun.* **2013**, *49*, 11647-11649.
36. C. Madhu, C. Voshavar, K. Rajasekhar, T. Govindaraju, *Org. Biomol. Chem.* **2017**, *15*, 3170-3174.
37. D. Dutta, M. Debnath, D. Müller, R. Paul, T. Das, I. Bessi, H. Schwalbe, J. Dash, *Nucleic Acids Res.* **2018**, *46*, 5355-5365.
38. R. Paul, D. Dutta, T. Das, M. Debnath, J. Dash, *Chem. Eur. J.* **2021**, *27*, 8590-8599.
39. S. Asamitsu, S. Obata, Z. Yu, T. Bando, H. Sugiyama, *Molecules* **2019**, *24*, 429.
40. M. L. Bochman, K. Paeschke, V. A. Zakian, *Nat. Rev. Genet.* **2012**, *13*, 770-780.
41. A. Siddiqui-Jain, C. L. Grand, D. J. Bearss, L. H. Hurley, *Proc. Natl. Acad. Sci. U. S. A.* **2002**, *99*, 11593-11598.
42. S. Balasubramanian, L. H. Hurley, S. Neidle, *Nat. Rev. Drug Discov* **2011**, *10*, 261-275.
43. D. Yang, L. H. Hurley, *NUCLEOS NUCLEOT NUCL*. **2006,** *25*, 951-968.
44. V. González, L. H. Hurley, *Annu. Rev. Pharmacol. Toxicol.* **2010**, *50*, 111-129.
45. R. Hänsel-Hertsch, A. Simeone, A. Shea, W. W. Hui, K. G. Zyner, G. Marsico, O. M. Rueda, A. Bruna, A. Martin, X. Zhang, *Nat. Genet.* **2020,** *52*, 878-883.

46. A. T. Phan, V. Kuryavyi, H. Y. Gaw, D. J. Patel, *Nat. Chem. Biol* **2005,** *1,* 167-173.

47. W. Wang, S. Hu, Y. Gu, Y. Yan, D. B. Stovall, D. Li, G. Sui, *Biochim. Biophys. Acta - Rev. Cancer* **2020**, *1874*, 188410.

48. J. Carvalho, J.-L. Mergny, G. F. Salgado, J. A. Queiroz, C. Cruz, *Trends Mol. Med* **2020**, *26*, 848-861.

49. K.-B. Wang, M. S. Elsayed, G. Wu, N. Deng, M. Cushman, D. Yang, *J. Am. Chem. Soc.* **2019**, *141*, 11059-11070.

50. W. Long, B.-X. Zheng, Y. Li, X.-H. Huang, D.-M. Lin, C.-C. Chen, J.-Q. Hou, T.-M. Ou, W.-L. Wong, K. Zhang, *Nucleic Acids Res.* **2022**, *50*, 1829-1848.

51. B.-X. Zheng, M.-T. She, W. Long, Y.-Y. Xu, Y.-H. Zhang, X.-H. Huang, W. Liu, J.-Q. Hou, W.-L. Wong, Y.-J. Lu, *Chem. Commun.* **2020**, *56*, 15016-15019.

52. A. Minard, D. Morgan, F. Raguseo, A. Di Porzio, D. Liano, A. G. Jamieson, M. Di Antonio, *Chem. Commun.* **2020**, *56*, 8940-8943.

53. D. Müller, P. Saha, D. Panda, J. Dash, H. Schwalbe, *Chem. Eur. J.* **2021**, *27*, 12726-12736.

54. M. Zuffo, A. Guédin, E.-D. Leriche, F. Doria, V. Pirota, V. Gabelica, J.-L. Mergny, M. Freccero, *Nucleic Acids Res.* **2018**, *46*, e115-e115.

55. M. Krafcikova, S. Dzatko, C. Caron, A. Granzhan, R. Fiala, T. Loja, M.-P. Teulade-Fichou, T. Fessl, R. Hansel-Hertsch, J.-L. Mergny, *J. Am. Chem. Soc.* **2019**, *141*, 13281-13285.

56. Y. Ma, Y. Wakabayashi, N. Watatani, R. Saito, T. Hirokawa, M. Tera, K. Nagasawa, *Org. Biomol. Chem.* **2021**, *19*, 8035-8040.

Chapter 3B

Folate derived biomimetic transmembrane nanopores

Biological transmembrane pores or channels, consists of membrane proteins that transport ions and various polar molecules across the cell membrane to regulate cellular homeostasis.[1] Malfunction in naturally occurring ion channel gives rise to various channel associated disorders or ´channelopathies´ including cystic fibrosis, alzehimer's, parkinson's, cardiovascular diseases, musculoskeletal disorders, neurological disorders and cancer.[2] Therefore, artificial transporter is often required to ameliorate channelopathies and maintain the physiological balance. Owing to the physiological significance and medical importance of biological pores, in last two decades, biomimicking transmembrane nanopores or ion channels have allured considerable interest to act as therapeutic target, synthetic transporter, drug delivery systems, biosensors and molecular devices.[2-5] However, designing artificial nanopores and replicating the biological processes have been a daunting task to date.

Large number of natural and synthesized ligands can self-assemble to give transmembrane nanopores or ion channels e.g., α-hemolysin, crown ether, macrocycles.[5-8] These ligands can stack together to create a self-assembled channel or pore like structure enabling transportation of ions, proteins, nucleic acids, drugs.[5-10] Natural guanine bases can self-assemble to form the channel like structure which mediates the transport of monovalent cations like Na^+ and K^+.[8-10] Likewise, naturally derived folate also possesses guanosine like structure and can

stack together to give supramolecular rosette membrane channels. Owing to the structural similarity of folate with guanosine, folate derivatives act as one of the potential species to build synthetic nanopores.[8-12] However, folic acid, an active biological molecule (also known as vitamin M or B9) plays crucial role in cell sustainability and proliferation, which can itself acts as therapeutic ligand for cancer.[12-15] The heterocyclic pterine ring in folic acid plays crucial role to regulate cellular functions in biological systems. Researchers are often inspired to design folate derived important biological tools for biomedical applications due to the natural occurrence and excellent self-assembling characteristics of folic acid.[15-29]

Herein, we delineate the synthetic analogues of naturally occurring folate or guanosines that can spontaneously assemble into stable supramolecular nanostructures to form artificial transmembrane nanochannels.

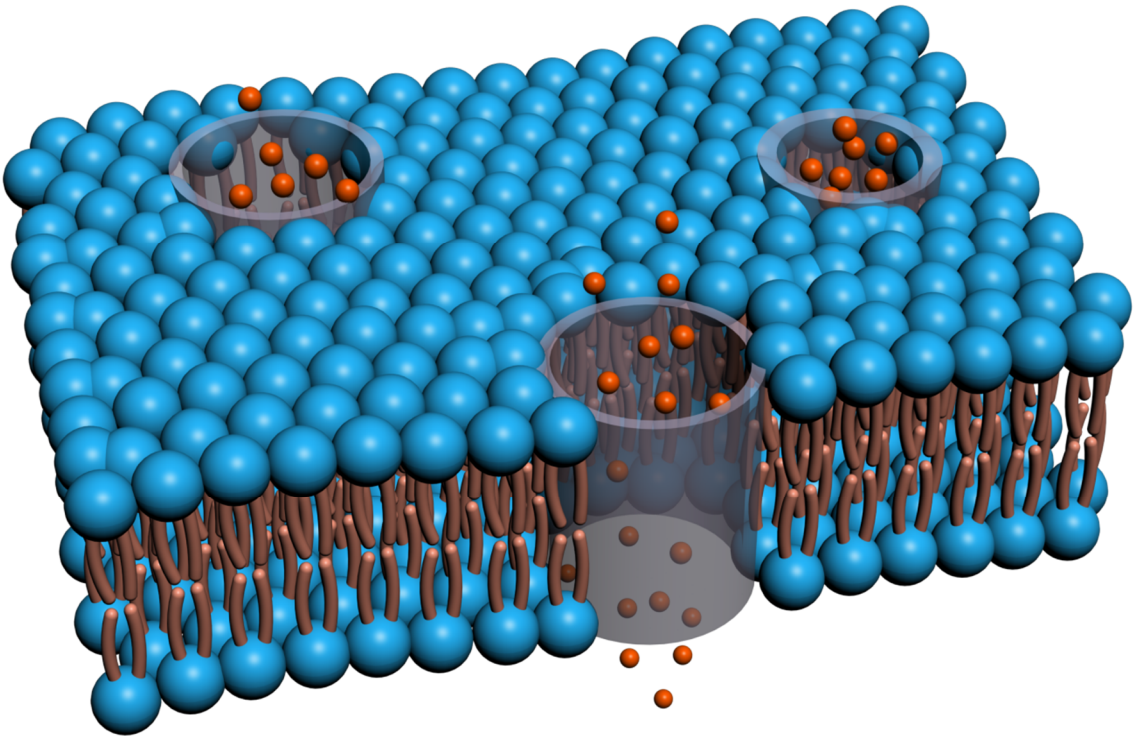

Figure 3B.1. Proposed model of ion transport via folic acid derived synthetic transmembrane nanopore.

Results and Discussion

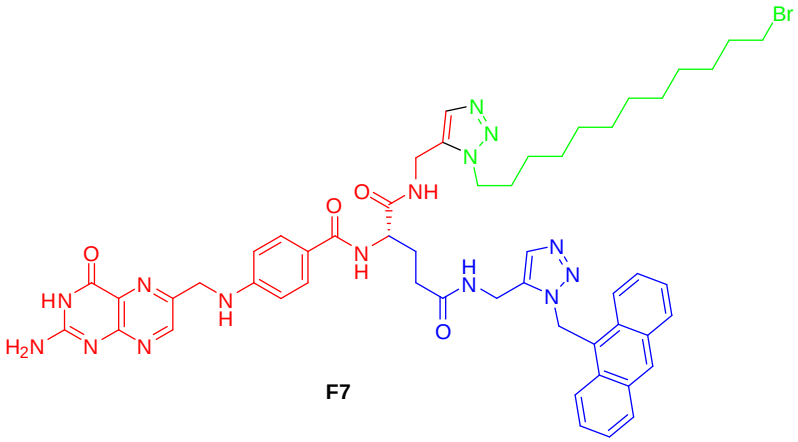

F7

Figure 3B.2. Structure of folic acid derivative.

Ion Transport activity of folate derivatives

The ion-transport behavior of folate derivatives was evaluated by fluorescence based HPTS (8-hydroxypyrene-1, 3, 6-trisulfonic acid trisodium salt) assay: HPTS was entrapped in EYPC (Egg Yolk L-α-Phosphatidylcholine) liposomes (large unilamellar vesicles, LUVs of ~ 400 nm) containing HEPES NaCl or HEPES KCl (10 mM HEPES, 100 mM NaCl or KCl, pH 6.4) buffer. The liposomes were suspended in 10 mM HEPES buffer (pH 6.4) containing 100 mM of MCl_2 (M^{n+}= Na^+, K^+). After introduction of folate derivatives (dissolved in DMSO) in the bilayer membrane, an external pH gradient was generated by NaOH addition. Next, changes in fluorescence intensity of HPTS were observed as a function of time. **F1**, **F2**, **F3**, **F5** showed low or moderate transport activity for Na^+ and K^+ up to a concentration of 100 µM (Figure 3B.2). The folic acid conjugated guanosine with triazole incorporated long alkyl hydrophobic chain linker, **F4** showed increased transport of alkali cations (Na^+ and K^+), while the small aliphatic linker in **F3** does not increase the transport activity as compared to **F4**. In addition, the anthracene conjugated folic acid with benzyl side chain; **F5** displayed no ion transport activity as like **F2**. Hill equation was used to determine the EC_{50} value (concentration of molecules to achieve 50% ion transport activity) of folate derivatives.

Hill equation: $Y = \frac{1}{1+(EC_{50}/[C]_n)}$

EC_{50} value of **F7** for Na^+ and K^+ was determined to be 24.5 µM and 30 µM, respectively while **F4** shows EC_{50} value of 36 µM and 45 µM for K^+ and Na^+, respectively. However, **F1**, **F2**, **F3** and **F5** showed significantly higher EC_{50} (>100 µM) values for both Na^+ and K^+ compared to **F4** and **F7** (Figure 3B.2). The Hill coefficient of **F7** and **F4** for Na^+ (**F7**: $n_{Na+} = 1.83$, **F4**: $n_{Na+} = 1.52$) and K^+ (**F7**: $n_{K+} = 1.54$, **F4**: $n_{K+} = 1.48$) indicates more than one molecule forms the supramolecular ion channel to transport Na^+ and K^+. These results indicated that **F7** and **F4** transport alkali cations with higher efficiency compared to other folate derivatives (Transport efficiency: **F7**>**F4**>**F1**>**F2**>**F3**>**F6**>**F5** for Na^+ and **F4**>**F7**>**F5**>**F1**>**F3**>**F6**>**F2** for K^+).

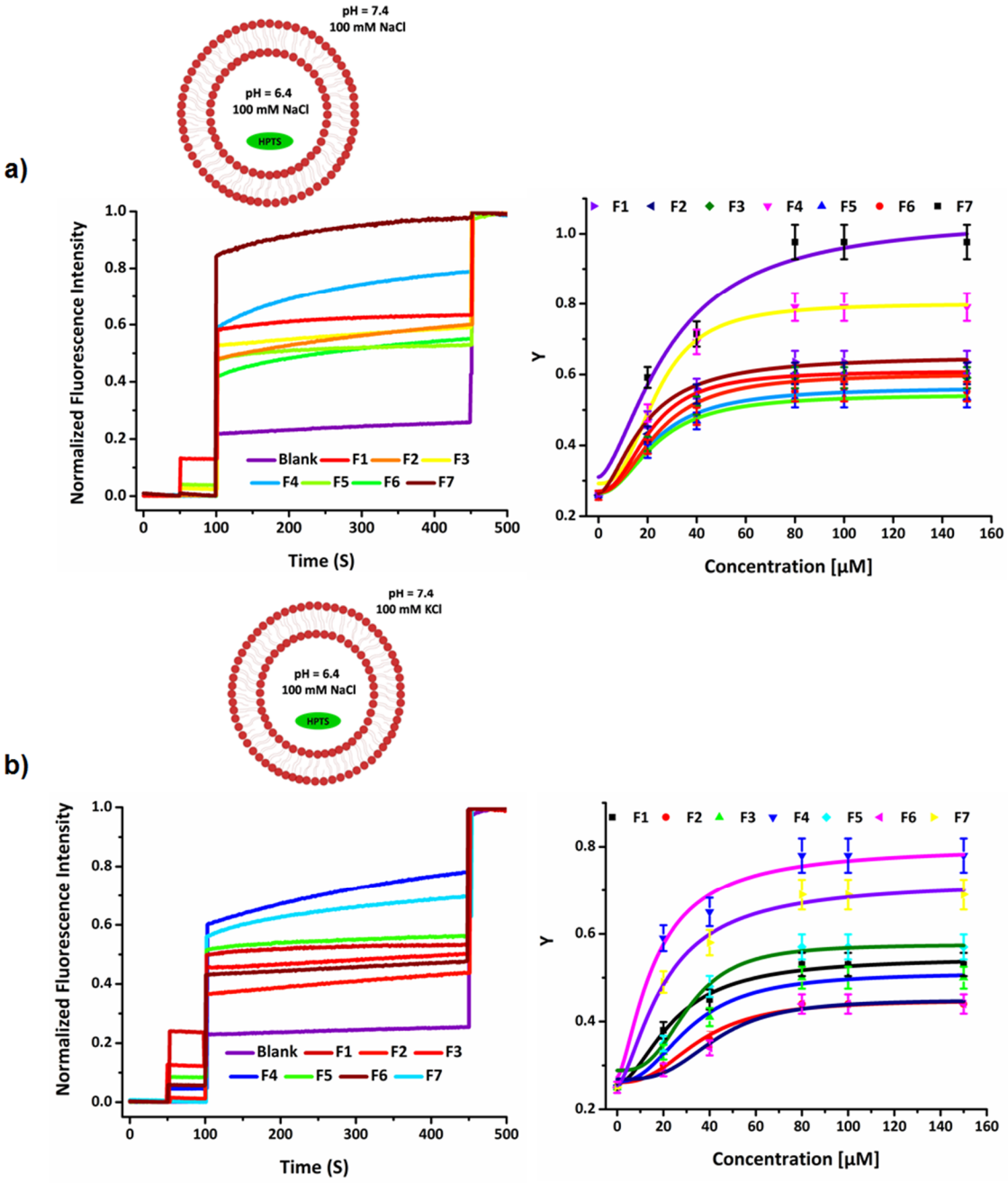

Figure 3B.2. pH-sensitive HPTS assay and determination of EC_{50} value for measuring the ion transport activity of **F1-F7** (80 µM) in presence of Na^+ and K^+ ions. a) Buffer composition: External – 10 mM HEPES 100 mM NaCl (pH 7.4), Internal – 10 mM HEPES 100 mM NaCl (pH 6.4), b) Buffer composition: External – 10 mM HEPES 100 mM KCl (pH 7.4), Internal – 10 mM HEPES 100 mM NaCl. (pH 6.4).

*Membrane permeability after treatment with **F7** and **F4***

To determine the effects of **F7** and **F4** on membrane permeability, a self-quenched carboxyfluorescein dye (CF) (<1 nm in size) was encapsulated inside the LUVs (Fig. 3B.3). In principle of CF leakage assay, highly fluorescent monomeric CF molecules form nearly non-fluorescent dimers at 40-50 mM. Likewise, the membrane impermeable CF dye (40 mM) can efflux from the vesicles owing to formation of a pore of >1 nm or disruption of the LUVs, which in turn will cause increase in fluorescence intensity. The percentage of CF release can be measured by monitoring the fluorescence intensity of released CF after addition of compounds compared to a 100% release by destroying the liposomes using 1X cell lysis buffer. The percentage release of CF from LUVs into the extravesicular solution of HEPES-KCl (10 mM HEPES, 100 mM KCl, pH 7.4) after addition of **F7** and **F4** was calculated to be 12.3% and 10% respectively, after 8 min. However, the CF release was observed to be 29% and 13% for **F7** and **F4**, respectively in extravesicular solution of HEPES-NaCl (10 mM HEPES 100 mM NaCl, pH 7.4). These data indicate conserved membrane integrity in the presence of both **F7** and **F4**. However, the CF leakage data illustrated that **F7** could create larger openings or insertions in the membrane compared to the **F4**.

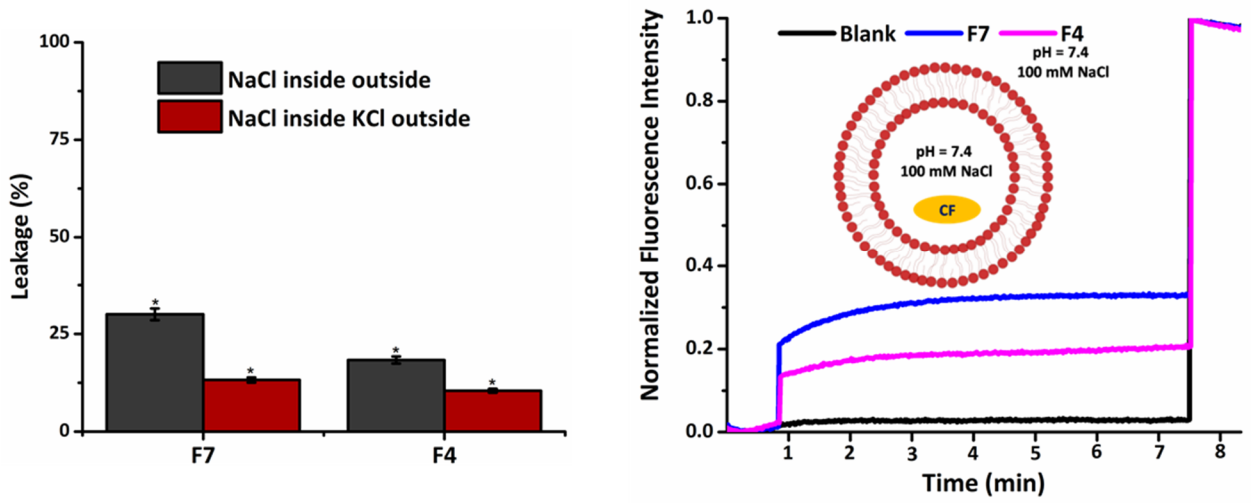

Figure 3B.3. CF leakage assay. Determination of CF release percentage in the presence of **F7** and **F4** (External: 10 mM HEPES 100 mM NaCl or KCl, pH 7.4, Internal: 10 mM HEPES 100 mM NaCl, pH 7.4) after 8 minutes.

F7 and F4 bind to the membrane of the vesicles

In order to understand the binding and insertion property of both **F7** and **F4** to the large unilamellar vesicle membrane, fluorescence titration study was carried out in HEPES NaCl or HEPES KCl (pH 7.4) buffer. **F7** (5 µM) and **F4** (5 µM) exhibited fluorescence emission maxima at 440 nm when excited at 325 nm. After subsequent addition of homogeneous solution of LUVs in HEPES NaCl buffer, fluorescence of **F7** and **F4** increased up to ~ 2 fold and ~ 1.5 fold till saturation, respectively (Figure 3B.4a). In HEPES KCl buffer, both **F7** and **F4** displayed ~ 1.7 fold fluorescence enhancement after addition of LUVs. This result indicates that ´turn on´ fluorescence could be due to the interaction of **F7** and **F4** with the lipid membrane.

Confocal microscopy was performed by the formation of GUVs (stained with nile red) to further assess the membrane embedding feature of **F7** and **F4**. Addition of **F7** and **F4** (10 µM), resulted in adsorption and colocalization with the membrane staining dye nile red into GUV membrane (Figure 3B.4b) while no changes in fluorescence of control or untreated GUVs were detected. Thus, the fluorescence titration study and confocal microscopy demonstrated that **F7** and **F4** can incorporate into the lipid membrane of both LUVs and GUVs.

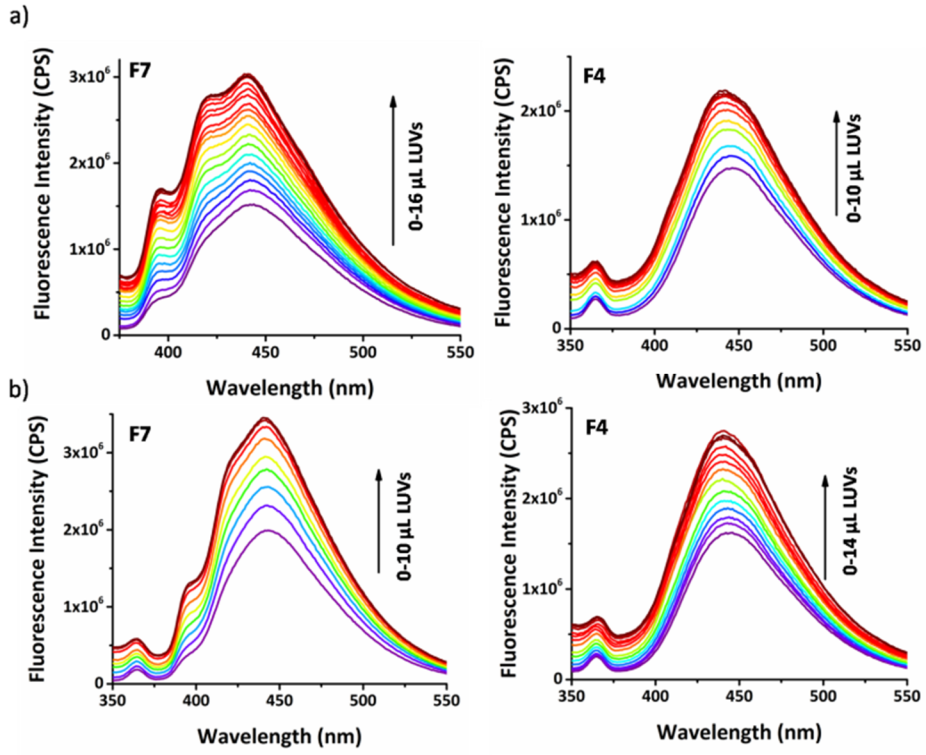

Figure 3B.4. Fluorescence titration of **F7** and **F4** with increasing amount of LUVs in a) External and internal 10 mM HEPES 100 mM NaCl buffer, pH 7.4 or b) External 10 mM HEPES 100 mM KCl buffer, Internal 10 mM HEPES 100 mM NaCl buffer, pH 7.4.

Voltage dependent ion transport by folate derivatives via the planar lipid bilayer

The planar lipid bilayer experiments provide further insight into the channel formation behavior of **F7** and **F4**. *Cis* and *trans* compartments containing 1 M NaCl or 1 M KCl solution were separated by a planar lipid bilayer membrane composed of egg yolk L-α-Phosphatidylcholine (EYPC) lipid. The addition of **F7** resulted in characteristic channel openings and closing at different applied potentials, showing the potential to form transmembrane ion channel. The ion transport activity is preferably faster and immediately starts after the addition of **F7** (Figure 3B.5). **F7** generates stronger transport activity with longer opening period and high conductance intensity in the presence of 1 M NaCl. Longer events (~ 1s) with the average opened-state conductance ~ 6 nS (multi-level conductance type) were observed at the holding potential of -100 mV. Intriguingly, this open state correlates the formation of conductance channels with step-like behavior. The transitions between the open steps are very rapid and this behavior might be characterized by the rapid interconversion of different open states. However, **F7** displays the average conductance of ~ 3 nS in the presence of 1 M KCl at the same applied potential of -100 mV. **F4** exhibits intense transport activity within a shorter opening time period (~ 0.2 s) with the average conductance of ~ 5 nS at -100 mV in presence of 1 M KCl.

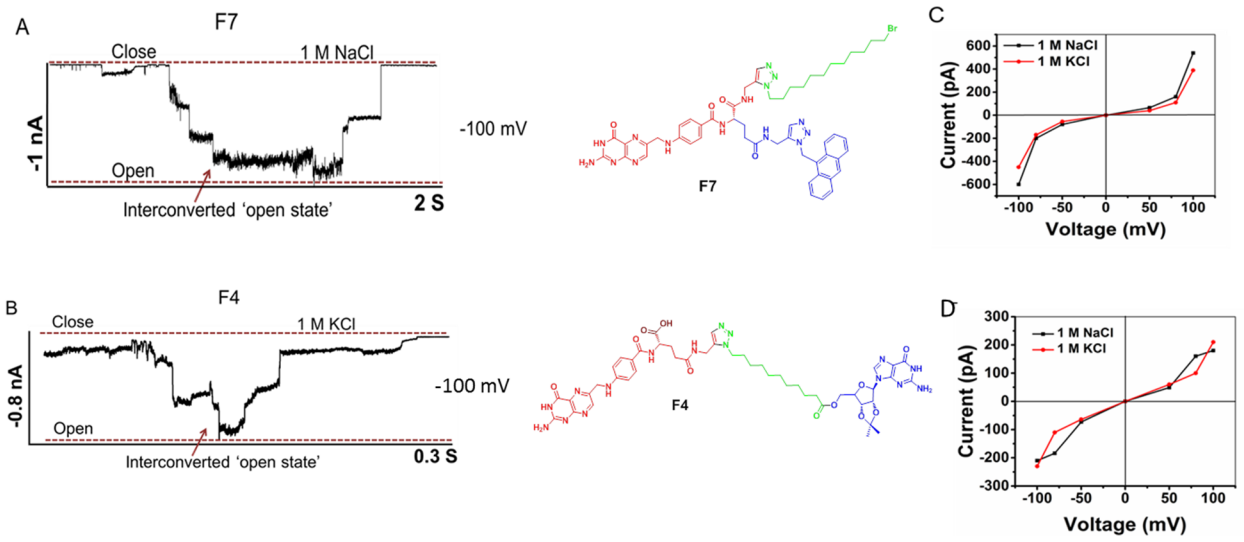

Figure 3B.5. Ion conductance measurement of A) **F7** and B) **F4** in the presence of 1M NaCl or 1M KCl at -100 mV, respectively. I-V curve plot of (C) **F7** and (D) **F4** in the presence of 1 M NaCl or 1 M KCl.

*Membrane spanning and nanopore forming ability of **F7** and **F4***

A dye influx assay was carried out to validate whether the folate derivatives **F7** and **F4** can span the membrane bilayer and form large porous or channel like structures (Figure 3B.6). In the assay, **F7** or **F4** were added to lipid vesicles that were immersed in fluorophore-containing (ATTO 633 or FITC dextran) solution. The membrane-spanning **F7** were expected to facilitate dye influx into vesicles. The results of the influx assay with EYPC GUVs and a small fluorophore dye ATTO 633 of around 1 nm size are summarized in Figure 3B.6. The fluorescence intensity within the vesicles was tracked using confocal microscopy and plotted as a function of time. The membrane-spanning **F7** and **F4** caused an increase in fluorescence inside the GUVs compared to untreated or control.

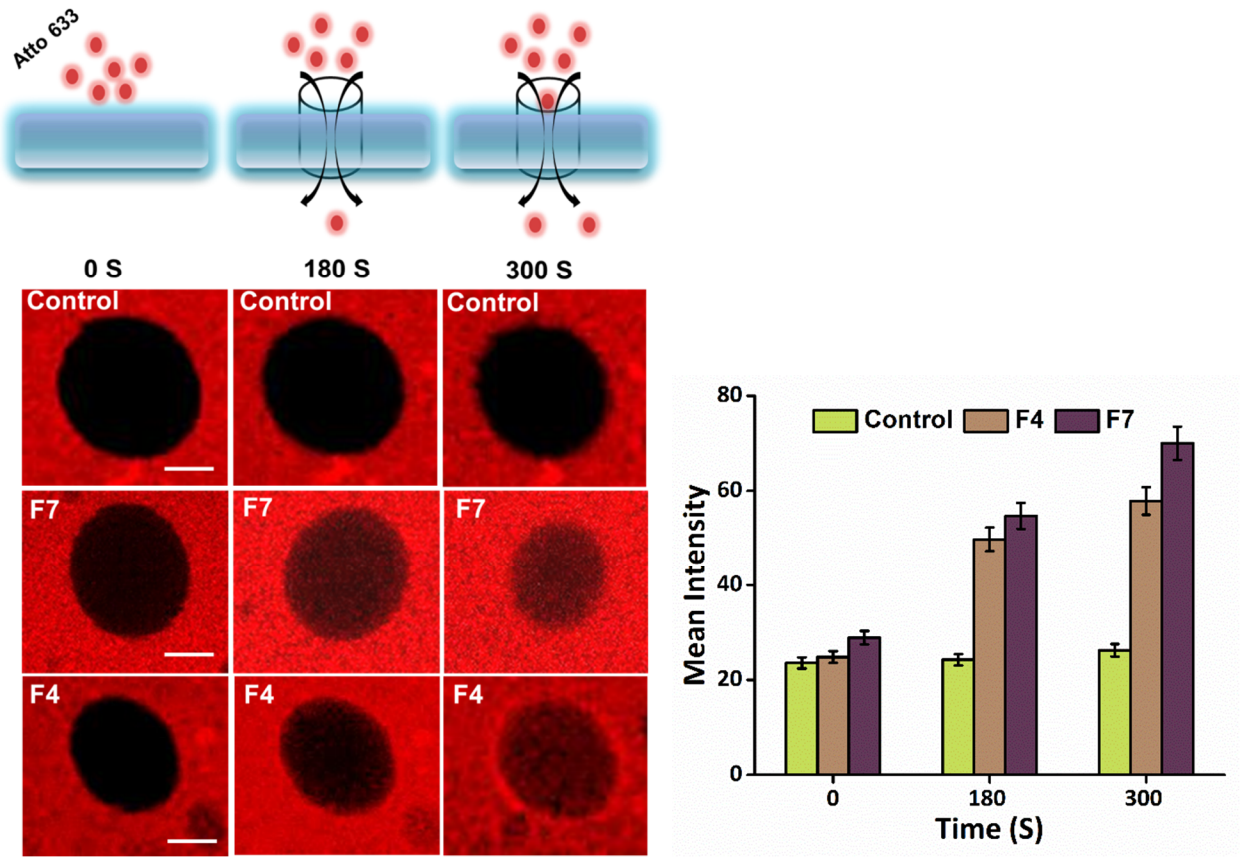

Figure 3B.6. Dye influx assay with **F7** and **F4** using EYPC GUVs exposed to fluorophore ATTO 633. **F7** and **F4** cause dye influx inside the GUVs in a time dependent manner and likely span the membrane. Scale bar represents 1 µm.

Confocal images revealed that fluorescence intensity of Atto633 was increased up to ~ 4-fold and ~ 3-fold after 300 secs of treatment with **F7** and **F4**, respectively. Fluorescence analysis revealed that **F7** or **F4** did not assist influx of the large dye, FITC, which concludes the bilayer-spanning nature of **F7** and **F4** rather than any nonspecific membrane disruption. The data indicate that the flexible small molecules, **F7** and **F4** can span the membrane and allows the influx of smaller molecule Atto633 inside the GUVs.

Imaging the membrane nanopore at single molecule level

The optical single channel recording (oSCR) was performed to visualize the influx of fluorophore (Fluo-8H) tagged Ca^{2+} via the ligand induced membrane pore of DPhPC Droplet Interface Bilayers (DIBs) system using total internal reflection fluorescence (TIRF) microscopic imaging (Figure 3B.7).

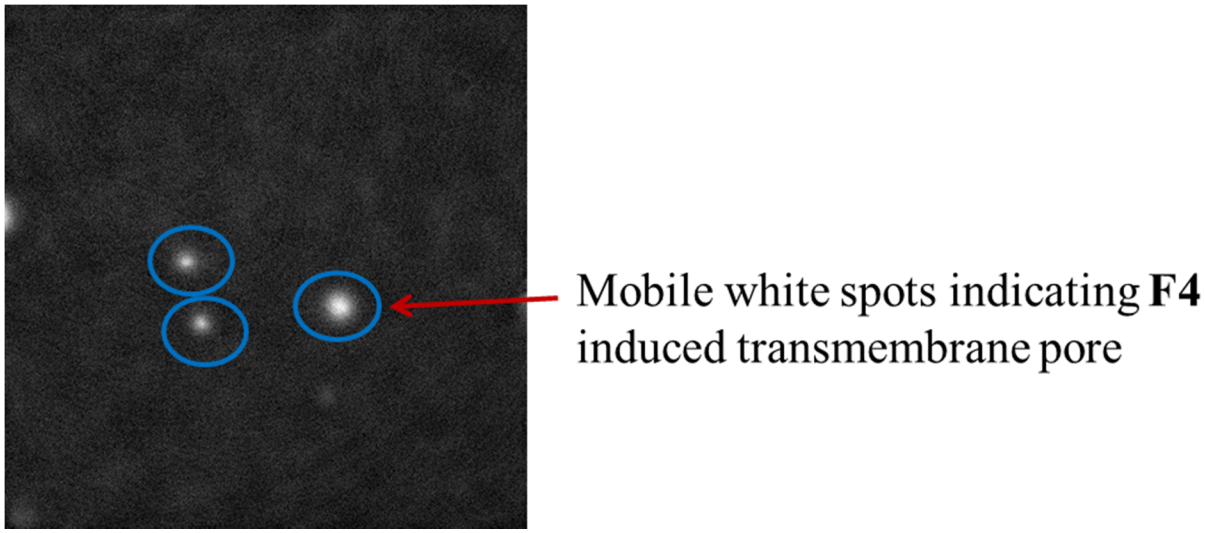

Figure 3B.7. Optical single channel recording of **F4** mediated Ca^{2+} channel in a DPhPC lipid membrane via total internal reflection fluorescence microscopy (TIRF).

The calcium-flux imaging showed multiple mobile spots diffusing in the plane of the bilayer that indicates the formation of transmembrane pore via the lipid membrane. The fluorescence images with distinct intensity further illustrates that the folate derivatives could create membrane pores with multiple conductance behavior.

Structure effect on transport activity

Transmission Electron Microscopy (TEM) images were taken to investigate possible structure formation due to the self-assembly of **F7** and **F4**. TEM imaging revealed helical filamentous nanostructures in addition to linear nanofibers of average width ~ 6 nm (Figure 3B.8). Intriguingly, microscopic images also indicate that the nanofibers are connected together via branched chains. Formation of fibroid type structures might result from extensive aggregation or contact of aromatic surfaces.

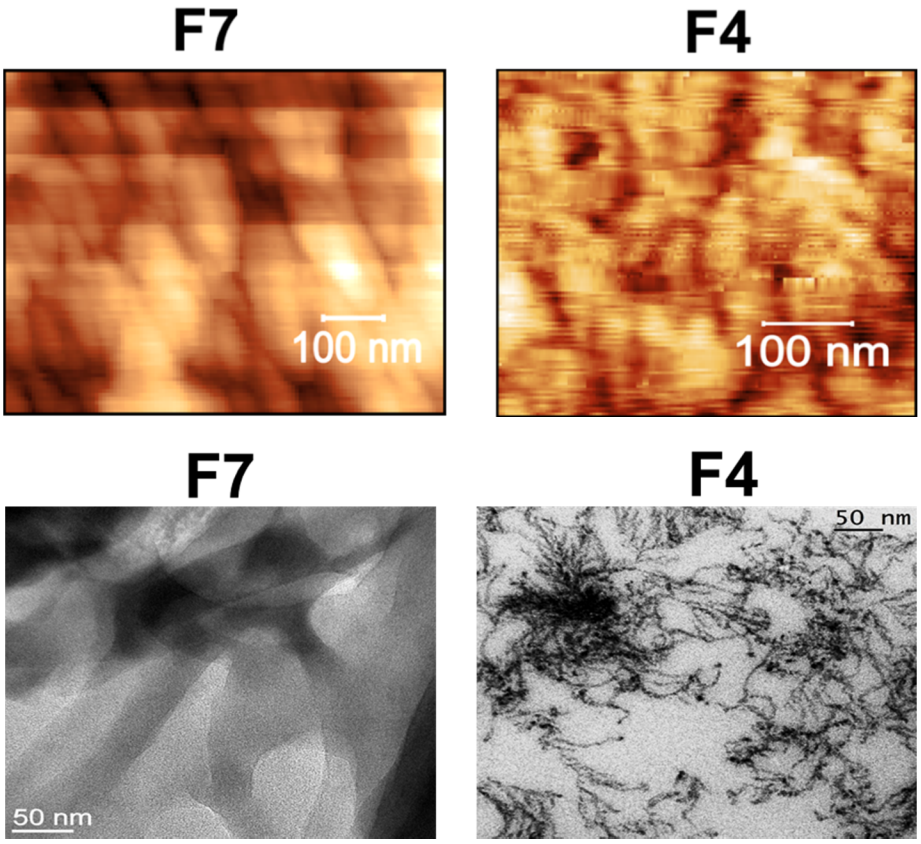

Figure 3B.8. AFM and TEM images of **F7** and **F4**.

Conclusion

The folate derivatives **F7** and **F4** can act as cation (Na^+ and K^+) transporting highly conductive (~ 6 nS) transmembrane nanopores. Both **F7** and **F4** can self-assemble to form nanostructures, enabling the transportation of ions across the lipid membrane. The fluorescence titration and confocal microscopy revealed that **F7** and **F4** can efficiently bind to the vesicular membrane and co-localizes with membrane staining dye nile red. The permeation of Atto633 dye within GUV membrane indicates that the long hydrophobic chain in **F7** plays crucial role in the formation of large porous structure (~ 4.8 nm) which allow the influx of Atto 633 dye (~1 nm) inside the GUVs. The structure and functional properties and the distinctive assembly pathway of **F4** and **F7** were elucidated by single-channel current recording. The high conductance rate indicates that both **F7** and **F4** form large porous structure due to self-assembly of folic acid-anthracene conjugate (**F7**) and folic acid-guanosine conjugate (**F4**) with long hydrophobic chain linker. This study would further propagate the discovery of nanopore based biomolecular devices and rational framework to design synthetic transporters in biological system.

References

1. J. K. Chui, T. M. Fyles, *Chem. Soc. Rev.*, **2012,** *41*, 148-175.
2. S. K. Bagal, A. D. Brown, P. J. Cox, K. Omoto, R. M. Owen, D. C. Pryde, B. Sidders, S. E. Skerratt, E. B. Stevens, R. I. Storer, *J. Med. Chem.* **2013,** *56* 593-624.
3. G. W. Gokel, I. A. Carasel, *Chem. Soc. Rev.*, **2007,** *36*, 378-389.
4. A. L. Sisson, M. R. Shah, S. Bhosale, S. Matile, *Chem. Soc. Rev.*, **2006,** *35*, 1269-1286.
5. G. W. Gokel, S. Negin, *Acc. Chem. Res.* **2013,** *46*, 2824-2833.
6. S. Howorka, *Nature nanotechnology* **2017**, *12*, 619-630.
7. F. Ciuchi, G. Di Nicola, H. Franz, G. Gottarelli, P. Mariani, M. G. Ponzi Bossi, G. P. Spada, , *J. Am. Chem. Soc.* **1994**, *116*, 7064-7071.
8. M. S. Kaucher, W. A. Harrell, J. T. Davis, *J. Am. Chem. Soc.* **2006**, *128*, 38-39.
9. S. Sivakova, S. J. Rowan, *Chemical Society Reviews* **2005**, *34*, 9-21.
10. N. Rodríguez-Vázquez, A. Fuertes, M. Amorín, J. R. Granja, in *The Alkali Metal Ions: Their Role for Life*, Springer, **2016**, pp. 485-556.
11. N. Sakai, Y. Kamikawa, M. Nishii, T. Matsuoka, T. Kato, S. Matile, *J. Am. Chem. Soc.* **2006**, *128*, 2218-2219.
12. L. Ma, M. Melegari, M. Colombini, J. T. Davis, *J. Am. Chem. Soc.* **2008**, *130*, 2938-2939.
13. Y. H. Li, S. Zheng, Y. M. Legrand, A. Gilles, A. Van der Lee, M. Barboiu, Structure-Driven Selection of Adaptive Transmembrane Na^+ Carriers or K^+ Channels. *Angew. Chem. Int.* **2018**, *57*, 10520-10524; *Angew. Chem.* **2018**, *57*, 10520-10524.
14. S. Majd, E. C. Yusko, Y. N. Billeh, M. X. Macrae, J. Yang, M. Mayer, *Curr. Opin. Biotechnol.* **2010**, *21*, 439-476.
15. S. Qi, C. Zhang, H. Yu, J. Zhang, T. Yan, Z. Lin, B. Yang, Z. Dong, *J. Am. Chem. Soc.* **2021**, *143*, 3284-3288.

16. H. Zhang, R. Ye, Y. Mu, T. Li, H. Zeng, *Nano Letters* **2021**, *21*, 1384-1391.
17. S. P. Zheng, Y. H. Li, J. J. Jiang, A. van der Lee, Dumitrescu, D.; Barboiu, M., Self-Assembled Columnar Triazole Quartets: An Example of Synergistic Hydrogen-Bonding/Anion–π Interactions. *Angew. Chem. Int.* **2019**, *131*, 12165-12170; *Angew. Chem.* **2019**, *131*, 12165-12170.
18. L. L. Lock, M. LaComb, K. Schwarz, A. G. Cheetham, Y.-a. Lin, P. Zhang, H. Cui, self-assemble folic acid. *Faraday Discuss.* **2013**, *166*, 285-301.
19. C. Lang, X. Deng, F. Yang, B. Yang, W. Wang, S. Qi, X. Zhang, C. Zhang, Z. Dong, J. Liu, Highly selective artificial potassium ion channels constructed from pore-containing helical oligomers. *Angew. Chem. Int.* **2017**, *56*, 12668-12671; *Angew. Chem.* **2017**, *56*, 12668-12671.
20. S. Krishnan R, R. Satheesan, N. Puthumadathil, K. S. Kumar, P. Jayasree, K. R. Mahendran, Autonomously assembled synthetic transmembrane peptide pore. *J. Am. Chem. Soc.* **2019**, *141*, 2949-2959.
21. X. Hou, W. Guo, L. Jiang, Biomimetic smart nanopores and nanochannels. *Chem. Soc. Rev.*, **2011**, *40*, 2385-2401.
22. A. Seifert, K. Göpfrich, J. R. Burns, N. Fertig, U. F. Keyser, S. Howorka, Bilayer-spanning DNA nanopores with voltage-switching between open and closed state. *ACS Nano.* **2015**, *9*, 1117-1126.
23. P. Chidchob, D. Offenbartl-Stiegert, D. McCarthy, X. Luo, J. Li, S. Howorka, H. F. Sleiman, Spatial presentation of cholesterol units on a DNA cube as a determinant of membrane protein-mimicking functions. *J. Am. Chem. Soc.* **2018**, *141*, 1100-1108.

24. J. E. Jones, V. Diemer, C. Adam, J. Raftery, R. E. Ruscoe, J. T. Sengel, M. I. Wallace, A. Bader, S. L. Cockroft, J. Clayden, *J. Am. Chem. Soc.* **2016**, *138*, 688-695.
25. S. Vanuytsel, J. Carniello, M. I. Wallace, *ChemBioChem* **2019**, *20*, 2569-2580.
26. J. A. Malla, R. M. Umesh, A. Vijay, A. Mukherjee, M. Lahiri, P. Talukdar, *Chem. Sci.* **2020**, *11*, 2420-2428.
27. D. Basak, S. Sridhar, A. K. Bera, N. Madhavan, *Bioorg. Med. Chem. Lett.* **2017**, *27*, 2886-2889.
28. M. Debnath, S. Chakraborty, Y. P. Kumar, R. Chaudhuri, B. Jana, J. Dash, *Nat. Commun.* **2020**, *11*, 1-12.
29. R. N. Das, Y. P. Kumar, O. M. Schütte, C. Steinem, J. Dash, *J. Am. Chem. Soc.* **2015**, *137*, 34-37.

Materials and Methods

General information

The common chemicals, lipids (DPhPC, EYPC), Sephadex G-25 column and unlabeled DNA sequences were procured from Sigma-Aldrich, Avanti Polar Lipids, Bio-Rad and Integrated DNA Technologies (IDT, USA). HPLC purified unlabeled DNA sequences were procured to obtain the best results. Hexadecane, EDTA, $CaCl_2$, KCl, HEPES (4-(2-Hydroxyethyl)piperazine-1-ethanesulfonic acid), agarose and alamethicin were purchased from Sigma-Aldrich. Quest Fluo-8H sodium salt was obtained from ABD Bioquest. The buffers were prepared freshly and filtered prior to use (0.2 μm cellulose acetate, Nalgene) and buffers used to make droplets were treated with Chelex 100 Chelating Ion Exchange Resin (Biotechnology Grade, 100-200 mesh, BioRad) to reduce the divalent ion concentration before the addition of Fluo-8H.

The reagents used in cell culture were bought from Thermo Fisher Scientific (USA) and the antibodies were procured from Santa-cruz Life Technologies, Invitrogen (USA). The *c-KIT* promoter was cloned into pGL4.72 plasmid from Biobharati Life Sciences. The luciferase reporter assay kit was procured from Promega.

Chapter 1A

Experimental unit

Melting experiments by FRET

The stock solution of 5′-FAM (Ex. 490 nm/Em. 520 nm) and 3′-TAMRA (Ex. 555 nm/Em. 580 nm) labeled oligo sequences were first diluted to 0.4 μM using a 60 mM potassium cacodylate (KCaco, pH 7.4) buffer. The diluted solution was then heated to 95 °C for 1 min, cooled slowly to room temperature and kept overnight at 4°C. Subsequently, the DNA solution (0.2 μM) was incubated with the **TPW TPE TPA TBE TBA** (0 - 10 equivalent) in 60 mM potassium cacodylate buffer at pH 7.4 for 1 h, using a blank 96-well plate (Axygen) with a total volume of 100 μL for each well. In the presence of 60 mM K^+, the labeled G4 forming sequence is mainly present in a quadruplex form where the FAM is in close distance to the TAMRA showing a low FAM fluorescence due to the FRET. With increasing temperature, the conformation of G4 changes to a single-stranded form where the FAM is far from the TAMRA, which results in a high FAM fluorescence. Melting curves for the determination of melting temperature (T_M) were then obtained by recording FAM fluorescence with increasing temperatures from 37 to 95 °C at the rate of 0.9 °C/min using Roche Light Cycler II. The analysis of T_M vaules was accomplished using OriginPro 2016 software. The ΔT_M values were then plotted

against concentration of ligands to determine the stabilization potential for G4s. Further details for FRET study are provided in the supplementary information.

Fluorometric titration

Fluorescence spectra were recorded on a Horiba JobinYvon Fluorolog instrument at 25 °C in a thermostated cell holder using quartz cuvette of 1 cm path-length. The DNA sequences used in the study are:

- *c-KIT1: 5′-d($G_3AG_3CGCTG_3AG_2AG_3$)-3′*
- *c-KIT2: 5′-d($G_3CG_3CGCTAG_3AG_4$)-3′*
- *c-KIT*: 5′-d($G_2CGAG_2AG_4CGTG_2C_2G_2C$)-3′*
- *c-MYC (Pu27): 5′-d($TG_4AG_3TG_4AG_3TG_4A_2G_2$)-3′*
- *BCL-2: 5′-d($G_3CGCG_3AG_2A_2T_2G_3CG_3$)-3′*
- *KRAS: 5′-d($AG_3CG_2TGTG_3A_2GAG_3A_2GAG_3A_2GAG_5AG_2$)-3’*
- *h-TELO: 5′-d($T_2G_3T_2AG_3T_2AG_3AT_2AG_3A$)-3′*
- *ds26* DNA*: 5′-d($CA_2TCG_2ATCGA_2T_2CGATC_2GAT_2G$)-3′*

Fluorescence spectroscopic titrations were performed on Horiba Jobin Yvon Fluoromax 3 instrument at 25 °C in a quartz cuvette (path-length 1 mm) with consecutive addition of pre-annealed DNA into 10 μM ligand in 60 mM potassium cacodylate buffer (pH 7.4). DNA sequences were pre-annealed in 60 mM potassium cacodylate buffer (pH 7.4) by heating in a dry bath to 95 °C for 5 min

followed by gradual cooling to 25 °C (0.1 °C /min) and incubated overnight at 4 °C. Stock solutions (10 μM) of thiazole containing polyamides were prepared in filtered and extremely degassed potassium cacodylate buffer. Ligand solutions were mixed and titrated with the pre-annealed G4 and *ds26* DNA samples and the emission was measured from the wavelength range of 300 – 500 nm (λ_{ex} = 290 nm) for **TPW**, 340 – 600 nm (λ_{ex} = 325 nm) in **TPE** and 300 – 550 nm (λ_{ex} = 290 nm) for compounds **TPA**, **TBE** and **TBA**. The Hill 1 equation was used with Origin software to calculate the binding constants.

$$F = F_0 + \frac{(F_{max} - F_0)\,[DNA]}{K_d + [DNA]}$$

Where *F* denotes fluorescence intensity, F_{max} for maximum fluorescence, F_0 for fluorescence in the absence of DNA and K_d indicates dissociation constant.

Limit of detection of **TPW**:

The limit of detection was calculated from the fluorescence titration data based on a reported method. The fluorescence spectrum of **TPW** was measured by six times and the standard deviation of blank measurement was achieved.[1] To gain the slope, the normalized fluorescent intensity data at 455 nm was plotted against the concentration of *c-KIT1* G4 DNA (μM). So the detection limit was calculated with the following equation:

Detection limit = 3σ/b

Where σ is the standard deviation of blank measurement, and b is the slope between the fluorescence vs. DNA concentration.

Thiazole orange displacement experiment

The assay was carried out on Horiba Jobin Yvon Fluoromax 3 at room temperature in a quartz cuvette (path-length 1 mm). To perform this experiment we chose **TPW**, the most potent and selective *c-KIT1* G-quadruplex binding ligand in the series, evaluated using fluorescence titration study. DNA sequences were pre-annealed as described before in fluorometric titration. A solution of pre-annealed G4-DNA (0.25 μM) and 0.50 μM thiazole orange (TO) was prepared and incubated for 2 min and fluorescence spectrum was monitored (λ_{ex}= 501 nm; λ_{em}= 510 − 650 nm). Then, **TPW** was added to the solution gradually with a 2 min equilibration time, and the fluorescence was measured. The TO displacement (%) was calculated using the following basic equation:

TO displacement or Relative fluorescence change (%)

$$= \mathbf{100} - \left(\frac{F}{F_0} \times 100\right)$$

Where, F denotes fluorescence intensity (F) at the emission maxima and F_0 denotes the initial fluorescence of TO-G4 complex

The TO displacement percentage was presented as a function of concentration of mixed **TPW** to determine the DC_{50} value.

Isothermal calorimetry

Calorimetric titrations were carried out in a MicroCal PEAQ-ITC system (Malvern). The DNA samples (5 μM in 60 mM potassium cacodylate buffer, pH 7.4) were pre-annealed via heating at 95 °C for 5 min followed by gradual cooling to room temperature (0.1 °C /min) and incubated overnight at 4 °C. Experiments were performed by overfilling the pre-annealed DNA samples (5 μM) in 300 μL sample cell followed by titration with duly prepared 50 μM ligand solution over 20 injections at an interval of 150 secs. The temperature of the reference and sample cells was preserved at 25 °C during the experiment with a reference power of 10 μcal/sec and the continuous stirring of sample cell solution was maintained at a speed of 750 rpm. Samples were extensively degassed immediately before use. The raw data were analyzed by Malvern ITC Analysis software provided with the instrument. The data fitting was done using an appropriate binding model. The dissociation constant (K_d), Gibb's free energy change (ΔG), enthalpy of reaction (ΔH) and entropy (ΔS) change were calculated using the following equation:

$$\Delta G = \Delta H - T\Delta S$$

Cell culture

Human bone marrow chronic myeloid leukemia cells (K562), lung carcinoma cells (A549), cervical cancer cells (HeLa), breast cancer cells (MCF-7) and human normal kidney epithelial cells (NKE) were procured from the National Centre for Cell Science (NCCS), Pune. These cells were cultured in RPMI-1640, DMEM (Dulbecco's Modified Eagle Medium) and MEM (Minimum Essential Medium) supplemented with L-glutamine, D-glucose, penicillin–streptomycin (Invitrogen) and 10% FBS (Fetal Bovine Serum) (Gibco). The K562 and HeLa cells were placed in 6-well plates (~ 10^6 cells each well) and incubated in a 5% CO_2 incubator at 37 °C to obtain ≥70% confluency before ligand treatment. Next, the cells were kept as control or treated with ligands followed by incubation under the same environment for the specified stretch of time and further analysis was accomplished.

Cell viability assay

The cell viability assay was based on the measurement of optical density of the orange-colored water soluble formazan salt produced by viable cells with active mitochondrial dehydrogenases (mitochondrial reduction of tetrazolium salt). According to the manufacturer's instruction, K562, HeLa, A549, MCF-7 and NKE cells were plated in 96-well microtiter plates and treated with different concentrations of **TPW** and **TPE** (Control, 0.2, 0.5, 1.0, 2.0, 4.0, 5.0, 10.0, 20.0,

50.0, 80.0, 100.0, 150.0 and 200 µM)for 24 hours before incubation with the XTT (2,3-bis-(2-methoxy-4-nitro-5-sulfophenyl)-2H-tetrazolium-5-carboxanilide) labeling mixture at 37 °C. The measurement of spectrophotometric absorbance was done using an ELISA microplate reader at 450 nm with a 630 nm reference filter. The cytotoxicity was evaluated based on the percentage of cell survival in a dose-dependent manner with regard to the negative control. The final IC_{50} values were calculated by using the OriginPro 2016.

Immunodetection of G-quadruplex

Cells grown on glass cover slips were kept as control or treated with two doses of **TPW** and **TPE** (20 µM and 40 µM) for 24 h. In the following day, cells were washed with 1X PBS and fixed in chilled acetone-methanol (1:1) and permeabilized with 0.03% saponin/PBS solution. After blocking with 3% BSA in 1X PBS, immunofluorescence was carried out using regular or standard methods, incubating at 37 °C with BG4 antibody (Mouse monoclonal, from Merck) diluted 1:200 in 1X PBS overnight, and Alexafluor 647-conjugated secondary antibody (Invitrogen) for 2 h on next day. Finally, cover slips were mounted with antified solution (Invitrogen). The BG4 emission (570−670 nm) was assembled with the excitation at 559 nm, sequentially. Digital images were taken in a Confocal Laser Scanning Microscope (LSM-800, Zeiss). For the quantification of BG4 foci, >50 cells were counted using FIJI ImageJ software and the standard error of the mean

was calculated from three replicates, *P <0.05 (Student's 't' test) was considered as statistically significant.

Quantitative real-time PCR (qRT PCR)

K562 cells (~ 10^6 per well) were placed in a 6-well plate and allowed to incubate overnight. Next day, cells were treated with **TPW** (20 µM, 40 µM) and **TPE** (20 µM, 40 µM) and harvested for 24 h. Untreated (control) cells and those treated with DMSO control were used to evaluate primary *c-KIT* expression levels. Total RNA was isolated using the TRIzol reagent (Invitrogen) according to the manufacturer's instructions. RNA quantification was carried out by a Cary Win 300 UV-Vis spectrophotometer and the total 500 ng of RNA was employed as a template for cDNA synthesis using a Verso kit (Thermo Fisher Scientific) as per the supplied protocol. Real-time PCR was carried out on Roche LightCycler 480 by the use of SYBR Premix (Applied Biosystems), according to the manufacturer's instructions. The C_T values were normalized to 18s rRNA and compared to the untreated or control cells. The C_T method (comparative cycle threshold method) was used to calculate relative mRNA expression. The mRNA level was expressed in terms of fold changes of target gene with respect to control or untreated value of 0. Three biological replicates were employed for the quantifications. The

significance level was statistically analyzed by employing a Student's t test, and results were statistically significant when *P < 0.05.

The qRT PCR was done using following primer sequences:

18S rRNA(forward): 5'-GATC$_2$GTG$_3$TG$_2$TG$_2$TGC-3'

18S rRNA (reverse): 5'-A$_2$GA$_2$GT$_2$G$_5$ACGC$_2$GA-3'

GAPDH (forward): 5'-GACG$_2$C$_2$GCATCT$_2$CT$_2$GT-3'

GAPDH (reverse): 5'-CACAC$_2$GAC$_2$T$_2$CAC$_2$AT$_4$-3'

c-KIT (forward): 5'-CGTG$_2$A$_4$GAGA$_4$CAGTCA-3'

c-KIT (reverse): 5'-CAC$_2$GTGATGC$_2$AGCTAT$_2$A-3'

c-MYC (forward):5'-CTGCGACGAG$_2$AG$_2$AG$_2$ACT-3'

c-MYC (reverse): 5'-G$_2$CAGCAGCTCGA$_2$T$_3$CT$_2$-3'

BCL-2 (forward): 5'-ACA$_2$CATG$_2$C$_3$TGTG$_2$ATGAC-3'

BCL-2 (reverse): 5'-T$_2$GT$_3$G$_4$CAG$_2$CATGT$_2$-3'

The comparative cycle threshold method (C_T method) was used for relative quantification of gene expression.

Transfection and luciferase assay

K562 cells were seeded (~10^6 cells each well) in 35 mm 6 well plates. After 16 h, cells were transiently transfected with *c-KIT*, *c-MYC* and *BCL-2* promoter (Addgene, USA) luciferase reporter construct by the use of Lipofectamine 2000 (Invitrogen), as per manufacturer's instructions. Basic empty vector pGL4.72 was

employed as negative control for *c-KIT* wild promoter. pRL-TK, a HSV-thymidine kinase promoter, used as Renilla luciferase control gene (Renilla Luciferase for normalization) was employed as transfection control. After 6 h of incubation, 10% FBS was supplemented to the cells and incubated for 2 h followed by treatment with **TPW** and **TPE** at two different doses (20 µM and 40 µM). Subsequently, after 48 h of incubation, cells were lysed by 150 µl 1X cell lysis buffer (Promega) with continuous pipetting followed by vortexing for 30 secs and kept at room temperature for 10 mins. The concentration of cell lysate protein was evaluated by Lowry method. The assay was performed in triplicate using Luciferase Reporter Assay System (Promega) in a Multimode microplate reader (Molecular Devices, USA). The normalization of luciferase activity was accomplished with protein concentration and the effect of ligands upon G4 constructs were normalized against the untreated or control leukemia cells.

Then, following equation was used to calculate the ΔC_T values:

$$\Delta C_T = C_{T\ target} - C_{T\ reference} \ldots\ldots \text{(i)}$$

In our experiment, *c-KIT*, *c-MYC* and *BCL2* were the target genes and the 18s rRNA is the reference gene.

Then the $\Delta\Delta C_T$ values were calculated by:

$$\Delta\Delta C_T = \Delta C_{T test\ sample} - \Delta C_{T calibrator\ sample} \quad \ldots. \text{(ii)}$$

In our experiment, the ΔC_T values of the untreated are the calibrator samples and the ΔC_T values of the treated are test the sample.

Finally, to calculate the relative level of mRNA expression of the target genes we used the arithmetic calibrator:

$$2^{-(\Delta\Delta C_T)} \ldots\ldots\ldots \text{(iii)}$$

Western blot experiment

The untreated K562 cells as well as cells treated with **TPW** and **TPE** in doses of 20 µM and 40 µM for 24 h were lysed with RIPA buffer (150 mM NaCl, 1.0% NP-40 or 0.1% Triton X-100, 0.5% sodium deoxycholate, 0.1% SDS, 50 mM Tris-HCl, pH 8.0, Protease inhibitors). The total protein concentrations were determined using the Lowry protein estimation assay. 150 µg of protein sample was filled in each lane and alienated in an 8% SDS-PAGE gel. Electroblotting was carried out in 48 mM Tris, 39 mM glycine, 20% methanol and 0.02% SDS on a 0.22 µM polyvinyl di-fluoride (PVDF) membrane. The blot blocking was done with 3% BSA in 1X TBS, followed by washing and probing with *c-KIT*, *c-MYC*, *BCL-2* and GAPDH (endogenous loading control) antibodies overnight at room temperature. After four washes with 1X TBST, the blots were subsequently incubated with (i) 1:200 or 1: 500 dilution of ALKP (Alkaline Phosphatase) conjugated secondary antibody (for *c-KIT*, *c-MYC* and *BCL-2*) (Santacruz Life technologies), (ii) 1:3000 dilution of HRP (Horseredish Peroxidase) secondary antibody (for GAPDH)

(Santacruz Life technologies) for 2 h at room temperature. The immunoreactive bands were observed using the chemiluminescence substrate (Thermo Fisher scientific) in a Biorad chemidoc imaging system and the band intensities were quantified with ImageJ software.

Molecular docking

The optimized structure of **TPW** and **TPE** were acquired from YASARA energy minimization server and further analyzed using YASARA software.[2] Molecular docking was performed by means of the Autodock 4.0 program. Lamarckian genetic algorithm (LGA) was employed for docking calculations with default parameter settings of Autodock 4.0. The 3D coordinates of *c-KIT1*, *c-KIT2*, *c-MYC*, *BCL-2*, *h-TELO*, and *KRAS* G4 sequences were adopted from the Protein Data Bank website with the PDB codes: 4WO2, 2KYP, 1XAV, 2F8U, 1KF1 and 5I2V respectively. A maximum of 25 million energy evaluations was applied for the experiment. The results were clustered with a tolerance of 2.0 Å and 10 lowest potential energy structures were assembled from the experiment. The docked ligand-DNA complex structures were illustrated using Chimera 1.11.2 software.

Chapter 1B

Experimental unit

Melting experiments by FRET

The stock solution of 100 μM 5′-FAM (Ex. 490 nm/Em. 520 nm) and 3′-TAMRA (Ex. 555 nm/Em. 580 nm) tagged sequence was first diluted to 0.4 μM using a 60 mM sodium cacodylate (NaCaco, pH 7.4) buffer. The diluted solution was then heated to 95 °C for 1 min, cooled slowly to room temperature and kept overnight at 4°C for G4 formation. Subsequently, the DNA solution (0.2 μM) was incubated with the **TBT1**, **TBT2**, **TBT3**, **TBT4**, **TBT5** and **TBT6** (0- 10 equivalent) in same buffer at pH 7.4 for 1 h, using a blank 96-well plate (ThermoFisher Scientific) with a total volume of 100 μL for each well. In the presence of 60 mM Na^+, the labeled *MYC*Pu22 is mainly present in a quadruplex form where the FAM is in close proximity to the TAMRA showing a low FAM fluorescence due to the FRET effect. With increasing temperature, the conformation of G4 changes to a single-stranded form where the FAM is far from the TAMRA, which results in a high FAM fluorescence. Melting curves for the determination of melting temperature (T_M) were then obtained by recording FAM fluorescence with increasing temperatures from 25 to 95 °C at a rate of 0.9 °C/min using a Roche Light Cycler System. The T_M values were determined by the maximum of the first derivative

plot of the melting curves. The ΔT_M values were then plotted against concentration of ligands to determine the stabilization potential for G4.

Fluorescence spectroscopy

Fluorescence excitation and emission spectra were acquired with a HORIBA Jobin–Yvon FluoroMax-3 spectrofluorometer, in a 1 mm pathlength quartz cuvette at room temperature. Fluorescence was measured between 365 nm and 600 nm using an excitation wavelength of 350 nm in extremely degassed 60 mM Na-Caodylate buffer (pH 7.4). The titration experiments were carried out with the ligand **TBT1**, **TBT2**, **TBT3**, **TBT4**, **TBT5** and **TBT6** at 2.5 µM concentrations in presence of pre-annealed seven different DNA sequences. The specific concentration of pre-annealed DNA were added into the ligand solutions and incubated for 2 min before fluorescence was measured. The binding affinity or the apparent K_d was calculated by the Hill-1 equation using OriginPro 2016 software. The equation is as follows:

$$F = F_0 + \frac{(F_{max} - F_0)\,[DNA]}{K_d + [DNA]}$$

Where F signifies for fluorescence intensity, F_{max} for maximum fluorescence intensity, F_0 for fluorescence intensity in the absence of DNA and K_d for dissociation constant. Following DNA sequences were used for fluorescence titration:

c-MYC: 5'-d(G3GAG3TG4AG3TG4)-3'

BCL-2: 5'-d(G3CGCG3AG2A2TTG3CG3)-3'

c-KIT1: 5'-d(G3AG3CGCTG3AG2AG3)-3'

KRAS: 5'-d(AG3CG2TGTG3A2GAG3A2GAG3A2GAG5AG2)-3'

h-TELO: 5'-d(T2G3T2AG3T2AG3AT2AG3A)-3'

ds26 DNA: 5'-d(TATAGCTATA8TATAGCTATA)-3'

Cell culture

The HeLa (Cervical cancer), A549 (Lung Carcinoma), K562 (Leukemia) and NKE (normal kidney epithelial) cell lines were originally obtained from the National Centre for Cell Science (NCCs, Pune) and grown in DMEM (Gibco, USA), DMEM:F12K (1:1), RPMI 1640 (Gibco, USA) supplemented with 10% fetal bovine serum (Gibco, USA). Cells were incubated for 24 hrs. at 37 °C with 5% CO_2.

Cell growth inhibition assay

To proceed for biological studies, it was crucial to first carry out XTT (2, 3-bis-(2-methoxy-4-nitro-5-sulfophenyl)-2H-tetrazolium-5-carboxanilide) assay to determine the cytotoxicity of the compounds in different cancer and normal cell lines. Growth inhibition experiments were performed in triplicate on 96-well plates from lower (submicromolar) to higher (submilimolar) doses. Cells were grown (~10^5 cells/well) in 100 µL of culture medium and treated with increasing

concentration of the compounds (0 − 200 μM) followed by incubation for 24 hours. The XTT/phenazine methosulfate (PMS) reagent was prepared by mixing 1 mg of XTT in 1 mL of culture medium with subsequent addition of 2.5 μL of 10 mM PMS solution [in phosphate-buffered saline (PBS)]. This freshly prepared mixture (25 μL) was then directly added to each well and incubated for 2 h at 37 °C. The absorbance of XTT formazan was read at 450 nm on a Multiskan FC microplate spectrophotometer (Thermo Scientific). The calculation of cell viability percentage was done using the following equation:

% of cell viability = (OD of treated cells/OD of untreated control cells) x 100

Confocal Microscopy

Cellular localization of compound **TBT1** fluorescence based cell imaging experiments. MCF-7 cells were seeded on glass cover slips placed in 6-well cell culture plates for 24 h followed by incubation with compound **TBT1** (2 μM) for 2 h in CO_2 (5%) incubator at 37 °C. After incubation, cells were washed with PBS buffer three times and the cover slips were mounted on glass slides using NucRed (1:1 solution in PBS) and localization of compound **TBT1** was viewed under Zeiss LSM-800 Confocal Laser Scanning Microscope. At least five fields per slide and three independent sets were examined.

Chapter 2

Experimental unit

Melting experiments by FRET

The stock solution of 5′-FAM (Ex. 490 nm/Em. 520 nm) and 3′-TAMRA (Ex. 555 nm/Em. 580 nm) labeled RNA oligo sequences were first diluted to 0.4 μM using a 100 mM Tris-KCl buffer (pH 7.4). The diluted solution was then heated to 95 °C for 1 min, cooled slowly to room temperature and kept overnight at 4°C. Subsequently, the RNA solution (0.2 μM) was incubated with the **RD1 RD2 RD3 RD4 RD5** (0 - 10 equivalent) in 100 mM Tris-KCl buffer (pH 7.4) for 1 h, using a blank 96-well plate (Axygen, USA) with a total volume of 100 μL for each well. In the presence of 100 mM K^+, the labeled G4 forming sequence is mainly present in a quadruplex form where the FAM and TAMRA are in close proximity and show a low FAM fluorescence due to the FRET. With increasing temperature, the conformation of G4 changes to a single-stranded form where the FAM is far from the TAMRA, which results in a high FAM fluorescence. Melting curves for the determination of melting temperature (T_M) were then obtained by recording FAM fluorescence with increasing temperatures from 37 to 95 °C at the rate of 0.9 °C/min using Roche Light Cycler II. The T_M values were analyzed and plotted against the concentration of ligands to determine the stabilization potential for G4s using OriginPro 2016 software.

Fluorescence measurements

Fluorescence excitation and emission spectra were acquired with a HORIBA Jobin–Yvon Fluorolog spectrofluorometer, in a 1 mm path-length quartz cuvette at room temperature. Fluorescence of peptidomimetics was measured between 300 nm and 550 nm using the same excitation wavelength of 290 nm in extremely degassed 100 mM Tris-KCl buffer (pH 7.4). The titration experiments were carried out with the ligands at 2.5 µM concentration in presence of RNA G4s: *RG-1*, *RG-2*, *RG-3* and *dsDNA*. The specific concentrations of pre-annealed RNA G4s were gradually added into the solutions of **RD1**, **RD2**, **RD3**, **RD4** and **RD5** followed by the incubation for 2 mins before the fluorescence measurement. The binding affinity or the apparent K_d was calculated by the Hill-1 equation using OriginPro 2016 software. The equation is as follows:

$$F = F_0 + \frac{(F_{max} - F_0)\,[DNA]}{K_d + [DNA]}$$

Where F signifies for fluorescence intensity, F_{max} for maximum fluorescence intensity, F_0 for fluorescence intensity in the absence of RNA or DNA and K_d for dissociation constant. Following RNA and *dsDNA* sequences were used for fluorescence titration:

RG1 *- 5'- GGCUGGCAAUGGCGG- 3'*

RG2 *- 5'- GGUAUGUGGAAAGGUUAUGG -3'*

RG3 *- 5'- GGCUUAUAGGUUUAAUGGUAUUGG -3'*

dsDNA *- 5'- $CA_2TCG_2ATCGA_2T_2CGATC_2GAT_2G$ - 3'*

Isothermal calorimetry

Calorimetric titrations were carried out in a MicroCal PEAQ-ITC system (Malvern). The RNA samples (5 μM in 100 mM Tris-KCl buffer, pH 7.4) were pre-annealed via heating at 95 °C for 5 min followed by gradual cooling to room temperature (0.1 °C /min) and incubated overnight at 4 °C. Experiments were performed by overfilling the pre-annealed *RG-1*, *RG-2*, *RG-3* and *dsDNA* samples (5 μM) in 300 μL sample cell followed by titration with duly prepared 50 μM ligand solution over 20 injections at an interval of 150 secs. The temperature of the reference and sample cells was retained at 25 °C during the experiment with a differential power of 10 μcal.sec^{-1} and the continuous stirring of sample cell solution at a speed of 750 rpm. Samples were extensively degassed immediately before use.

The raw data were analyzed by Malvern ITC Analysis software provided with the instrument. The data fitting was done using an appropriate binding model. The dissociation constant (K_d), Gibb's free energy change (ΔG), enthalpy of reaction (ΔH) and entropy (ΔS) change were calculated using the following equation:

$$\Delta G = \Delta H - T\Delta S$$

Chapter 3A

Experimental unit

Ion transport study by fluorescence spectroscopy

Large unilamellar vesicles preparation

Large unilamellar vesicles (LUVs) were formed using a 200 μL 9:1 mixture of 10 mM EYPC (L-α-Phosphatidylcholine egg yolk) and cholesterol in chloroform. After solvent removal and vacuum drying, the resulting thin film was hydrated with 500 μL of buffer (10 mM HEPES, 100 mM NaCl or KCl, pH 6.4) containing 100 μM HPTS (8-hydroxypyrene-1,3,6- trisulfonic acid trisodium salt). Next, the suspension was subjected to six freeze–thaw cycles (liquid nitrogen/water at room temperature) during hydration. The resulting white suspension was then extruded 19 times through a 100 nm polycarbonate membrane to obtain large unilamellar vesicles (LUVs) with an average diameter of ~ 60 nm (as measured by DLS method). The LUVs suspension was separated from extravesicular HPTS dye by using size-exclusion chromatography (Econo-Pac 10DG column, Bio-rad; mobile phase: 10 mM HEPES, 100 mM NaCl or KCl, pH 6.4) and diluted with mobile phase for the desired working concentration.

Monitoring ion transport by HPTS assay

To a EYPC· LUVMs⊃ HPTS suspension ([EYPC] = 10 mM, [HPTS] = 100 μM) in 10 mM HEPES buffer containing 100 mM KCl (490 μL, pH 6.4) was added an

aqueous solution of NaOH (0.5 M, 5 μL, ΔpH = 1) by a syringe in the dark at 20 °C. Fluorescence intensity of HPTS at 510 nm upon excitation with 460 nm-light was monitored as a function of time until the addition of 1.0 wt% Triton X-100 (40 μL) at 450 s. Relative fluorescence intensity of HPTS was evaluated by the equation of

$$I = \frac{I_t - I_0}{I_{Lysed} - I_0}$$

Where I_0 and I_t represent the initial, final and I_{lysed} represent the fluorescence intensities before addition of NaOH, after addition of NaOH and 1 wt% Triton X as lysis buffer, respectively.

Preparation of carboxyfluorescein (CF) encapsulated vesicles

Liposomes were prepared by using the extrusion procedure. Lipid films were prepared from a mixture of 10 μL of 10 mM egg yolk L-α-phosphatidylcholine (EYPC) and cholesterol (9:1) in chloroform by drying in vacuum for ~ 16 hrs. The film was hydrated with carboxyfluorescein (0.5 mL, 40 mM) in HEPES buffer (10 mM HEPES 100 mM KCl/NaCl pH 7.4). The mixture was then resuspended to form vesicles followed by vortexing. The unilamellar vesicles were extruded through a polycarbonate membrane with a pore diameter of ~1 μm. Free dye was removed by column chromatography using a Sephadex G25 column.

CF release experiments

The carboxyfluorescein release assay was carried out via the formation of CF encapsulated LUVs. Carboxyfluorescein was encapsulated in large unilamellar vesicles (LUV) prepared from EYPC/cholesterol (9:1) under self-quenching conditions (0.5 mL, 40 mM carboxyfluorescein). **TBP1** or **TBP2** (20 μM) in DMSO was added and mixed with the LUVs in HEPES NaCl buffer (final volume 500 μL). The time resolved fluorescence intensity (Horiba Jobin Yvon Fluoromax 3 instrument) was monitored at 25 °C at 520 nm (λ_{ex} = 480 nm). Total dye release was determined by disruption of the LUVs by the addition of Triton X-100 (40 mM). The percentage of CF release caused by ligands was determined by using the following equation:

$$Leakage\ (\%) = (F_t - F_0)(F_{100} - F_0) \times 100$$

Where, F_t is the time dependent fluorescence intensity and F_0 and F_{100} are fluorescence intensities observed in the absence of **TBP1** and **TBP2** and after Triton X-100 treatment, respectively.

Formation of giant unilamellar vesicles (GUVs)

GUVs were prepared by electroformation technique (Vesi Prep Pro, Nanion, Germany). 10 μL of a 10 mM solution of EYPC and cholesterol (9:1) in chloroform was spread evenly on the indium tin oxide (ITO) coated glass slides within the "O" ring area. The solvent was evaporated at room temperature and the

slides were dried overnight under vacuum. Then, ITO slides were assembled in the Vesi Prep Pro and filled with 275 μL of sorbitol solution (1 M). A sinusoidal AC field of 3 V and 5 Hz was applied for 2 h at 25 °C temperature. The prepared GUV solution was collected and subjected to patch-clamp experiments.

Confocal imaging in GUVs

GUVs were suspended in 10 mM HEPES, 100 mM KCl or 100 mM NaCl (pH 7.4) buffer and incubated with **TBP2** (20 μM) and Nile red (Sigma, USA) for 5 minutes. After incubation, the mixture was placed on the fluodish and observed under Confocal Microscope (Zeiss, Germany). For control slides, GUVs were incubated with either **TBP2** or Nile red. At least 4 fields per slide and three independent sets were examined. The images obtained were processed using ImageJ software.

Conductance measurements by patch-clamp technique

Conductance measurements were carried out using the Port-a-Patch setup (Nanion, Munich, Germany). First, a borosilicate glass chip (NPC chip, Nanion, Germany) with 3-5 mΩ was loaded with symmetrical working buffer containing 1 M KCl, and 10 mM HEPES (pH 7.0) in both *cis* and *trans* compartments and Ag/AgCl electrodes were placed on both sides of the NPC chip. Next, bilayer membrane with >1 Giga Ohm resistance was constructed across the micrometer-sized aperture in the NPC chip by adding GUV suspension and applying a mild negative pressure

(-10 mbar). **TBP2** (20 μM) was added to the *cis*-side of the chamber. Current traces were recorded using an HEKA EPC 10 patch clamp amplifier with a built-in 1 kHz 4 pole Bessel low-pass filter and a Digidata 1322A digitizer. I-V curve was generated using a voltage ramp from -80 mV to +80 mV. Data analysis was performed using Clampfit 10.2 software.

UV absorption spectroscopy

UV measurements were carried out on a JASCO UV/Vis/NIR spectrophotometer at 25 °C in a thermo stated cell holder using a quartz cuvette with a 1 cm path-length. The absorption spectrum of **TBP1** and **TBP2** (10 μM) was recorded in 10 mM HEPES, 100 mM KCl or NaCl, pH 7.4.

Melting experiments by FRET

The stock solution of 100 μM 5′-FAM (Ex. 490 nm/Em. 520 nm) and 3′-TAMRA (Ex. 555 nm/Em. 580 nm) tagged DNA sequences were first diluted to 0.4 μM using a 60 mM potassium cacodylate (KCaco, pH 7.4) buffer. The diluted dual labeled oligonucleotides were annealed by heating to 95 °C for 1 min, then cooled slowly to room temperature and kept overnight at 4 °C. Subsequently, the DNAs (0.2 μM) were incubated with **TBP1** or **TBP2** (0 - 10 equivalent) in the same buffer at pH 7.4 for 1 h, using a blank 96-well plate (ThermoFisher Scientific) with a total volume of 100 μl for each well. In the presence of 60 mM K^+, the G4 DNA sequences mainly adopt a quadruplex structure in which the donor fluorophore

FAM is in close proximity to the acceptor probe TAMRA resulting in a low FAM fluorescence due to the FRET effect. With increasing temperature, the conformation of G4 changes to a single-stranded form where the FAM is far from the TAMRA, which results in a high FAM fluorescence. Melting curves were then obtained by recording FAM fluorescence with increasing temperatures from 25 to 95 °C at a rate of 0.9 °C/min using Roche Light Cycler System 480II. The melting temperature (T_M)) values were determined by the maximum of the first derivative plot of the melting curves. The ΔT_M values were then plotted against the concentration of ligands to determine the stabilization potential for G4.

Fluorescence spectroscopy

Fluorescence excitation and emission spectra were acquired with a HORIBA Jobin–Yvon Fluorolog spectrofluorometer, in a 1 mm path length quartz cuvette at room temperature. Fluorescence of **TBP1** and **TBP2** was measured between 340 nm and 550 nm using the same excitation wavelength of 330 nm in degassed 60 mM KCaco buffer (pH 7.4). The titration experiments were carried out with the ligand **TBP1** and **TBP2** at 2.5 μM concentration in the presence of pre-annealed quadruplexes and *ds26* or *dsDNA*. The specific concentrations of pre-annealed DNAs were added into the **TBP1** or **TBP2** solutions and incubated for 2 min before fluorescence measurement. The binding affinity or the apparent K_d was

calculated by the Hill-1 equation using OriginPro 2016 software. The equation is as follows:

$$F = F_0 + \frac{(F_{max} - F_0)\,[DNA]}{K_d + [DNA]}$$

Where F signifies for fluorescence intensity, F_{max} for maximum fluorescence intensity, F_0 for fluorescence intensity in the absence of DNA and K_d for dissociation constant. Following DNA sequences were used for fluorescence titration:

c-MYC22: 5'-d(G3GAG3TG4AG3TG4)-3'

BCL-2: 5'-d(G3CGCG3AG2A2TTG3CG3)-3'

c-KIT1: 5'-d(G3AG3CGCTG3AG2AG3)-3'

c-KIT2: 5'-d(G3CG3CGCTAG3AG4)-3'

h-TELO: 5'-d(T2G3T2AG3T2AG3AT2AG3A)-3'

ds26 DNA: 5'-d(CA2TCG2ATCGA2T2CGATC2GAT2G)-3'

Chapter 3B

Experimental unit

Large Unilamellar Vesicles Preparation

Large unilamellar vesicles (LUVs) were created using a 200 µL 9:1 mixture of 10 mM EYPC (L-α-Phosphatidylcholine) and cholesterol in chloroform. After solvent removal and vacuum drying, the resulting thin film was hydrated with 500 µL of buffer (10 mM HEPES, 100 mM NaCl or KCl, pH 6.4) containing 100 µM HPTS (8-hydroxypyrene-1,3,6- trisulfonic acid trisodium salt). Next, the suspension was subjected to six freeze–thaw cycles (liquid nitrogen/water at room temperature) during hydration. The resulting white suspension was then extruded 19 times through a 100 nm polycarbonate membrane to obtain large unilamellar vesicles (LUVs) with an average diameter of ~100 nm. The LUVs suspension was separated from extravesicular HPTS dye by using size-exclusion chromatography (Econo-Pac 10DG column, Bio-rad; mobile phase: 10mM HEPES, 100mM NaCl or KCl, pH 6.4) and diluted with mobile phase to desired working concentration.

Giant Unilamellar Vesicles Preparation

GUVs were prepared by electroformation technique (Vesi Prep Pro, Nanion, Germany). 10 µL of a 10 mM solution of EYPC and cholesterol (9:1) in chloroform was spread evenly on the indium tin oxide (ITO) coated glass slides

within the “O” ring area. The solvent was evaporated at room temperature and the slides were dried overnight under vacuum. Then, ITO slides were assembled in the Vesi Prep Pro and filled with 275 µL of sorbitol solution (1 M). A sinusoidal AC field of 3 V and 5 Hz was applied for 2 h at 25 °C temperature. The GUV solution was collected and stored at 4 °C.

HPTS assay

To a EYPC·1 LUVMs⊃HPTS or EYPC·2 LUVMs⊃HPTS suspension ([DOPC] = 0.20 mM, [HPTS] = 100 µM) in 10 mM HEPES buffer containing 100 mM KCl (490 µL, pH 6.4) was added an aqueous solution of NaOH (0.5M, 5 µL, ΔpH = 0.8) by a syringe in the dark at 20 °C. Fluorescence intensity of HPTS at 510 nm upon excitation with 460 nm-light was monitored as a function of time until the addition of 1.0 wt% Triton X-100 (40 µL) at 450 s. Relative fluorescence intensity of HPTS in response to the pH enhancement was evaluated by the equation of

$$I = \frac{I_t - I_0}{I_{Lysed} - I_0}$$

Where I_0 and I_t represent the initial, final and I_{lysed} represent the fluorescence intensities before addition of NaOH, after addition of NaOH and 1 wt% Triton X as lysis buffer respectively.

Preparation of carboxyfluorescein encapsulated vesicles

Liposomes were prepared by using the extrusion procedure. Lipid films were prepared from a mixture of 10 μL of 10 mM L-α-Phosphatidylcholine egg yolk (EYPC) and cholesterol (9:1) in chloroform by drying in vacuum for ~16 hrs. The film was hydrated with carboxyfluorescein (0.5 mL, 40 mM) in HEPES buffer (10mM HEPES 100mM KCl/NaCl pH 7.4). The mixture was then resuspended to form vesicles followed by vortexing. Multilamellar vesicles were extruded through a polycarbonate membrane with a nominal pore diameter of 1 μm. Free dye was removed by column chromatography using a Sephadex G25 column.

CF release assay

The Carboxyfluorescein (CF) release assay was carried out via CF encapsulated in LUVs. Carboxyfluorescein was encapsulated in large unilamellar vesicles (LUV) prepared from EYPC/cholesterol (9:1) under self-quenching conditions (0.5 mL, 40 mM carboxyfluorescein). **F4** or **F7** was added and mixed with the LUVs in PBS (final volume 500 μL). The time resolved fluorescence intensity (Horiba Jobin Yvon Fluorlog instrument) was monitored at 25 °C at 520 nm (λ_{ex} = 480 nm). Total dye release was determined by disruption of the LUVs by the addition of Triton X-100 (40 mM). The percentage of CF release caused by XX was determined by using the following equation:

$$Leakage\ (\%) = (F_t - F_0)(F_{100} - F_0) \times 100,$$

where F_t is the time dependent fluorescence intensity and F_0 and F_{100} are fluorescence intensities observed in the absence of **F4** and **F7** and after Triton X-100 treatment, respectively.

Fluorescence titration study

Fluorescence titrations were carried out on Horiba Jobin Yvon Fluorolog instrument at 25 °C in a quartz cuvette (path-length 1 mm) with subsequent addition of LUVs in HEPES NaCl or HEPES KCl buffer (pH 7.4). **F4** or **F7** were dissolved in the same buffer to obtain the concentration of 10 µM from 10 mM stock solution (DMSO). Both the ligands were excited at 325 nm wavelength and the emission spectra were recorded from 350 nm - 550 nm. The Hill 1 equation was used to calculate the binding constants in OriginPro 2016.

$$F = F_0 + \frac{(F_{max} - F_0)[DNA]}{K_d + [DNA]}$$

Where F denotes fluorescence intensity, F_{max} for maximum fluorescence, F_0 for fluorescence in the absence of DNA and K_d indicates dissociation constant.

Dye influx assay

A droplet of EYPC solution (5 µL, 10 mg/mL in chloroform) was added onto an ITO glass slide. Within 5 minutes the solvent evaporated and a dried thin lipid film was formed. The glass slide was then inserted in a vesicle prep-pro device

(Nanion). An O-ring was added around the patch. 1X Sorbitol solution (300 μL, 1 M in water) was added to the lipid film patches confined by the O-ring. Finally, another ITO glass slide was applied from the top, resulting in a sealed chamber. An alternating electric field was applied between the two slides according to the following protocol: 3 V, 5 Hz for 120 minutes. The solution was collected and stored at 4 degrees. To prepare imaging samples, 10 μL of the GUV solution was mixed with 500 μL buffer solution (0.5x TAE and 500 mM NaCl) in a fluorodish. The dyes were then added: 20 μM Atto633. The solution was mixed gently with the pipette tip and the dish was transferred onto a confocal microscope (Zeiss, LSM800) equipped with two laser sources: 488 nm and 633 nm. A brief check of the morphology of the GUV sample was done using transmitted light to confirm that the GUVs were formed properly. **F7** or **F4** were added (10 μL, 1 μM) to the above solution and mixed gently. Observation was started after 7 minutes in which the GUVs were allowed to sink down for observation and the structures to bind to the GUVs. The fluorescence intensity of dye inside the vesicles was analyzed using FIJI ImageJ software.

Preparation of Droplet Interface Bilayers (DIBs)

A homogenous hydrogel layer was formed on a O_2 plasma treated clean glass coverslip by spin-coating an excess volume of an aqueous solution of low melting point substrate agarose (0.75%, 90 degrees, 4000 rpm, 30 s). Subsequently, 29 μL

solution of DPhPC, dissolved in chloroform (50 mg/ml), was transferred to a 1 mL glass vial to evaporate the solvent and form a solvent free lipid film under nitrogen stream. After 30-35 minutes, following the addition of 150 µL of silicon/hexadecane, the lipid suspension was sonicated for 5 min to produce a solution of DPhPC in silicon/hexadecane with a final concentration of 9.5 mg/ml. The prepared coverslip was incorporated into the PMMA poly(methyl methacrylate) device, into which buffered agarose solution was injected (4.3% low melting point agarose in 10 mM HEPES 20 µM EDTA, 1M $CaCl_2$ pH 7.0, making contact with the agarose-coated coverslip maintaining hydration and ionic content of the hydrogel bilayer support. Each well of the array of the assembled device was filled with hexadecane. 0.2 µL aqueous droplets (10 mM HEPES, 333 µM EDTA, 1 M KCl, 0.25 mM Fluo-8, pH 7) were prepared by incorporating **F4** or **F7** (0.5 – 50 µM) and injected into micro-wells containing 9.5 mg/ml^{-1} DPhPC in hexadecane. Droplets were incubated for 20 minutes to ensure self-assembly of a lipid monolayer at the aqueous hexadecane interface; droplets were then transferred by pipette into individual wells of the bilayer array device. Droplet Interface Bilayers were instantly formed after addition into the wells.

Fluorescence Imaging via TIRF microscopy

The DIBs were imaged via Total Internal Reflection Fluorescence (TIRF) microscopy with an inverted microscope with oil immersion objective (60x Plan

Apo N.A. 1.4, TE-2000, Nikon Instruments). The Fluo-8H dye in the droplet was excited using a 473 nm laser (Shanghai Dream Lasers Technology Co.) beam. The emitted fluorescence was collected by the objective and transmitted through a dichroic mirror (500 DRLP, Omega Optical) and 525/50 nm band-pass filter (Omega optical), before being imaged on a frame-transfer electron-multiplying charge-coupled device (iXon+, Andor Technology, 128 × 128 pixels).

Summary

Chapter 1

Chapter 1A illuminates a G4 sensing small molecule **TPW** selectively binds *c-KIT1* G4 with ~ 1:1 stoichiometry and downregulates *c-KIT* proto-oncogene expression in cancer cells. The thiazole based polyamide with a pyridine unit targets nuclei structures and emit high fluorescence inside the cell nuclei followed by interaction with G4 structures in cancer cells. Thus a promising polyamide probe has been developed to specifically recognize G-quadruplex structures with the ability to specifically alter *c-KIT* oncogene expression.

Chapter 1B demonstrates that anthracene conjugated thiazolyl peptidomimetic, **TBT1** preferentially binds to *c-MYC* G-quadruplex (G4) with high G4 stabilizing potential (ΔT_M ~18.3 $^{\circ}$C) to repress *c-MYC* expression in breast cancer cells. **TBT1** can efficiently invade the cell membrane as well as colocalizes with the nucleus staining dye, NucRed inside the cellular nuclei. Intriguingly, **TBT1** could induce the cell death with the IC_{50} value of 3.7 μM in breast cancer cells (MCF-7) while it does not possess comparable toxicity to normal kidney epithelial cells. G4 based luciferase reporter assay further confirms that **TBT1** can successfully interact with the *c-MYC* promoter region to reduce the *c-MYC*

expression in MCF-7 cells. Development of such cytotoxic fluorescent peptidomimetic could show new avenues to explore future possible theranostics for cancer.

Chapter 2

Chapter 2 explains that SARS-CoV-2 (COVID-19) genome possess G-rich RNA secondary structures known as *RG-1, RG-2, RG-3* which could be a potential therapeutic target against COVID-19. We have developed a coumarin conjugated peptidomimetic ligand **RD5** that specifically interacts with SARS-CoV-2 RNA quadruplex over duplex DNA with high stabilization potential for *RG-2* (ΔT_M = 23.7±1.2 °C). The FRET analysis elucidates that the molecule **RD5** possesses the highest stabilization potential for the *RG-2* G4s (ΔT_M = 23.7±1.2 °C) over other SARS-CoV G4 structures like *RG-1, RG-3* and duplex DNA. The fluorescence spectroscopic studies illustrate that **RD5** preferentially binds to the *RG-2* (K_d = 1±0.05 μM) with high affinity compared to *RG1, RG-3* and *dsDNA*. **RD5** interacts with the *RG-2* with highest potential binding energy (ΔG = ~ -8 kcal/mol) and 1:1 stoichiometry as indicated in calorimetric data. Overall, the study suggests that the peptidomimetic ligand **RD5** harbors the unique feature to be able to specifically interact with COVID-19 quadruplex *RG-2*. We predict that the ligand could inhibit the replication of SARS-CoV-2 via the stabilization of G-quadruplex which will be further studied in near future.

Chapter 3

In *chapter 3A*, construction of an artificial ion channel with G4 specific thiazole based peptidomimetic **TBP2** has been described which enables the transportation of Na^+ and K^+ via model lipid bilayer membrane with high ionic conductance (~0.6 nS). **TBP2** can form nanovesicular structures (r ~50 nm) along with nanofibres as shown in transmission electron microscopy imaging. Biophysical assays (e.g., FRET, fluorescence, NMR) illustrate that **TBP2** preferentially binds to *c-MYC22* G4 with high affinity (K_d = *~1.6* µM) over other G4s and *ds26* DNA with 1:1 stoichiometry. **TBP2** exhibits potent toxicity towards cancer cells with *c-MYC* promoter G4 as demonstrated in luciferase reporter assay. However, **TBP2** can also be used as a fluorescent probe due to its excellent fluorescence enhancement property both in the cellular nuclei and the cell membrane. Thus, we report a *c-MYC* G4 selective cytotoxic thiazolyl peptidomimetic for the first time to act as a synthetic ion channel in an in-vitro model system.

In *chapter 3B*, the folate derivatives **F7** and **F4** can act as cation (Na^+ and K^+) transporting highly conductive (~ 6 nS) transmembrane nanopore in cell membrane mimicking artificial lipid bilayer. **F7** and **F4** have been found to construct self-assembled nanostructure enabling transportation of ions via the lipid membrane. The fluorescence titration and confocal microscopy have revealed that

F7 and **F4** can efficiently bind to the vesicular membrane and co-localizes with membrane staining dye nile red. The permeation of Atto633 dye via GUV membrane indicates that the long hydrophobic chain in **F7** plays crucial role in the formation of large porous structure (~ 4.8 nm) which allow the influx of Atto 633 dye (~1 nm) inside the GUVs. The high conductance rate indicates that both **F7** and **F4** could form large porous structure due to self-assembly of folic acid-anthracene conjugate (**F7**) and folic acid-guanosine conjugate (**F4**) with long hydrophobic chain linker.

Future Outlook

- The development of such G4 selective small molecule could play a significant role as substitutes to non-specific DNA binding small molecules, often claimed to be used for cancer theranostics. Altogether, the outcomes may provide insights into the designing of new anticancer molecules with preferential affinity for the DNA G4-structures which in-turn may ease the off-target toxicity and increase bioavailability and also might help to escape the drug resistance property of cancer cells.
- Development of RNA quadruplex specific peptidomimetic would further inspire and propagate the design and synthesis of new peptidomimetic synthetic molecules to target the SARS-CoV-2 RNA secondary structures towards the development of antiviral therapeutics and biomolecular devices against the ongoing COVID-19 pandemic in pharmaceutical sectors.
- The small molecule ion transporters would provide critical structural and functional aspects of artificial ion channels and open a new paradigm for developing novel synthetic ion transporters with improved chemotherapeutic or drug like properties. Apart from that, design of biomimetic small molecules could provide insights into transmembrane nanopore towards development of drug delivery tools, biomolecular devices, and diagnostics.

Chemistry–A European Journal
Full Paper
doi.org/10.1002/chem.202100907

Special Collection

G4 Sensing Pyridyl-Thiazole Polyamide Represses *c-KIT* Expression in Leukemia Cells

Raj Paul,[a] Debasish Dutta,[a] Tania Das,[a] Manish Debnath,[a] and Jyotirmayee Dash*[a]

Abstract: Specific sensing and functional tuning of nucleic acid secondary structures remain less explored to date. Herein, we report a thiazole polyamide **TPW** that binds specifically to *c-KIT1* G-quadruplex (G4) with sub-micromolar affinity and ~1:1 stoichiometry and represses *c-KIT* proto-oncogene expression. **TPW** shows up to 10-fold increase in fluorescence upon binding with *c-KIT1* G4, but shows weak or no quantifiable binding to other G4s and *ds26 DNA*. **TPW** can increase the number of G4-specific antibody (BG4) foci and mark G4 structures in cancer cells. Cell-based assays reveal that **TPW** can efficiently repress *c-KIT* expression in leukemia cells via a G4-dependent process. Thus, the polyamide can serve as a promising probe for G-quadruplex recognition with the ability to specifically alter *c-KIT* oncogene expression.

Introduction

The development of small molecule ligands that selectively recognize genomic structures and modulate their stability is one of the fundamental approaches of chemical biology.[1] Besides the storage of genetic information, the regulation of gene expression is a key function of nucleic acids.[2a] Therefore, specific recognition of a gene is pivotal to selectively regulate its expression inside cells.[2b] Owing to the occurrence of G-quadruplexes (G4s) in oncogenic promoters (e.g., *c-KIT, c-MYC, BCL-2, KRAS)* and telomeres; targeting these structures has become an elegant approach for cancer therapeutics and diagnostics.[2–5] G4s adopt four-stranded stacked guanine quartets construct in the presence of monovalent cations (e.g., Na^+, K^+). The distinctive structural morphology and promising biological role make the G4s smart targets for the design of synthetic ligands.[6] Owing to globular structures of G4s with large planes, they can be targeted with high selectivity in contrary to single-stranded and duplex DNAs having linear structures.[7,8]

In the last two decades, a variety of small molecule ligands have been reported as G4 binding compounds that down-regulate mRNA and protein expression of oncogenes.[8,9] Notably, most of the reported compounds exhibit promiscuous cross reactivity and cytotoxicity; thus they might not be suitable for selective recognition and regulation of oncogenes. However, a few ligands like thiazole orange analogues, BMVC (3,6-bis(1-methyl-4-vinylpyridinium)carbazolediiodide), IMT (a benzothiazole derivative), N-TASQ have been studied to act as fluorescent light-up molecular probe for G4 detection in cancer cells.[9c] Probing quadruplex selective ligands towards cancer therapeutics and diagnostics[9c] is still a challenging objective currently. Considering the putative biological importance of quadruplexes, it is a worthy goal to develop and exploit quadruplex specific ligands as tools for potential therapies as well as to examine and understand G4-related biological mechanisms.[10,11] Herein, we delineate a potential G4 binder, which specifically recognizes quadruplex and attenuate the *c-KIT* proto-oncogene expression without influencing the morphological properties of cells.

c-KIT codifies a type-III RTK (receptor tyrosine kinase) for stem cell factor (SCF), which is a key to cell proliferation, migration, maturation and survival in different cancer types.[12] The overexpression of *c-KIT* is observed in various malignant cancers like myeloid leukemia (due to kinase mutation causing *c-KIT* protein auto phosphorylation), pancreatic cancers, Gastric Intestinal Stromal Tumors (GIST), colorectal cancers etc.[13] In particular, identification of novel antileukemic agents and markers became a challenge due to the non-adherent and drug resistance property of leukemia cells.[14] Imatinib is the only clinically approved chemotherapeutic drug which acts through preserving the bcr-abl kinase in an inert state to treat chronic myeloid leukemia (CML).[15] However, due to high mutation rate in bcr-abl kinase, imatinib resistance and its adverse effects are so common in patients with CML. Though some second generation inhibitors have been developed to circumvent the challenge, mitigating *c-KIT* oncogene expression via small molecules is considered as an effective way for the treatment of CML.[14,15] The *c-KIT* promoter comprises three neighboring regions capable of folding into parallel G4 structures: *c-KIT1*, *c-KIT** (a G-rich Sp1 binding site) and *c-KIT2* which are positioned between −109 and −182 nucleotides upstream of the ATG start site. Experimental evidence as well as theoretical studies indicate that *c-KIT1* G4 possesses parallel topology wherein one non-G-tract guanine takes part in the center of stacked G-quartets. It is noteworthy to state that the *KIT1* G4 has a strong influence on biological role of the whole promoter.[16,17] To date,

[a] *R. Paul, Dr. D. Dutta, Dr. T. Das, Dr. M. Debnath, Prof. Dr. J. Dash*
School of Chemical Sciences
Indian Association for the Cultivation of Science
Kolkata 700032 (India)
E-mail: ocjd@iacs.res.in
Homepage: http://iacs.res.in/faculty-profile.html?id=98

Supporting information for this article is available on the WWW under https://doi.org/10.1002/chem.202100907

This manuscript is part of an Indo-German special collection.

Organic & Biomolecular Chemistry

ROYAL SOCIETY OF CHEMISTRY

COMMUNICATION

View Article Online
View Journal | View Issue

Cite this: *Org. Biomol. Chem.*, 2021, **19**, 1965

Received 6th January 2021,
Accepted 9th February 2021

DOI: 10.1039/d1ob00248a

rsc.li/obc

A DNA nanosensor for monitoring ligand-induced i-motif formation†

Puja Saha, Deepanjan Panda, Raj Paul and Jyotirmayee Dash *

Herein, we present a gold nanoparticle (GNP)-based DNA nanosensor to detect the formation of an i-motif from the random coil structure by small molecules at physiological pH. The nanosensor shows a distance dependent fluorescence turn-off response in the presence of a ligand, indicating conformational changes from the C-rich single stranded DNA into an i-motif.

i-Motifs are interspersed tetrahelical DNA secondary structures that are stabilized by hemi-protonated and intercalated cytosine base pairs ($C:C^+$).[1–4] The *in vitro* stability of i-motifs strongly depends on chemical and physical environmental factors such as acidic pH, low ionic strength, molecular crowding, low temperature, *etc.*[1–4] These conditions are not available in cellular environment to stabilize i-motif structures. Thus, the existence of i-motifs within genomic DNA is still a matter of scientific debate. Recent studies show that i-motifs are stable and they exist in the nuclei of living human cells.[5–7] These findings suggest that i-motifs could be potential targets for gene regulations. The non-canonical DNA i-motifs are also hypothesized to be involved in several cancer-related processes.[8,9] In this regard, ligands that preferentially target and induce the i-motif formation in genomic DNA in the cellular environment would be useful in i-motif-targeted anti-cancer therapeutics. Such ligands[10–16] would also provide detailed insights into the potential impact of i-motif structures on physiological processes. Thus a simple and fast high-throughput screening method can be used to identify i-motif inducing ligands at physiological pH.

Circular Dichroism, ^{1}H NMR spectroscopy and FRET-based techniques (like FRET-based DNA melting assay, smFRET, *etc.*)[10–16] are currently used as standard methods to detect ligand mediated i-motif formation and stabilization. However, NMR and CD spectroscopy techniques are time-consuming, have low throughput and require precise control of experimental setups. FRET based assays are generally used to detect i-motif stabilization under acidic conditions. In comparison to these traditional detection methods, gold nanoparticle (GNP)-based nanosensors are extremely attractive because of the ease of detection, minimal interference, high sensitivity and potential for high-throughput analysis.

GNP-based sensors are of particular interest due to the unique features of gold nanomaterials such as distinct optical and physicochemical properties, controllable size, ease of synthesis and versatile surface chemistry that allow multifunctionalization with a wide range of organic or biological molecules.[17–23] Each of these attributes of GNPs enables researchers to develop novel cost effective probes for the selective binding and detection of small molecules and biological targets.[17–27] We herein report the design and fabrication of a high throughput GNP-based DNA sensor for the identification of i-motif inducing ligands. To our knowledge, GNP-based sensors have not been reported so far to detect induction of the i-motif structure at physiological pH.

In this study, the GNP-based DNA probe was devised by grafting random coil cytosine-rich DNA sequences onto the surface of water-soluble gold nanoparticles (GNPs) *via* thiol–gold covalent bonds (Fig. 1). We have used a 5′-thiolated C-rich

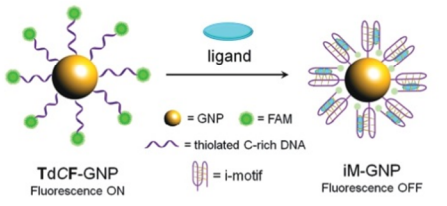

TdCF: 5′-ThiC6-$TC_4AC_2T_2C_4AC_3TC_4AC_3TC_4A$-FAM-3′

Fig. 1 Schematic illustration for the detection of ligand-mediated i-motif folding using gold nanoparticles (GNPs) coated with 5′-thiolated and 3′-FAM labelled C-rich DNA sequences.

School of Chemical Sciences, Indian Association for the Cultivation of Science, Jadavpur, Kolkata-700032, India. E-mail: ocjd@iacs.res.in; Fax: +91-33-2473-2805; Tel: +91-33-2473-4971, ext 1405

†Electronic supplementary information (ESI) available. See DOI: 10.1039/d1ob00248a

Zitierweise: *Angew. Chem. Int. Ed.* **2020**, *59*, 12407–12411
Internationale Ausgabe: doi.org/10.1002/anie.202003461
Deutsche Ausgabe: doi.org/10.1002/ange.202003461

VIP RNA Targeting Very Important Paper

Target-Directed Azide-Alkyne Cycloaddition for Assembling HIV-1 TAR RNA Binding Ligands

*Rakesh Paul, Debasish Dutta, Raj Paul, and Jyotirmayee Dash**

In memory of Professor Rolf Huisgen

Abstract: *The highly conserved HIV-1 transactivation response element (TAR) binds to the trans-activator protein Tat and facilitates viral replication in its latent state. The inhibition of Tat–TAR interactions by selectively targeting TAR RNA has been used as a strategy to develop potent antiviral agents. Therefore, HIV-1 TAR RNA represents a paradigmatic system for therapeutic intervention. Herein, we have employed biotin-tagged TAR RNA to assemble its own ligands from a pool of reactive azide and alkyne building blocks. To identify the binding sites and selectivity of the ligands, the in situ cycloaddition has been further performed using control nucleotide (TAR DNA and TAR RNA without bulge) templates. The hit triazole-linked thiazole peptidomimetic products have been isolated from the biotin-tagged target templates using streptavidin beads. The major triazole lead generated by the TAR RNA presumably binds in the bulge region, shows specificity for TAR RNA over TAR DNA, and inhibits Tat–TAR interactions.*

Human immunodeficiency virus type-1 (HIV-1)[1] contains a cis-acting regulatory element called TAR RNA located upstream of the transcriptional start site (+1 to +59).[2] TAR RNA forms a stable hairpin structure with a hexanucleotide loop and a three base bulge (UCU). A trans-activator protein Tat binds to the bulge region of the TAR RNA and activates HIV-1 replication by stimulating the elongation efficiency of RNA pol II.[3] The interaction between TAR and Tat is essential for viral replication and growth; however, mutated TAR shows a reduced affinity for Tat and is unable to replicate efficiently.[4] Various strategies have been developed to inhibit viral replication, such as targeting the HIV-1 protease and the long terminal repeat (LTR) region. Although numerous classes of small molecules have been reported,[5,6] mutated virus makes them ineffective over time.[7] However, the TAR sequence and its heterogeneity are highly conserved throughout the evolution of the virus (Figure 1a).[8,9] Therefore, the TAR RNA can be targeted for an anti-HIV therapeutic strategy because of its structural integrity and central role in HIV-1 replication.

Herein we demonstrate the rapid discovery of HIV-1 TAR-Tat inhibitors by TAR RNA guided in situ cycloaddition of azide and alkyne fragments. The in situ cycloaddition was also performed with a TAR RNA without the UCU bulge (TAR RNA w/b; w/b = without bulge) and a TAR DNA (Figure 1). The target-guided synthetic (TGS) approach, commonly known as an in situ click reaction, accelerates the discovery of novel pharmaceutical molecules through the involvement of the biological target itself in the selection process.[10] This bio-orthogonal approach has been demonstrated previously using enzymes and a few nucleic acid targets;[11] however, TAR RNA has not been employed as a target to date. The in situ click approach is a unique process which relies on target-guided Huisgen 1,3-dipolar cycloaddition of alkyne and azide residues to produce five-membered nitrogen-containing triazole heterocycles.[12] Triazoles are stable under oxidative or reductive conditions as well as to basic or acidic hydrolysis. Furthermore, they actively participate in hydrogen bonding and π–π stacking interactions with biological targets.[13]

Both alkynes and azides are energetic species and there is a high kinetic barrier for cycloaddition. The kinetic barrier can be overcome by bringing the reactants into proximity with a biological template or with a catalyst.[14] The biological target samples various combinations of the alkynes and azides and synthesizes the best binders with high efficacy. Given the dynamic folding topology of RNA structures, the in situ

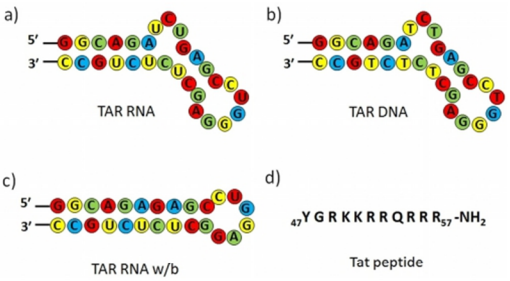

Figure 1. Sequences of a) target TAR RNA, b) TAR DNA, c) TAR RNA w/b, and d) Tat peptide used in the study.

[*] R. Paul, Dr. D. Dutta, R. Paul, Prof. J. Dash
School of Chemical Sciences
Indian Association for the Cultivation of Science
Jadavpur, Kolkata 700 032 (India)
E-mail: ocjd@iacs.res.in
Homepage: http://iacs.res.in/faculty-profile.html?id=98
Supporting information and the ORCID identification number for some of the authors of this article can be found under: https://doi.org/10.1002/anie.202003461.

ACS Biomaterials SCIENCE & ENGINEERING

pubs.acs.org/journal/abseba Article

Carbon Dot Cross-Linked Gelatin Nanocomposite Hydrogel for pH-Sensing and pH-Responsive Drug Delivery

Swarup Krishna Bhattacharyya, Madhab Dule, Raj Paul, Jyotirmayee Dash, Md Anas, Tarun Kumar Mandal, Poushali Das, Narayan Chandra Das,* and Susanta Banerjee*

Cite This: ACS Biomater. Sci. Eng. 2020, 6, 5662−5674 Read Online

ACCESS | Metrics & More | Article Recommendations | Supporting Information

ABSTRACT: Delivery of therapeutics to the intestinal region bypassing the harsh acidic environment of the stomach has long been a research focus. On the other hand, monitoring a system's pH during drug delivery is a crucial diagnosis factor as the activity and release rate of many therapeutics depend on it. This study answered both of these issues by fabricating a novel nanocomposite hydrogel for intestinal drug delivery and near-neutral pH sensing at the same time. Gelatin nanocomposites (GNCs) with varying concentrations of carbon dots (CDs) were fabricated through simple solvent casting methods. Here, CDs served a dual role and simultaneously acted as a cross-linker and chromophore, which reduced the usage of toxic cross-linkers. The proposed GNC hydrogel sample acted as an excellent pH sensor in the near-neutral pH range and could be useful for quantitative pH measurement. A model antibacterial drug (cefadroxil) was used for the *in vitro* drug release study at gastric pH (1.2) and intestinal pH (7.4) conditions. A moderate and sustained drug release profile was noticed at pH 7.4 in comparison to the acidic medium over a 24 h study. The drug release profile revealed that the pH of the release medium and the percentage of CDs cross-linking influenced the drug release rate. Release data were compared with different empirical equations for the evaluation of drug release kinetics and found good agreement with the Higuchi model. The antibacterial activity of cefadroxil was assessed by the broth microdilution method and found to be retained and not hindered by the drug entrapment procedure. The cell viability assay showed that all of the hydrogel samples, including the drug-loaded GNC hydrogel, offered acceptable cytocompatibility and nontoxicity. All of these observations illustrated that GNC hydrogel could act as an ideal pH-monitoring and oral drug delivery system in near-neutral pH at the same time.

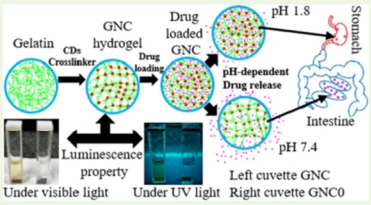

KEYWORDS: *nanocomposite, gelatin hydrogel, drug delivery, pH sensing, cytocompatibility*

1. INTRODUCTION

Approximately 90% of all of the therapeutics are orally administrated as it is less painful, noninvasive, and produces a maximum patient response. However, successful oral deliveries of some therapeutics (protein drugs, insulin, anticancer drugs) for the treatment of local maladies such as ulcerative colitis, inflammation, Crohn's diseases, infections, and colon carcinoma remain a challenge.[1] During passage through the GI (gastrointestinal) tract, drug molecules encounter numerous challenges, like rapid enzymatic degradation, a harsh acidic environment, poor intestinal absorption, and low residence time, which limit the therapeutic efficiency.[2] All of these issues can be addressed by conjugating the therapeutics with some specially designed drug carriers. Together, they can successfully bypass the harsh acidic environment of the stomach and release the drugs in the targeted location. In real practice, some specific types of hydrogel (gelatin, chitosan, pectin, alginate) serve as drug carriers.[2] These hydrogels show a pH-responsive behavior due to the presence of large numbers of carboxylated groups in the main chains. At low pH values, these hydrogels swell less, but at higher pH, they swell more and release the entrapped drug molecules to the target. On the other hand, monitoring a system's pH during drug delivery is also very important. As we know, pH plays a crucial role in many biological and chemical systems. For many pathological and physiological events, precise monitoring of a system's pH is highly recommended. A slight deviation in pH may lead to serious health problems, such as neurological disorder, cardiopulmonary disease, and cancer.[3] To date, different techniques have been reported for pH measurement, including colorimetric, electrochemical, and electromechanical-based methods.[4] However, these techniques are sophisticated, nonuser friendly, and come at a high cost,[4] which reduce their direct application in pH sensing. In this scenario,

Received: July 2, 2020
Accepted: September 17, 2020
Published: September 17, 2020

https://dx.doi.org/10.1021/acsbiomaterials.0c00982
ACS Biomater. Sci. Eng. 2020, 6, 5662−5674

Paul and Majumder, J Comput Sci Syst Biol 2017, 10:4
DOI: 10.4172/jcsb.1000255

Journal of
Computer Science & Systems Biology

Research Article OMICS International

Development of Algorithm for Lorenz Equation using Different Open Source Softwares

Paul R[1,2] and Majumder D[1,2*]

[1]Department of Physiology, West Bengal State University, Berunanpukuria, Malikapur Barasat, Kolkata, West Bengal, India
[2]Society for Systems Biology & Translational Research; 103, Block - C, Bangur Avenue, Kolkata - 700055, West Bengal, India

Abstract

Physiological processes are dynamic in nature and have multi-factorial influences; hence, exhibited as nonlinear and complex. Due to unavailability of data capturing technology in discreet time points, majority of physiological researches are focused on linearity; and hence problems of complexity are addressed empirically. However, in recent time there is an increasing trend to understand the physiological system in a quantitative manner across the globe. Due to unavailability of costly software, it is difficult for students to get an exposure to this global trend. In physical system complexity was first addressed by Edward Lorenz in 1963, which is now known as Lorenz equation. Here we depict the simple computational approach to represent the Lorenz equation using some freely available open source softwares, so that students by themselves can appreciate the importance of the quantitative approach of science and able to represent the complex and nonlinear dynamical behaviour of different physiological systems.

Keywords: Mathematical model; Algorithm; Complexity; Quantitative science

Introduction

Complexity in physical system was first addressed by Edward Lorenz [1] which is now known as Lorenz equations. For this he developed a simplified mathematical model of Ordinary Differential Equation (ODE) of atmospheric convection. These coupled equations have chaotic solutions for certain parameter values and initial conditions. In particular, the Lorenz attractor is a set of chaotic solutions of the Lorenz system which, when plotted, resemble a butterfly or figure eight. Lorenz equations are follows:

$$\frac{dx}{dt} = \sigma(y - x)$$

$$\frac{dx}{dt} = X(\rho - z) - y$$

$$\frac{dz}{dt} = xy - \beta z$$

In the above equations, σ, ρ, β are the system parameters; x, y, z are the system state and t is time.

One can easily assume that σ, ρ and β are positive. Lorenz used the values σ=10, ρ=28, β=8/3. The system exhibits chaotic behaviour for these values [2]. Looking for chaos in cardiac rhythm, brain and population dynamics now has a greater merit in comparison to linear statistical methods. Hence, modeling and data analysis are considered to motivate the investigation in an understanding the behaviour or nature of the biological systems in a dynamical manner, particular their chaotic features, if any. Hence such modeling approach followed by data fitting may be useful in diagnosis and prognosis (predictions about the efficacy of a therapeutic process [3]. From a technical standpoint, the Lorenz system is nonlinear, three-dimensional and deterministic [4].

Development of Algorithm for Solving Differential Equation

If the system of differential equation is a linear there are systemic methods for deriving a solution. Most of the problems biologist encounters are non-linear and for such cases mathematical solutions rarely exist. Hence, computer simulation is often used instead. The general approach to obtaining a solution by computer is as follows:

1. Construct the set of ordinary differential equations, with one differential equation for every molecular species in the model.
2. Assign values to all the various kinetic constants and boundary species.
3. Initialize all floating molecular species to their starting concentrations.
4. Apply an integration algorithm to the set of differential equations.
5. If required, compute the fluxes from the computed species concentrations.
6. Plot the results of the solution.

Step 4 is obviously the key to the procedure and there exist a great variety of integration algorithms. Other than educational purposes, it is rarely a modeller can write their own integration computer code because many libraries and applications exist that incorporate excellent integration methods. An integration algorithm approximates the behaviour of a continuous system on a digital computer. Since digital computers can only operate in discrete time system, the algorithms convert the continuous system into a discrete time system. In practice, a particular step size, h is chosen, and solution points are at the discrete points up to some upper time limit. The approximation generated

*Corresponding author: Majumder D, Department of Physiology, West Bengal State University, Berunanpukuria, Malikapur Barasat, Kolkata, West Bengal, India, Tel: +91-33-25241977; E-mail: durjoy@rocketmail.com

Received September 02, 2017; **Accepted** September 11, 2017; **Published** September 13, 2017

Citation: Paul R, Majumder D (2017) Development of Algorithm for Lorenz Equation using Different Open Source Softwares. J Comput Sci Syst Biol 10: 087-092. doi:10.4172/jcsb.1000255